Progress in Materials Science 132 (2023) 101017

Contents lists available at ScienceDirect

Progress in Materials Science

journal homepage: www.elsevier.com/locate/pmatsci

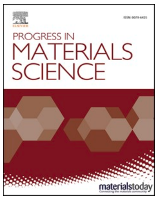

Heusler alloys: Past, properties, new alloys, and prospects

Sheron Tavares [a], Kesong Yang [a,b,c], Marc A. Meyers [a,b,d]

[a] Materials Science and Engineering Program, University of California, San Diego 92093-0418, USA
[b] Department of Nano and Chemical Engineering, University of California, San Diego 92093-0448, USA
[c] Center for Memory and Recording Research, University of California, San Diego 92093-040, USA
[d] Department of Mechanical and Aerospace Engineering, University of California, San Diego 92093-0411, USA

ARTICLE INFO

Keywords:
Heusler alloys
Half metallicity
Mechanical properties
Structure
Spintronics
Giant magnetoresistance effect

ABSTRACT

Heusler alloys, discovered serendipitously at the beginning of the twentieth century, have emerged in the twenty-first century as exciting materials for numerous remarkable functional applications, including spintronics and thermos-electric devices.

The basic structural characteristic is an ordered structure with a face-centered cubic (FCC) superlattice and a body-centered cubic (BCC) unit cell. This structure separates the atoms into distances not encountered in their pure state nor disordered solid solutions and this provides the opportunity for exploring a range of novel material properties. The original alloy, Cu_2MnSn, exhibited ferromagnetism, in spite of the fact that none of the three constituent elements show this behavior in their pure state. Heusler alloys have become a broad class of materials with designations including Full Heusler (with stoichiometry $X_2Y_1Z_1$), Half Heusler (with stoichiometry $X_1Y_1Z_1$), Inverse Heusler (IH), Binary, and Quaternary Heusler (QH). This class of materials is exiting the laboratories, where they were a curiosity and the object of basic investigations, to technological applications. We review here the steps that led to the discovery of these materials, the fundamental principles behind their magnetic and electronic properties, their mechanical properties, and the magnetic shape memory effect that some of them exhibit. The computational design of Heusler alloys is also presented, including the general workflow of the high-throughput computational material design approach, the best-known computational techniques for establishing materials stability, the proper choice of materials descriptors, and the applications of the emerging machine learning approach in the accelerated materials design. We conclude the review article with a discussion of the current challenges and future directions in the field.

1. Introduction and goals

Heusler alloys were discovered at the end of the 19th century but remained for many years a scientific curiosity because of their fascinating ferromagnetism, being composed of non-ferromagnetic elements. There are only four ferromagnetic elements: Fe, Co, Ni, and Gd. The number of papers published on Heusler alloys is over 6,000, but the majority occurred after the significant discovery of their half metallicity (having both metallic and semiconductor character) in 1983 by de Groot [1]. This property makes them excellent candidates for spintronic devices, which were made possible by the discovery of the Giant Magnetoresistance (GMR) effect in 1988. The evolution of publications is shown in Fig. 1 [2]. The rapid rise in numbers since the 1980 s is astounding. The most important breakthroughs since the 1883 discovery of these alloys [3,4] are presented in Fig. 2. In addition to the GMR effect, some alloys were found to exhibit reversible martensitic transformations generating both the shape memory and superelastic effects. Interestingly, the martensitic transformation is affected by an externally applied magnetic field, leading to significant strains. This effect opens the door for a number of applications in sensors and even magnetic refrigeration. This will be presented in Section 9. Some alloys also exhibit

https://doi.org/10.1016/j.pmatsci.2022.101017
Received 14 February 2021; Received in revised form 19 August 2022; Accepted 27 August 2022

antiferromagnetism, a property that has potential use in spintronics.

There have been several reviews on Heusler alloys [5–8], the most notable being the excellent collection of articles edited as a book by Felser and Hirohata [9]. It contains twenty chapters addressing many important aspects, ranging from theory [10,11], functional properties [12–14], nanoparticles, martensitic transformations [15] and applications such as spintronic (giant magnetoresistance) devices [16,17], thermoelectric and other energy conversion devices [18,19], thin-film growth [20], and new properties [21].

This review, intended for the non-specialist, provides an introduction to these complex materials. This is a rapidly evolving field with research at the global level introducing new ideas and applications at a high rate. Section 2 covers the history of the development of these alloys, which started with the discovery of ferromagnetism in ternary (Cu_2MnSn and Cu_2MnAl) systems wherein the three elements were not ferromagnetic. This research led to a broad class of materials exhibiting outstanding functional properties. Thus, the contemporary classification of Heusler alloys encompasses three types (binary, ternary, and quaternary) presented in Section 3. The electronic and magnetic properties of Heusler alloys are presented in Section 4. In this context, Section 5 describes the most important property of half-metallicity, which enabled spintronics (Section 6). New Heusler alloys based on transition metals, called all-*d*-metal Heusler alloys, which have great potential for applications in solid-state refrigeration, are presented in Section 7. Some of these alloys also display the shape-memory effect (Section 8), albeit magnetic and not mechanical, like the common Ni-Ti alloys, well known to materials scientists.

Magnetocaloric and inverse magnetocaloric effects open the door to solid-state refrigeration applications. An important discovery was the multicaloric effect, whereby mechanical and electric fields can generate the martensitic phase and enhance the magneto caloric effect; these caloric effects are explained in Section 9. Topological insulators, a new state of quantum matter, which are being considered for application in spintronic and quantum computing are covered in Section 10. The mechanical properties of Heusler alloys have received relatively less attention but are nevertheless summarized in Section 11. This is an area where we recommend additional research efforts, especially in thin films.

These fundamental properties are being exploited in the development of novel applications, some of which are presented in Sections 12 and 13. The computer design of alloys is being vigorously applied to Heusler alloys and is enabling the discovery of new systems with enhanced functionalities (Section 13). It is hoped that the overview presented herein will introduce the non-specialist materials scientist to this rapidly expanding field of research.

2. Historical Aspects: Facts leading to the discovery of the Heusler alloys

The history of Heusler alloys is a fascinating one, and some of the complexity it carries is since there were three, and not one Heusler: Conrad, Friedrich (or Fritz), and Otto Heusler. They each contributed to what resulted in a class of ferromagnetic alloys comprised of non-magnetic components which have outstanding functional applications. The work started in the search for a new bronze.

In 1876 the “Isabelle” Plant, located in Dillenburg (Germany) began to produce technically iron-free manganese. This company specialized in the manufacture of bronze (a CuSn alloy). Problems invariably arose in melting the bronzes, e.g., oxygen absorption and consequent copper oxide formation causing loss of vital properties. These undesired effects were partially eliminated by the addition of phosphor to the bronze. The phosphor removed the copper oxide from the material, but side effects were clearly noticeable by an increased brittleness. In order to avoid this inconvenient property, Conrad Heusler [22] brought forth in 1881 the idea of adding

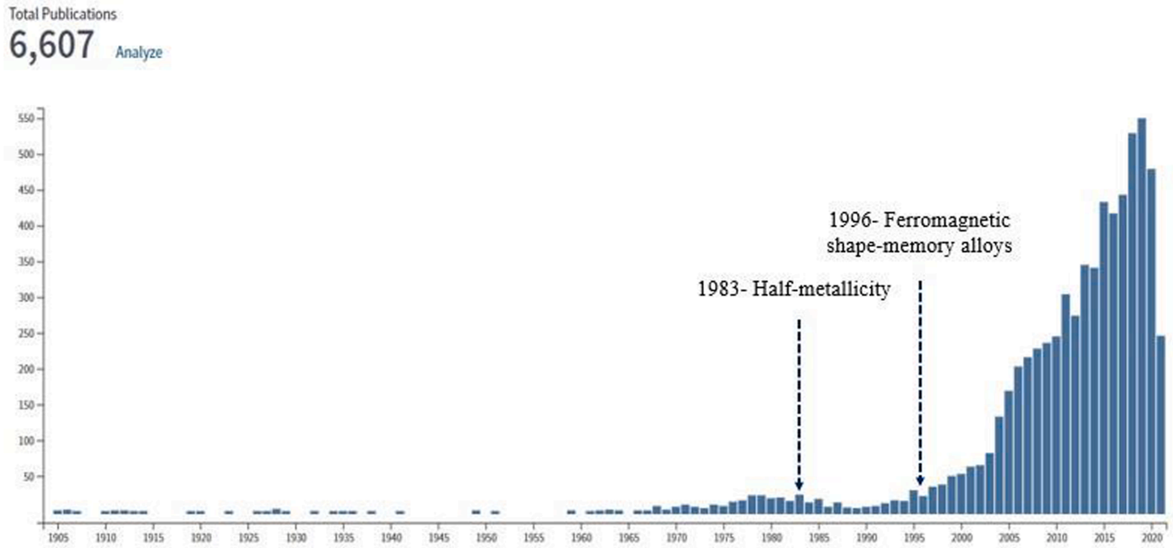

Fig. 1. Total publications with the name “Heusler Alloys”; notice a rapid increase after de Groot et al. [1] discovers half metallicity. (From Web of Science [2]).

manganese to the bronzes. The substitution of phosphor by manganese as a reducing agent was successful, and the Cu-Mn-Sn alloys had properties that made them common-use materials at the end of the last century.

They could be rolled and forged. They retained their properties at high temperatures, being therefore extremely useful as tightening bolts inside steam engines of locomotives. Furthermore, they had a wide range of applications in electrical measuring instruments, under the commercial name of "Manganin." Their dimensional constancy was particularly important for use in spools, around which copper conduction leads were wound. The precision obtained in electrical measuring instruments at that time was to a great extent due to the size invariability of the "Manganin" alloys. Seventeen years later, in 1898, a second Heusler, Friedrich [23], discovered by chance the ferromagnetic properties of this alloy. He had prepared a spool by quickly cooling and aging it. He was mounting it in an electrical instrument when he noticed that it was strongly attracted by one of its magnets. By repeating the experiments with other alloys, he observed still stronger attraction with Cu-Mn-Al.

The importance of manganin, and other alloys which have a negligible coefficient of thermal expansion, was recognized by the precision instrument industry, especially in Switzerland. The Swiss Physicist Charles Edouard Guillaume was awarded the 1922 Nobel prize for the study of these alloys. Contemporary versions of Manganin, with a composition of 86 %Cu-12 %Mn-2 %Ni, are used in gages for the determination of the pressure in shock compression experiments because of the high sensitivity of their resistance to hydrostatic pressure. For example, Manganin gages were used by Hsu et al. [24] in shock compression experiments on nickel. They are also used in shunts and in manganin-constantan thermocouples which use the thermoelectric effect.

2.1. Early work on structure determination

In his subsequent investigations, Friedrich Heusler found the following alloys to be ferromagnetic: Cu-Mn- (Sn, Al, As, W, Sb, B). The communication, as well as quantitative measurements of intensities of saturation magnetization by magnetometric techniques, was made in 1903 [25,26]. The highest magnetization was found at the compositions Cu_2MnAl and Cu_6Mn_3Sn. The enormous interest which arose from these discoveries was to great extent due to the fact that while the alloys were ferromagnetic, its constituent elements were diamagnetic or paramagnetic. Table 1 [27] shows the mass susceptibilities of various elements participating in Heusler Alloys.

The Heusler alloys have mass susceptibilities higher than 1 and are ferromagnetic. Some workers initially suspected that the ferromagnetism in the Heusler alloys was associated with the presence of iron traces. In Heusler's [25,26] original work, the iron content was approximately 0.4 %. In order to investigate the influence of iron, Haupt [28] prepared identical alloys having 0.4 and 1.2 % iron. They were indistinguishable in the magnetometer. Furthermore, Honda [29] observed that iron, in percentages smaller than 2 %, never had any noticeable magnetic effect on alloys. The suspicion on the influence of iron was therefore definitely discarded.

The Cu-Mn-Sn system was explored by Take and Semm [30] in 1914 and the presence of two magnetization maxima was confirmed, at the compositions Cu_2MnSn and Cu_6Mn_3Sn. Ross and Gray [31] studied in 1910 a series of Cu-Mn-Sn and Cu-Mn-Al alloys. Their results did not allow a final conclusion and the maximum magnetizations with the tin alloys were much lower than with aluminum alloys. Later studies show that this is absolutely not true [32]. Ross and Gray [9] thought that the intermetallic compounds Cu_3Al and Cu_3Sn played an important role in determining the magnetic behavior. They concluded by saying that these compounds had similar behavior to Heusler alloys after undergoing similar heat treatment. It seemed therefore likely that magnetism in Heusler alloys of aluminum or tin was due to the entrance of the intermetallic compounds into solid solutions.

2.2. Congress on magnetism

In 1912 the Faraday Society sponsored a congress on magnetism. A series of papers on Heusler alloys were presented. The

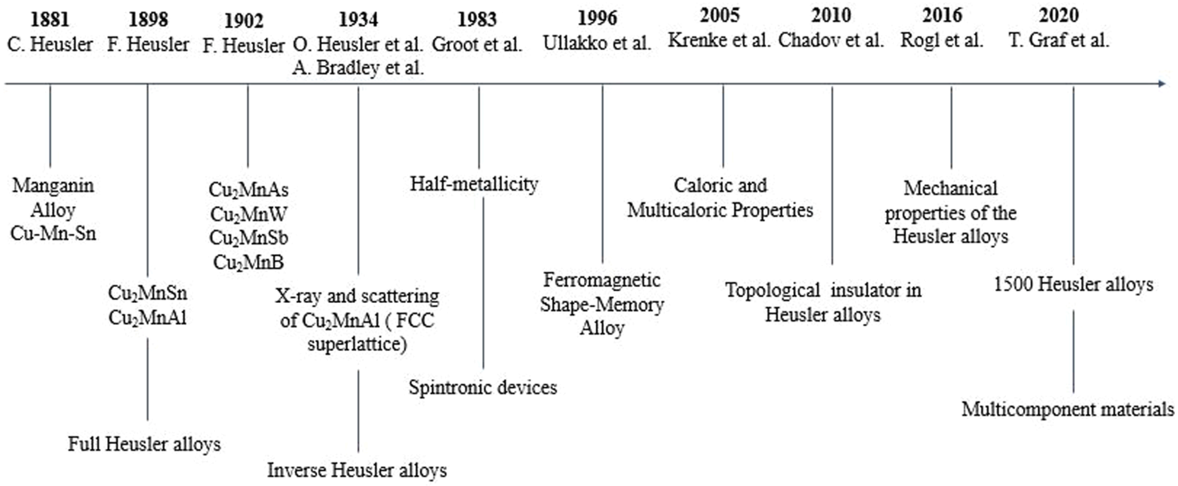

Fig. 2. Historical development of the Heusler alloy field. (From Meyers [3], Wollmann et al. [4]).

Table 1
Mass susceptibilities of elements [27].

Element	X x10^6 (in cm^3/g)	Classification
Cu	−0.086	Diamagnetic
Mn	9.7	Paramagnetic
Al	0.65	Diamagnetic
Sn	−0.25	Diamagnetic
Gd	−0.24	Ferromagnetic
In	−0.11	Diamagnetic
Ag	−0.2	Diamagnetic
Bi	−1.34	Diamagnetic
B	−0.69	Diamagnetic
As	−0.31	Diamagnetic
Co	$> 10^6$	Ferromagnetic
Ni	$> 10^6$	Ferromagnetic
Sb	−0.87	Diamagnetic
Au	−0.15	Diamagnetic

impressive number of references cited in their bibliography indicates that these alloys had been extensively studied, since their discovery in 1898. Some polemics took place, and they are worth describing.

Heusler [33] attacked Wedekind for claiming for himself the association of the ferromagnetic properties of Cu-Mn-(As, Sb, Bi, B, Al, Sn) with the molecular structure. It seems that Wedekind had not cited Heusler as the original discoverer, a common occurrence even in our days. In the same communication [11], Take criticized Ross and Gray [9] for claiming the priority in the explanatory theory involving solid solutions of Cu_3Sn and Cu_3Al. Heusler had for the first time indicated [34] the solid solution $(Cu, Mn)_3Al$ as responsible for ferromagnetism. This communication preceded Ross' and Gray's [31] by one year.

Heusler and Take refuted a theory explaining ferromagnetism forwarded by Guillaume. Guillaume assumed that pure manganese existed in a strongly magnetic allotropic form. This structure was stable only at very low temperatures. The addition of aluminum or tin had the effect of raising the transformation temperature so that ferromagnetism of Heusler alloys became possible at room temperature. However, this theory did not explain strong ferromagnetism in Cu-Mn- (As, Sb, Bi, B). Furthermore, no experimental evidence existed of the low-temperature ferromagnetic form of manganese.

Ross [35] presented a summary of all his previous work, which included magnetometric and metallographic analysis. He maintained his position as the first investigator to associate ferromagnetism with a solid solution of the type $(Cu, Mn)_3Al$. This can be seen from his statement: "Moreover, the metallographic examination of the structure of some of these alloys, which has been recently taken in hand, has already afforded valuable evidence in support of certain hypothesis first advanced by the author 3 years ago, and it had done much to explain the behavior of the alloys under varying heat treatment." However, there is no solid evidence in his support and the facts indicate that Heusler was the original introducer of the idea. Furthermore, Ross concluded, by deviating from his first proposition [31], stating that the solid solutions were probably composed of two intermetallic compounds, Cu_3Al and Mn_3Al. This conclusion was wrong. Another paper presented at this meeting analyzed the magnetic changes taking place with heat treatment, without coming to any positive conclusions. In general conclusion, the knowledge in 1912 on Heusler alloys was:

a) Ferromagnetism is caused by the presence of manganese atoms.
b) Ferromagnetism is associated with a solid solution of the type $(Cu, Mn)_3Al$.
c) Aging has confusing effects on ferromagnetism.
d) The highest saturation magnetizations appear at the composition Cu_2MnAl and Cu_2MnSn.

2.3. Ordering studies

In 1927 Harang [36] studied a series of Cu-Mn-Al alloys by X-ray diffraction, each containing 12 % aluminum. He detected the presence of three phases in the magnetic alloy. These three phases were probably present because of the sluggishness of his quenching procedure. These phases remained basically identical for different manganese compositions. They were:

a) FCC structure of copper (α); a = 0.37 nm
b) BCC structure (β); a = 0.3 nm
c) A phase having an intricate cubic lattice, with 52 atoms per unit cell (ϒ); a = 0.870 nm.

The beta phase was identical to the previously described $(Cu, Mn)_3Al$ solid solution. Harang [36], therefore, contradicted Heusler [11], concluding that ferromagnetism could not be exclusively associated with the beta phase. It resulted, according to him, from the interaction of the three phases α, β, and ϒ.

Persson [37] made a substantial contribution to the knowledge of Heusler alloys in 1928. He subjected Harang's [14] β phase to a careful crystallographic examination. His alloys had undergone a fast quench, inhibiting, for the most part, the precipitation of the low-temperature phases alfa and gamma. He confirmed the BCC nature of the structure but noticed ordering among aluminum atoms. They occupied sites of an FCC lattice with twice the lattice parameter (a = 0.605 nm) of the BCC. Thus, the basic pattern of a BCC structure with an FCC superlattice was identified. In ideal conditions, the unit cell contained four aluminum and twelve copper and manganese atoms. Their positions referred to as letters in Fig. 3, are: B is aluminum; A, C, and D are copper and manganese.

X-ray techniques did not, at that time, allow distinction between copper and manganese atoms, because of their nearly identical scattering powers. Wrong conclusions were, however, drawn by Persson on the change of magnetization with heat treatment. He observed that alloys with low manganese amounts exhibited an increase in magnetization with aging. Persson's explanation was that the α and β phase appearing during aging allowed the beta phase to be enriched by manganese. It is nowadays a well-known fact that saturation magnetization increases due to a more perfect ordering attained by the atoms.

Most of the investigations conducted up to 1928 included considerations on aging and its effects on magnetizability. The aging studies always gave confusing information. For this reason, Otto Heusler [38] decided, in 1928, to systematically analyze the copper-rich portion of the Cu-Mn-Al system. The techniques used in his work were differential thermal analysis and microscopic examination. He observed that the beta phase, existing over a considerable range of the ternary system, had its origin in the Cu-Al system. It advanced into the ternary, surrounded by the two adjoining regions (α + β) and (β + ϒ). This configuration was stable at higher temperatures ($T > 600$ °C). Fig. 4 shows an isothermal equilibrium section at a high temperature.

As the temperature dropped the beta phase range shrank. At low enough temperatures ($T < 600$ °C) it underwent a eutectoid decomposition into (α + β). Some of the previously contradictory results obtained by aging were thus explained by the fact that this eutectoid decomposition was very sluggish. From the three structures observed by Harang [14] and Persson [15], only the α and β were at equilibrium at low temperatures. This tentative phase diagram was later found to be partially incorrect at low temperatures [39]; many other phases appear and complicate the picture. However, it was of great help in interpreting heat-treatment results.

Potter [40] in 1928 made an investigation with single crystals of Cu_2MnAl. The elegance of his work justifies a detailed description. He initially tried to grow Cu_2MnSn single crystals. This was, however, impossible due to the low melting point of the alloy at the highest saturation magnetization composition. He analyzed the quenched specimens by X-rays, confirming the already identified beta structure [15], by taking advantage of the fact that single crystals show different magnetizations along different crystallographic directions.

The directional magnetic properties of the Heusler alloys were almost identical to those of nickel (FCC) and had no resemblance to the directional properties of iron (BCC). This would be understandable if the magnetization were mainly produced by the distribution of the aluminum atoms. It appeared more probable, however, that the important factor was the presence of manganese. It was known to form various ferromagnetic compounds and alloys; thus, ferromagnetism was usually attributed to its presence. On this assumption, the directional properties would probably depend on the spatial distribution of the manganese atoms. In a conclusion, Potter stated that manganese, like aluminum, was arranged in an FCC structure.

There are, however, two possible ordering models. Potter [21] concluded by considering two alternate models but could not decide between either of them because of inadequate X-rays techniques at the time. These models can be described, according to Fig. 3, by the following distribution:

- Model 1: A – Cu; B- Al; C – Cu; D – Mn
- Model 2: A – Mn; B – Al; C – Cu; D – Cu

In 1929, Persson [41] presented a complete report on his previously described conclusions [17]. He carefully investigated the Cu-

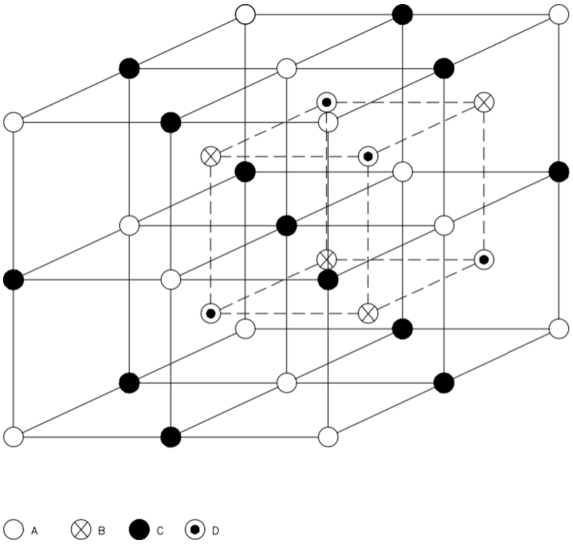

Fig. 3. In the beta-phase structure in Heusler Alloys; four atomic positions are shown which can be established through X-ray diffraction using structure factor analysis (Adapted from Meyers et al. [60]).

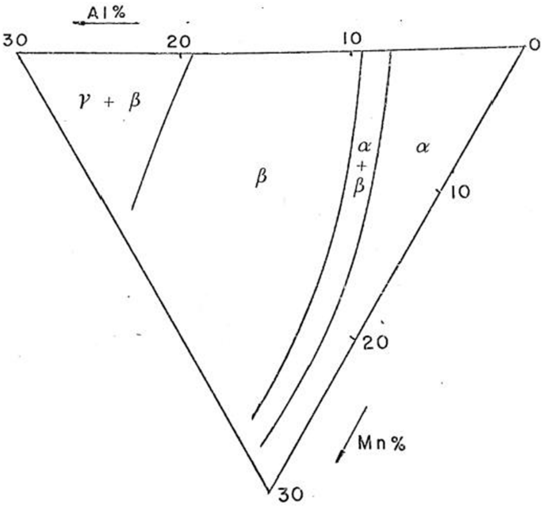

Fig. 4. Tentative phase diagram for Cu-Mn-Al. (Isothermal section for T > 600 °C). (From Meyers [3]).

Mn-Al system, having already the knowledge of the metastability of the beta phase at room temperature [38]. By analogy, he extended his conclusions to the Cu-Mn-Sn system. He prepared sets of quenched and slowly cooled alloys. The quenched alloys were analyzed, showing the presence of the β phase only. By comparing the saturation magnetizations with X-ray determinations (taking relative intensities of the lines into consideration) he came to the final conclusion that the β phase alone was responsible for ferromagnetism. In the quenched alloys the maximum magnetizations occurred at the composition Cu_2MnSn and Cu_2MnAl.

This was already a well-known fact, but Persson reasoned that it was so because this composition allowed ideal conditions for ordering among Mn atoms. He, therefore, suggested two alternate ordering models, identical to those of Potter [40]. The aging experiments showed that the β phase decomposed into two or more phases. If the manganese content was less than the required for the formation of the Cu_2MnAl, the phases were Cu_3Al (a = 0.583 nm) and Cu_2MnAl (a = 0.595 nm). If the manganese content was larger, a structure of the β Mn type (a = 0.6370 nm) was formed, besides the Cu_2MnAl. Less emphasis was given to the Cu-Mn-Sn system. Persson [19] said that its β phase had probably the same type of ordering. The β phase decomposed, by aging, into an FCC structure (a = 0.616 nm) and a phase very similar to hexagonal Cu_3Sn (a_1 = 0.2.824 nm), (a_3 = 0.4502 nm), (a_3/a_1 = 0.1594 nm).

Valentiner and Becker [42] presented in 1933 a comprehensive review on aging studies done on Cu-Mn-Al. They added to this their personal experiments; the purpose of the work was to obtain consistent knowledge on aging. They completely ignored the phase diagram constructed by Heusler [38] and therefore tried to relate saturation magnetizations and compositions with Curie temperatures. Their conclusions are, as stated in their communication: “The aging temperatures influence the change in magnetic properties, as well as the formation of the ordered Cu_2MnAl crystal in different ways at different temperatures”. “The most appropriate aging temperature varies with the composition of the alloy.”.

In 1934 the ordering among manganese atoms was experimentally proved. It is interesting to observe that two workers came independently to these conclusions, but the communications were made on the same date, in different journals: October 4, 1933. The coincidence is rather strange, since the techniques they used were nearly identical. A fact that enhances the suspicion that some information transfer might have taken place is that there is no common elucidative reference from which the authors could have gotten their conclusions. They will be described below.

Otto Heusler [43], by using X-ray techniques and electrical measurements, studied quenched Cu-Mn-Al alloys in the beta range. He comparatively analyzed two possible ordering models previously suggested by Potter [40] and Persson [41], by designating them by their space groups: Oh^5 and Td^2. He calculated the structure factors of the diffraction patterns for the two groups in an extremely rough manner. Intensities were taken, as a first approximation, as proportional to the squares of the structure factors. The ratios found between the intensities of the three types of lines (designated X, Y, and Z) were:

- Oh_5 I_x: I_y: I_z = 100:4.34:1.56
- Td_2 I_x: I_y: I_z = 100:1.56:2.95

The structure factors were calculated by taking advantage of the phenomenon of anomalous dispersion. Fe Kα radiation increased the intensity differences between the Y and Z lines for the two models. The X-ray experiments showed that the Y lines were much stronger than the Z lines. This served as a confirmation of the Oh_5 structure, corresponding, in Fig. 3, to the following atomic positions:

- A - Cu
- B - Mn
- C - Cu

- D – Al

Ordered alloys are known to have a decreased resistivity and an increased dependence of conductivity on temperature. Electrical measurements conducted by Heusler [21] confirmed that maximum ordering existed at the composition Cu_2MnAl. Bradley and Rogers [44] prepared an alloy close to the stoichiometric composition Cu_2MnAl. They subjected it to a fast quench in order to fully retain the beta phase. They considered three alternate ordering models: the ones suggested by Potter [40] and Persson [41] and the third one with randomization between copper and manganese atoms. The structure factors were calculated with great precision, by taking into account the effect of the incident angle, the wavelength of the incident radiation, and anomalous dispersion near the K absorption edge of the elements. The intensities of the lines were calculated by means of the expression:

$$I = \frac{1 + cos^2 2\theta}{sin^2\theta\cos\theta} p|F|^2 \tag{1}$$

where I is the intensity, p is the multiplicity factor, and F is the structure factor. Calculations were made for Fe Kα, Cu Kα, and Ni Kα incident radiations. A comparison of calculated and actual data led the authors to conclude that ordering existed among manganese atoms and that it corresponded, according to Fig. 3, to the following pattern:

- A-Cu
- B-Mn
- C-Cu
- D-Al

Bradley and Rodgers [44] conducted their work with more precision than Heusler [43]. They based their structure factor calculations on strong theoretical evidence. Their investigation was more rigorous than Heusler's, but it is interesting that both arrived at the same structure.

2.4. Investigations on Heusler alloys from the 40 s to the 70 s

In the years following the discovery of the Heusler alloys, the attention of investigators was concentrated for the most part on the Cu-Mn-Al system. This interest was justified by the fact that this system exhibited the highest saturation magnetization. However, after the structure responsible for the magnetization had been identified and fully investigated, the interest in other Heusler alloys grew. In 1942 Carapella and Hultgren [32] published the results of a systematic investigation of the beta phase range in the Cu-Mn-Sn system. They used X-ray, microscopic, and magnetometric techniques. They designed quenching equipment that allowed an almost instantaneous quench. Earlier saturation magnetizations obtained on the Cu-Mn-Sn systems were usually very low because sluggish quenching media were used. The decomposition of the beta phase in the Cu-Mn-Sn is extremely fast and had never been completely inhibited in the early investigations. Carapella and Hultgren [32] obtained saturation magnetizations exceeding the highest values reported for the Cu-Mn-Al system. They outlined the phase range for temperatures above 620 °C, and it is shown by the full line in Fig. 5.

No evidence of a Curie point, corresponding to the order–disorder transformation temperature, was found. X-ray photographs taken at 630 °C showed the presence of superlattice lines. Quantitative magnetometric measurements showed that high saturation

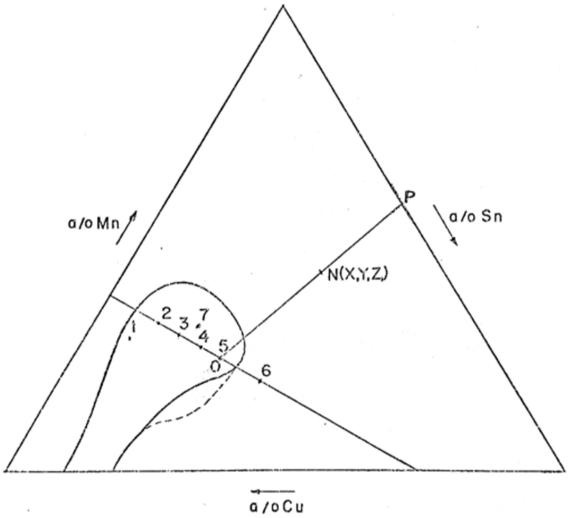

Fig. 5. The beta phase range for Cu-Mn-Sn (for T > 600 °C) and alloys was studied by Meyers et al. [60]. (From Meyers [3]).

magnetizations were confined to alloys having long-range ordering. The highest value for the intensity of saturation magnetization was equal to Ms = 660 emu. cm^{-3} (~0.830 Wb/m^2); it was found at the composition Cu_2MnSn. The investigators did not, however, make a careful ordering study by X-rays.

In 1947 Valentiner [45] discovered ferromagnetism in the system Cu-Mn-In. Sometime later, the maximum was detected at the composition Cu_2MnIn [46,47]. In 1948 Hames [48] reported ferromagnetism in the system Cu-Mn-Ga. In the following years, many other ternary systems of manganese were found to exhibit ferromagnetism. A complete investigation on a series of alloys inside and outside the Cu-Mn-Sn range was performed in 1953 by Valentiner [49]. He corrected the beta limits previously traced by Carapella and Hultgren [10].

This is indicated in Fig. 5 by a dotted line. The quenched and slowly cooled alloys were analyzed by X-rays. The slowly cooled alloys having a composition close to Cu_2MnSn showed an FCC structure of the C_{15} type. The lattice parameter was 0.69658 nm. Valentiner [23] attributed the composition Cu_8Mn_4Sn to it. He considered it to correspond to the Cu_6Mn_3Sn magnetization maximum found by Take and Semm [30]. He interpreted some of Carapella’s aging results, in terms of the Cu_8Mn_4Sn C_{15} phase. The C_{15} phase was, according to him, ferromagnetic, and the increase of ferromagnetism due to its appearance more than compensated for the decrease due to the precipitation of the ordered β phase. So, he returned to the old-fashioned idea [36] that more than one phase was responsible for ferromagnetism.

Taglang and Ash [50] studied in 1954 the transformation occurring in Cu_2MnSn. They observed that the decomposition of beta Cu_2MnSn into an FCC structure with a lattice parameter of approximately 0.7 nm and the Cu_3Sn phase coincided with the decrease in ferromagnetism. This contradicted Valentiner’s [49] conclusions. They observed that the beta phase was stable above 500 °C but only had a considerable range of existence at 620 °C. Based on their magnetometric measurements, they suggested that it remained ordered up to melting temperature. Thermal differential analysis measurements were made, indicating the presence of an intermediate state between 400° and 440 °C.

The copper-rich portion of the Cu-Mn-Al system underwent a systematic survey in 1956 [39]. The isothermal sections above 600 °C confirmed the phase diagram constructed by Heusler [38]. However, at low temperatures, an intricate array of phases appeared. One fact that should be noticed is the discovery of the intermetallic compound Cu_3Mn_2Sn, having a C_{15}-type structure. It was formed by the peritectoid reaction $\beta + \beta$ Mn = Cu_3MnAl at temperatures below 550 °C.

In 1961 Gladyshevskii et al. [51] confirmed the existence of the Cu_4MnSn compound in the Cu-Mn-Sn system. Taglang [52] repeated his original experiments in 1961 by using dilatometric, electrical resistance, and X-ray measurements. He confirmed the existence of an intermediate state limited by two transformations:

a) A first-order transformation at 432 °C
b) A second-order transformation at 477 °C

From this fact, he concluded that all alloys quenched from above 477 °C showed at room temperature the phase which was stable between 432 °C and 477 °C. According to him, the high-temperature phase, existing between 477 °C and 650 °C was never retained. He concluded that the intermediate state corresponded to the ordered beta phase. The order–disorder transformation occurred at 477 °C. He did not verify his conclusions by high-temperature X-ray photographs. Those had been previously done by Carapella and Hultgren [32] showing ordering up to melting temperature. Therefore, Taglang’s conclusions [50] are probably wrong.

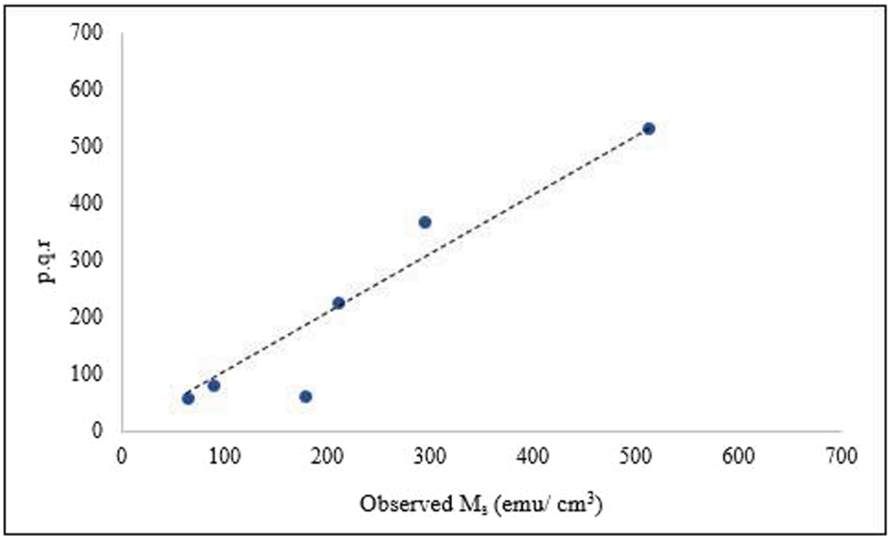

Fig. 6. Correlation between experimental parameter p.q.r from X-ray diffraction with saturation magnetization for six Cu-Mn-Sn alloys within the β range (shown in Fig. 5). (Adapted from Meyers et al. [60]).

In 1963 Oxley, Tebble, and Williams [53] analyzed a series of Heusler alloys. They could not detect ferromagnetism in the Cu-Mn-Sb system, although it had been previously reported. Cu_2MnGe was found to be ferromagnetic. However, this behavior could not be associated with a BCC-ordered structure; X-ray measurements showed a tetragonal structure. Cu_2MnBi and Cu_2MnGa were polyphase, and the ferromagnetism was interpreted as being due to the precipitation of two binary phases.

Johnson et al. [54–56] reported in 1968 several discoveries on Heusler alloys. In their first communication [54] they studied partial disordering in quenched Cu-Mn-Al alloys by X-ray and neutron diffraction. They analyzed the reordering taking place by aging and producing the maximum magnetizability. The second communication presented a discussion on the nature of the intermetallic compound Cu_3Mn_2Al. It was found to be a Laves phase and antiferromagnetic. Their last investigation was on the Cu-Mn-Sb system, where Oxley [53] and Heusler [23] had obtained conflicting results. In 1971, Webster [57] investigated the structural and magnetic characteristics of some ternary systems of cobalt and manganese. In 1972, this same author carried out a series of studies on the magnetic and chemical order containing cobalt and titanium-containing alloys [58].

In the early seventies, Meyers and Hepworth [59] determined the enthalpies of formation of several Cu-Mn-Sn alloys within the beta phase range; they were trying to obtain the enthalpy of ordering but the sensitivity of the apparatus (tin calorimeter) was not sufficient. Later, Meyers et al. [60] confirmed the ordered structure for this alloy using X-diffraction and structure factor calculations. Thus, Cu_2MnSn and Cu_2MnAl have the same structure. They also measured the saturation magnetization and correlated it with a function of the long-range ordering parameter. A parameter p.q.r composed of three factors was defined; p corresponds to a number varying linearly from the composition Cu_2MnSn ($p = 1$) to the boundary of the β region ($p = 0$) in Fig. 6; q is the fraction of β phase retained upon quenching as deduced from the height of the peaks in the X-ray diffractometer; and r is the highest value of the saturation magnetization reported for Cu_2MnSn, namely 660 $emu.cm^{-3}$ ($\sim$0.830 Wb/m^2). The straight line represents a perfect correlation. It can be seen that the parameter p.q.r represents the saturation magnetization of the different alloys fairly well and that the maximum saturation magnetization corresponds to the composition Cu_2MnSn. Some deviations are observed which are due to experimental errors.

In the middle of the seventies, the magnetic properties of Heusler alloys continued to be explored. Ziebeck and Webster [61] investigated the neutron-diffraction and magnetization of Heusler alloys with the composition Co_2YZ (Y belongs to the family IVA or VA, while Z represents the group IIIB or IVB of the periodic table). It was demonstrated that for the same family, the magnetic moment and Curie temperature of alloys are similar, but their lattice parameters vary if Z belongs to the IIIB or IVB group. This behavior suggests that for these Heusler alloys, the change in electron concentration has a larger effect on the magnetic properties than the change in the lattice parameter.

Noda and Ishikawa [62] studied the spin waves of two Heusler alloys, Pd_2MnSn and Ni_2MnSn, to understand their magnetic interactions. Neutron scattering was used to determine the magnetic interactions because this technique has considerable precision. The results indicated that the magnetic interaction for the alloys studied is long-range, reaching more than eight neighbors. In addition, only Mn atoms have a magnetic moment. For both alloys, it was observed that the first two nearest-neighbor interactions are ferromagnetic, and that the Curie temperature is defined by the interactions.

2.5. Research activity from the 80 s to present

Whereas the activity in Heusler alloys continued at a moderate pace in the seventies, an acceleration of research occurred from the

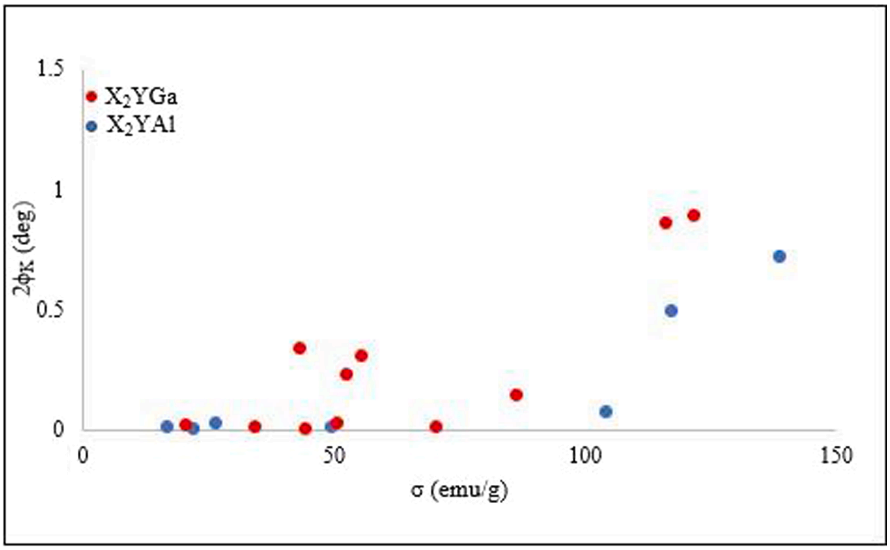

Fig. 7. Kerr rotation at room temperature versus the corresponding at an ambient temperature saturation magnetization. (Adapted From Buschow and Engen [63]).

80 s, as evident from the number of publications in Fig. 1. The triggering event was the discovery by de Groot et al. [1]. This work is introduced and briefly described here. An in-depth and detailed presentation of the development is presented in Sections 6 to 13.

In the eighties, Buschow and Engen [63] studied a series of compounds with the general formula X_2YZ, to investigate their magnetic and magneto-optical properties. In this study, X is a 3d transition metal or Cu, Y characterizes a second 3d transition metal, and Z represents Al or Ga atoms. The results showed that a limited combination of these elements promotes the formation of the cubic $L2_1$ phase. Regarding the magnetic properties, they found that, for the X_2MnZ Heusler alloys, the magnetic moment of the Mn does not depend on the X and Y elements. This same effect was demonstrated by Noda and Ishikawa [62]. It is known that ferromagnetic compounds with high Kerr rotation are used in magneto-optical recording devices. As the Heusler alloys are formed by different components and their magnetization can be altered extensively, Kerr's effect was analyzed for these materials. The Kerr effect of a material is defined as the change in its refractive index as a function of an applied electric field. A plot of the Kerr rotation as a function of the saturation magnetization at ambient temperature is shown in Fig. 7. The materials with the highest values of Kerr rotation also have the maximum saturation magnetization values. However, according to Buschow and Engen [63], the correlation between these two variables cannot be assumed. The highest Kerr rotation values are found for the systems Co_2FeAl and Co_2FeGa. In contrast, the lowest Kerr rotation values are observed in the alloys containing Mn. According to Buschow and Engen [63], Mn atoms, when combined with other magnetic 3d metals, cause a deleterious effect on the Kerr rotation. Table 2 presents the Kerr effect for the Heusler alloys studied.

In 1983, de Groot et al. [1] discovered a most important phenomenon regarding this class of materials, the half-metallicity. They studied the electronic properties of four Half-Heusler alloys: NiMnSb, PtMnSb, PdMnSb, and PtMnSn, and observed a particular behavior for the NiMnSb alloy. Its majority-spin band has a metallic character; the minority-spin band is a semiconducting behavior. The conduction electrons are 100 % polarized at the Fermi level. This unusual feature is known as half-metallicity. Materials that exhibit this behavior are strong candidates for spintronic applications. After de Groot's discovery, many investigations have been conducted to search for half-metallicity in other families of Heusler alloys. In this context, two important research groups, led by Galanakis [64–72] and Felser [73–82] have been studying theoretical and experimental aspects of the half-metallicity in Heusler alloys. This will be further discussed in Section 5.

A discovery related to the Heusler alloys was made by Webster and collaborators [83]. They found a peculiar behavior for Ni_2MnGa alloys. During quenching heat treatment, these alloys undergo a martensitic phase transformation. The transformation occurred at a temperature below 202 K. Fig. 8(a), (b), and (c) present the microstructure evolution at different temperatures: above 202 K, at approximately at 202 K, and below 202 K, respectively. For temperatures above 202 K, there is no martensite formation. At a temperature of nearly 202 K, the phase transformation is initiated. Finally, at a temperature below 202 K, martensitic platelets are observed over the entire surface. This pioneering work by Webster et al. [83] opened a new study field for the Heusler compounds because certain alloys that undergo structural transformation display superelasticity of a few percent as well as thermal recovery strains. Compounds that exhibit these features are known as magnetic shape-memory materials due to their capability to exhibit a large magnetically-induced strain due to the formation of the martensitic phase. As consequence, this class of materials is classified as 'new actuators.'.

In the nineties, it was reported that higher performance of new actuators is achieved by magnetic field control of the shape memory effect. As a result, many research groups studied ferromagnetic alloys with the martensitic transformation, allowing control of the

Table 2

Kerr effect. The lattice constant (a), Curie temperature (T_c), saturation moment at 4.2 K (μ_s), saturation magnetization at 300 K (σ_{300}), and Kerr rotation ($2_{\phi k}$) [63]. The T_c of Co_2MnAl was exported from Webster's investigation [58] while Co_2V and Co_2HfAl were exported from Ziebeck and Webster [61].

Compounds	Heat treatment	a (Å)	T_c (K)	μ_s (μB/FU)	σ_{300} (emu/g)	$2_{\phi k}$ degrees	
						633 nm	830 nm
Mn_2VAl	30d 800	5.932	–	1.82	50	0.02	0.01
Fe_2NiAl	30d 600	5.758	–	4.25	117	−0.50	−0.61
Fe_2MnAl	12d 900	5.816	–	1.58	52	−0.23	−0.22
Fe_2CrAl	11d 800	5.805	246	1.67	–	–	–
Fe_2VAl	11d 800	5.761	–	$\chi_g = 1.8x10^{-5}$ emu/g	–	–	–
Fe_2TiAl	11d 900	5.879	123	0.11	–	–	–
Fe_2MoAl	as-cast	5.918	–	0.36	–	–	–
Co_2FeAl	10d 800	5.73	–	4.96	138	−0.73	−0.84
Co_2MnAl	as-cast	5.749	639 a)	4.04	104	−0.08	−0.07
Co_2CrAl	as-cast	5.887	334	1.55	17	−0.02	−0.02
Co_2VAl	as-cast	5.772	310	1.95	27	−0.03	−0.03
Co_2VAl	14d 800	5.847	134 b)	0.74	–	–	–
Co_2NbAl	10d900	5.935	383	1.35	22	0.00	0.01
Co_2ZrAl	3d 1050	6.078	178	0.79	–	–	–
Co_2TaAl	10d 900	5.93	260	1.50	–	–	–
Co_2HfAl	3d 1000	6.045	193 b)	0.82	–	–	–
Ni_2MnAl	8d 900	5.824	$T_N = 30$	–	–	–	–
Ni_2CrAl	sp.c.	5.737	140	0.13	–	–	–
Cu_2MnAl	10d 800	5.968	603	3.60	86	0.00	0.00
Cu_2CrAl	10d 800	5.809	–	$\chi_g = 3.5x10^{-7}$ emu/g	–	–	–

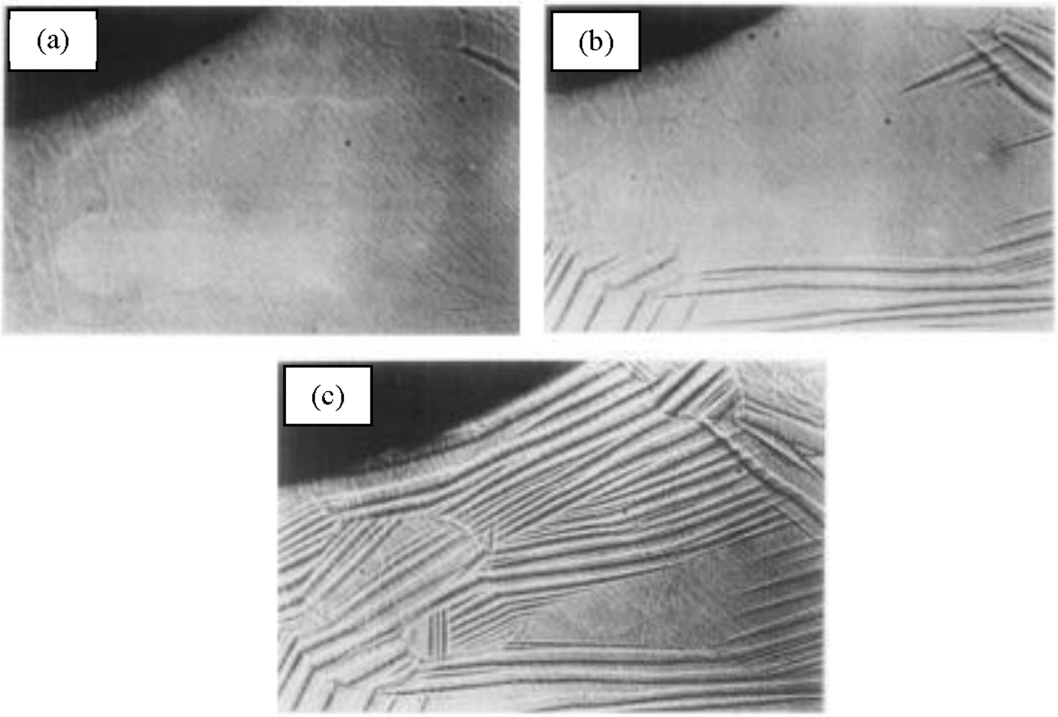

Fig. 8. Microstructure of Ni_2MnGa alloy on cooling. (a) Above 202 K. (b) At 202 K and (c) Below 202 K. (From Webster et al. [83]).

displacement through the application of a magnetic field at a constant temperature. In this scenario, Ullakko et al. [84] induced strains of 0.20 % along the [0 0 1] direction in a non-stressed crystal of Ni_2MnGa, applying a magnetic field of 8 kOe at 265 K. We remind the reader that the measurements of magnetic field intensity in Oersted (H; CGS) and Tesla (B; SI) are related by the equation:

$$B = \mu_r \mu_0 H \tag{2}$$

where μ_r is the permeability of the medium and μ_0 is the permeability of vacuum.

Fig. 9(a) shows the strain gauge and the sample alignment caused by the application of the magnetic field. Fig. 9(b) and (c) present the strain along [0 0 1] due to the fields applied along [0 0 1] and [110] at 283 K (parent phase), and 265 K (martensite phase). It was observed that when the magnetic field has the same orientation as the [0 0 1] direction, i.e., they are in a parallel configuration, the strain is higher than when they exhibit antiparallel alignment. In addition, the strain effect is more pronounced for the martensite phase. The strains are due to the movement of coherent twin boundaries in the martensitic phase. At high temperatures, the Ni_2MnGa alloy has the $L2_1$ cubic lattice (a = 0.5822 nm). The martensite transformation occurs close to 276 K. At low temperatures, the crystal structure evolves from the parent phase through a non-diffusional mechanism that promotes the tetragonal structure (a = b = 0.590 nm, c = 0.544 nm)[85].

In the early 2000 s, Sutou et al. [86] investigated the martensitic and magnetic transformation in Heusler alloys that were Ga-free. The following systems were studied: $Ni_{50}Mn_{50\text{-}y}X_y$ (where X corresponds to In, Sn, and Sb atoms). The transformation temperatures (martensitic and magnetic) were evaluated through differential scanning calorimetry (DSC) and vibrating sample magnetometry (VSM) techniques. Transmission electron microscopy (TEM) identified the martensite phase crystal structure. In addition, X-ray diffraction (XRD) was utilized to determine the lattice of the martensite structure. Fig. 10(a), (b), and (c) show the results of the thermomagnetization curves on cooling and heating for the alloys: $Ni_{50}Mn_{34}In_{16}$, $Ni_{50}Mn_{37}Sn_{13}$, and $Ni_{50}Mn_{37}Sb_{13}$, which were subjected to a magnetic field of 500 Oe. In these curves, martensitic transformation start and finish temperatures are defined as M_s and A_f, respectively. Furthermore, martensitic-to-martensitic transformations are characterized by M_s' and M_s''. The reversible transformation is defined by A_f' and A_f'' while the Curie temperature is designated as T_c. The alloys exhibit the same behavior, i.e., the thermomagnetization curves rapidly rise because of the magnetic transformation from the paramagnetic to ferromagnetic phase during cooling. After that, the magnetization is significantly reduced due to the martensitic transformation and cooling rate change. Sutou et al. [86] explain that this behavior is evidence of a martensite-to-martensite transformation, which appears in all compounds studied. A particular case occurs for $Ni_{50}Mn_{37}Sn_{13}$ alloy (Fig. 10b), in which three stages of martensitic transformation are observed. Fig. 11 shows TEM and XRD of the $Ni_{50}Mn_{37.5}Sn_{12.5}$ alloy at room temperature. The presence of the modulated layer of twins or stacking faults is observed in Fig. 11(a). Furthermore, the extra spots present in Fig. 11(b) indicate that the martensite exhibits an orthorhombic four-layered structure. According to the authors, this type of geometry had not been demonstrated earlier in any other ferromagnetic shape memory alloys.

The magnetocaloric effect (MCE) is a property present in some Heusler alloys. This phenomenon occurs by variation of magnetic

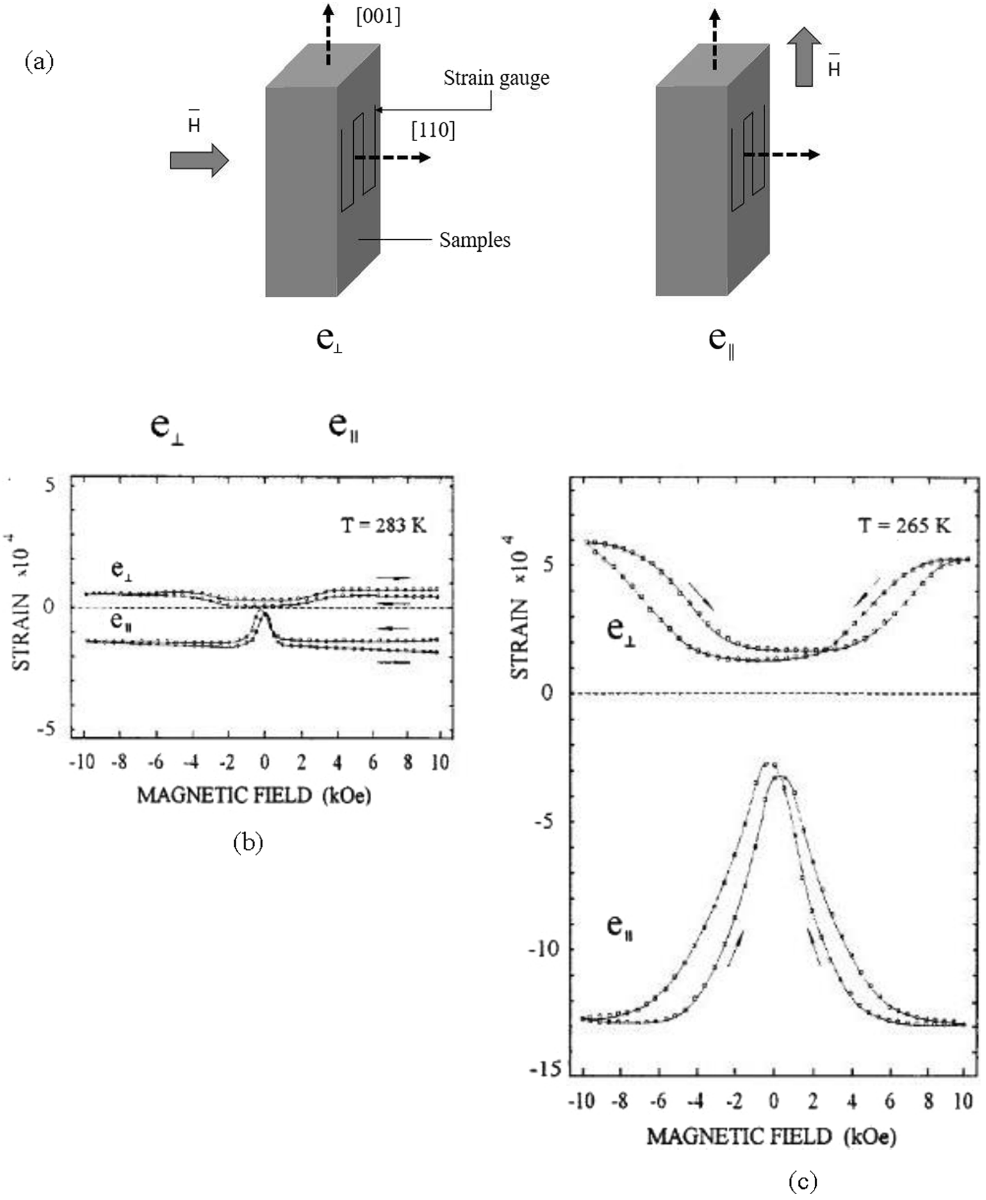

Fig. 9. (a) Schematic drawing of the relative orientation of strain gauge and sample. (b) Strain as a function of the applied field for parent phase, at 283 K. (c) Strain as a function of the applied field for martensitic phase, at 265 K. (From Ullakko et al. [84]).

fields promoting heating or cooling of the materials, due to the temperature change (ΔT_{ad}) in an adiabatic process or by entropy change (ΔS_{iso}) in an isothermal system [87]. The magnetocaloric effect is an intrinsic property of magnetic materials. Furthermore, a large magnetocaloric effect is reached for materials that undergo magneto-structural transition and first-order magnetic transition. This property allowed the creation of a new technology of refrigeration that did not require the expansion and compression of a gas. Fig. 12 shows how the magnetic refrigeration process occurs. In the first stage, a magnetocaloric material is adiabatically magnetized promoting an increase in the temperature. In the second step, additional heat is rejected into the environment, and the temperature of the materials drops. In the third stage, the magnetic field is removed adiabatically; this action causes a decrease in the temperature. In the last step, the cooling is accomplished [88].

Magnetic refrigeration demonstrates several advantages compared to the conventional compression gas method. The cooling efficiency is higher (30–60 % of a Carnot cycle, while for the conventional technique it is 5–10 %) even on a small scale [89]. In addition, magnetic refrigeration does not use corrosive substances (ammonia), ozone-depleting (chlorofluorocarbons and hydrochlorofluorocarbons), or any substances that promote global warming [90,91]. In other words, magnetic refrigeration is considered an environmentally-friendly cooling technology. The magnetocaloric effect is not a unique property found in Heusler alloys. The inverse magnetocaloric [92–99], mechanocaloric [100–103] properties are examples of caloric effects present in these materials. The latter is

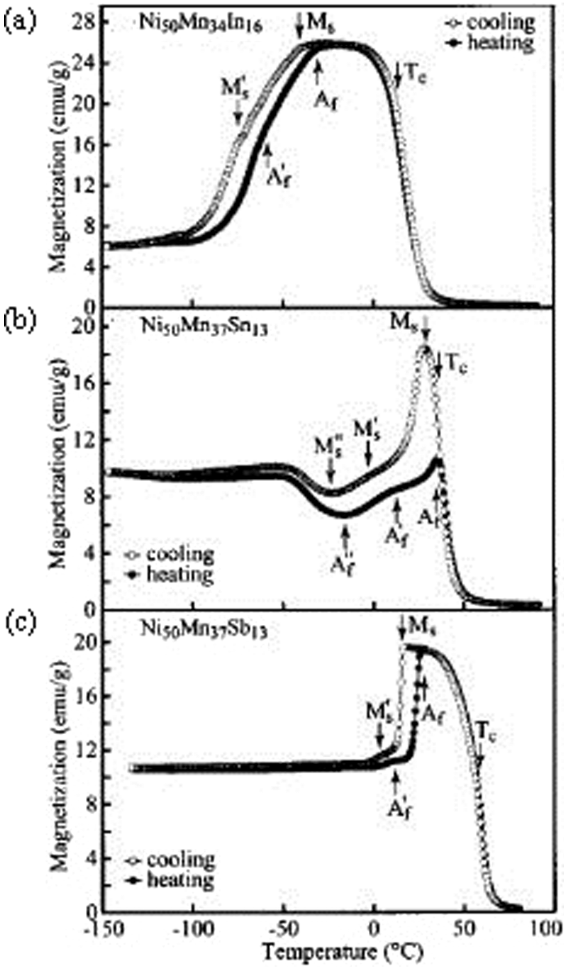

Fig. 10. Measurement of the thermomagnetization curves for (a) Ni$_{50}$Mn$_{34}$In$_{16}$, (b) Ni$_{50}$Mn3$_{7}$In$_{13}$, and (c) Ni$_{50}$ Mn$_{37}$Sb$_{13}$ alloys via VSM. (From Sutou et al. [86]).

divided into barocaloric (pressure) and elastocaloric (elastic uniaxial deformation).

Topological insulators (TIs) are defined as a new state of quantum matter, which exhibits a gapless surface inside the bulk energy gap [104,105]. They can occur in two-dimensional (2D), called quantum spin Hall (QSH), and three-dimensional (3D) states. The first material identified as a 2D topological insulator was CdTe/HgTe/CdTe quantum well [106,107], while Bi$_{1\text{-}x}$Sb$_x$ was the first alloy known as a 3D topological insulator [108]. Investigations led by Felser's group [109–115] revealed that some ternary Heusler compounds can be classified as topological insulators. This new state has gained much attention in diverse areas such as condensed matter physics, chemistry, and materials science with great potential in spintronics and quantum computing applications [109,116,117].

The first investigations on the mechanical properties of the Heusler alloys began in 2016, by Rogl et al. [118]. They evaluated the hardness, elastic moduli, Vickers fracture resistance, and thermal expansion of Half Heusler alloys. They also compared experimental data with density functional theory (DFT) simulations. It was observed, as in most materials, that elastic moduli are dependent on the porosity: they decrease as porosity increases. Furthermore, there is a linear relationship between the Vickers hardness and Young's modulus. It is well known that hardness is proportional to the yield strength; this is the so-called Tabor equation. Regarding fracture resistance, it was demonstrated that this property rises with increasing zirconium/hafnium content. Concerning the thermal expansion, it was concluded that for Half Heusler alloys this parameter shows a linear behavior above 100 K.

Theoretical studies based on atomistic modeling methods and DFT simulations were performed by Everhart and Newkirk [119] to obtain information on the mechanical properties of Heusler alloys. They evaluated various properties such as Young's modulus, shear modulus, bulk modulus, hardness, porosity, and fracture toughness. Through this theoretical investigation, it was possible to predict the mechanical behavior of Heusler compounds and to compare it with other classes of materials (metals and ceramics).

Recently, experimental studies of mechanical properties based on Ni-Mn-In [120,121], and all-*d*-metal Ni-Mn-Ti [103,122] alloys have been conducted since these alloys are promising alternatives to the vapor compression refrigeration cycle, due to their multi-caloric properties. All-*d*-metal Heusler alloys refer to a novel class of Heusler alloys comprised totally of transition metals, i.e, the *p*-

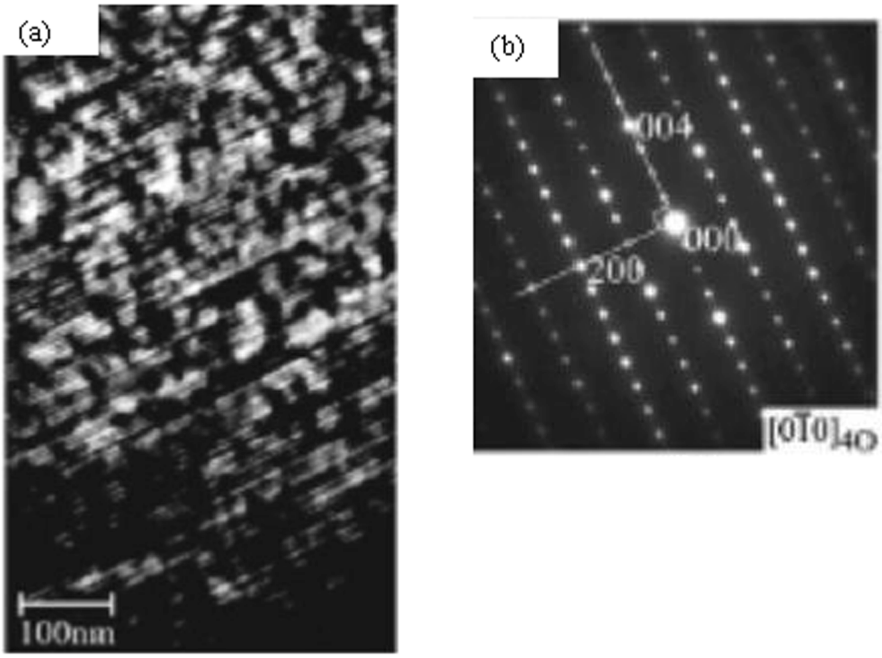

Fig. 11. TEM and XRD analysis for $Ni_{50}Mn_{37.5}Sn_{12.5}$ alloy at ambient temperature. (a) Usual microstructure and (b) Diffraction pattern of martensite phase. (From Sutou et al. [86]).

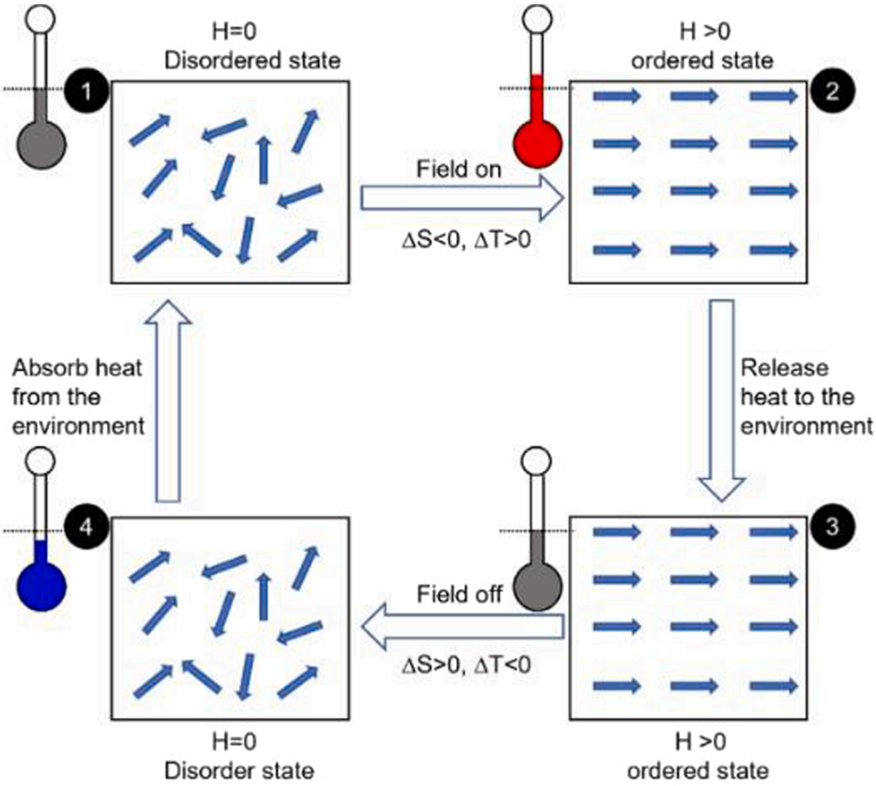

Fig. 12. Diagrammatic representation of magnetocaloric refrigeration principle. (From Yan et al. [317]).

elements of the periodic table (formed by the groups 13, 14, 15) are replaced by *d*-elements (transition metals). Yan et al. [122] demonstrated a high ultimate strength of 1.1 GPa for the $Ni_{50}Mn_{31.7}Ti_{18.25}$ all-*d*-metal Heusler alloy.

3. Classification of Heusler alloys

Ternary Heusler alloys are classified as: Full Heusler, Half Heusler, and Inverse Heusler. Additionally, due to the chemical substitutions and structural variations, Heusler alloys are extended into Binary and Quaternary compounds.

Full Heusler alloys have the general formula X_2YZ (2:1:1), where X and Y atoms are transition metals or lanthanides and Z atoms belong to the main group (III or IV) of the periodic table [119]. Fig. 13 shows the periodic table of each element that forms the Full-Heusler alloys. Usually, the transition metal is the first in the formula, while the main group atom is put at the end, such as Cu_2MnAl, Cu_2MnSn, and Co_2MnGe, Co_2MnSi [123,124]. However, this rule does not apply to compounds in which an element is defined as the most electropositive, as $LiCu_2Sb$. In this case, the most electropositive element is the first in the formula, following the criteria of IUPAC [125]. Full Heusler alloys exhibit the cubic structure $L2_1$ and belong to the space group $Fm\overline{3}m$ number 225. However, depending on the site-disordered state, the Full Heusler alloys can present the B2 (Y-Z disorder) and A2 (X-Y-Z disorder) structures. The basic structure is shown in Fig. 3 and was originally established by Otto Heusler [43] for Cu_2MnAl and Meyers et al. [60] for Cu_2MnSn. Full-Heusler alloys can be characterized by four interpenetrating FCC lattices, two of which are equally occupied by X. In this system, X atoms occupy Wyckoff positions 8c (¼, ¼, ¼), four Y atoms occupy the Wyckoff position 4b (½, ½, ½), and four Z atoms, occupy the Wyckoff position 4a (0, 0, 0), as demonstrated by Otto Heusler [43], Bradley and Rodgers [44]. Graf et al. [6] showed that this structure is known as a zinc blende sublattice, developed by one X and Z atom. The second X atom is located in the remaining tetrahedral voids, while Y is placed in the octahedral holes. The relationship between zinc blende type sublattice and Full Heusler alloys is presented in Fig. 14.

Half Heusler alloys follow the chemical formula XYZ (1:1:1), for instance, NiMnSb and TiNiSn. According to Graf et al. [7], these compounds exhibit covalent and ionic parts, where X and Y elements have cationic character, while Z is the anionic part. X, the most electropositive element, forms a rock-salt (NaCl) sublattice with the main-group atom Z, and this interaction corresponds to a stronger ionic character of their bonding. Y and Z atoms form a zinc-blend (ZnS) sublattice: this indicates covalent bonding [9]. Consequently, the structure of Half Heusler alloys is a sum of zinc blende and sodium chloride lattice, as shown in Fig. 15. The most electropositive atom is located in the first position of the formula; it can be a transition metal, the main group element, or lanthanides. In contrast, the most electronegative atom is placed at the end of the formula: this is a main-group element and belongs to the right side of the periodic table [7]. Fig. 16 presents the periodic table of the elements that composed half-Heusler alloys. These alloys crystallize in cubic structure $C1_{b,}$ belonging to space group $F\overline{4}3m$ number 216 [6]. Half Heusler alloys have a non-centrosymmetric arrangement, which is a ternary ordered modification of the CaF_2 structure and can be obtained from the tetrahedral ZnS structure by filling the empty octahedral lattice sites [7]. Webster and Ziebeck [126] proposed that these compounds can be also represented by four FCC sublattices; however, one sublattice is empty. The atom X is located in Wyckoff positions 4b (½, ½, ½,) the Y atom is placed in the 4c (¼, ¼, ¼), and the Z atom occupies the 4a (0,0,0) position, respectively. Furthermore, it is possible to obtain three different atomic arrangements for this type of structure as presented in Table 3 [6].

Inverse Heusler alloys are derived from Full Heusler alloys. Therefore, they follow the same chemical formula X_2YZ, such as the

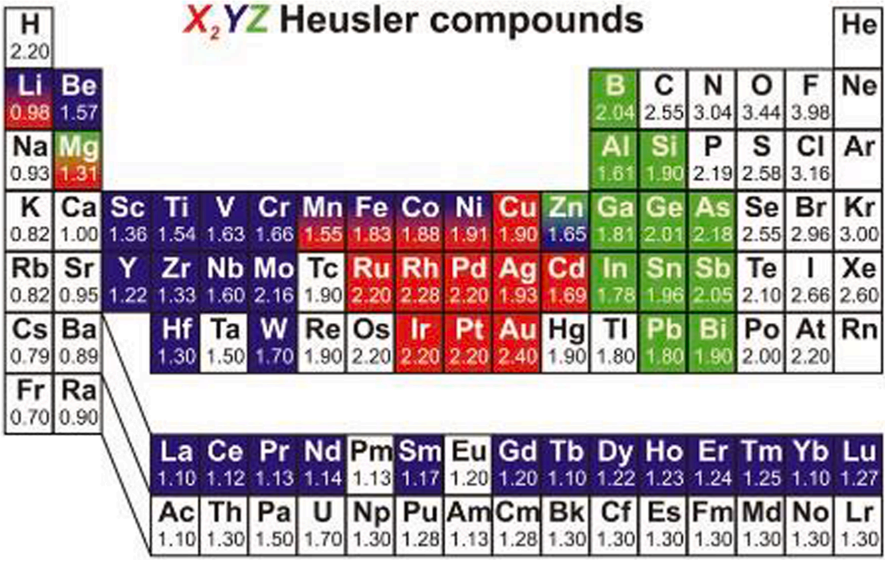

Fig. 13. Periodic table of the elements that form the Full-Heusler alloys (X_2YZ). Red: X; blue: Y; green Z (From Graf et al. [7]). (For interpretation of the references to color in this figure legend, the reader is referred to the web version of this article.)

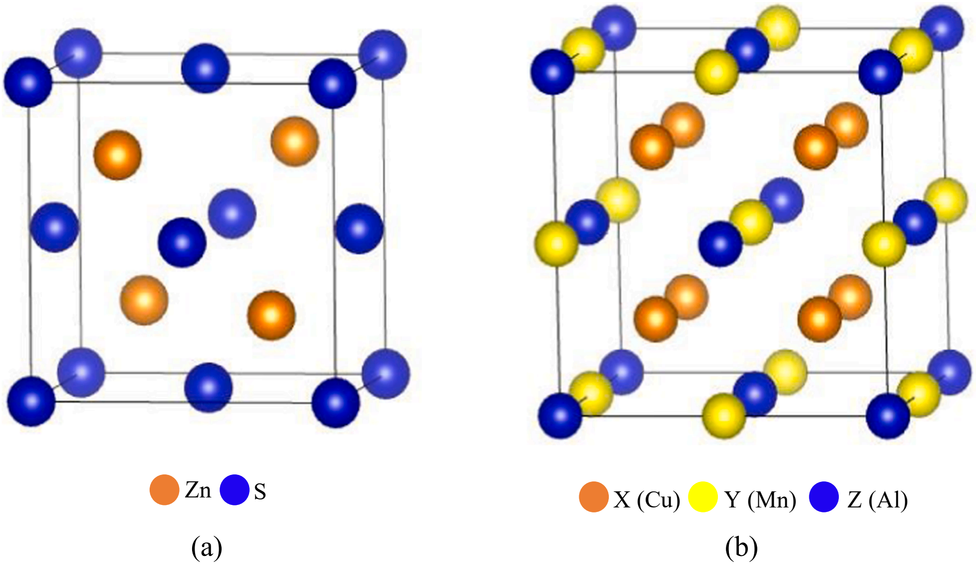

(a)

(b)

Fig. 14. Comparison between ZnS prototype and Full-Heusler. (a) Zinc blend structure and (b) Full-Heusler structure (Cu_2MnAl).

Hg_2TiCu and Zr_2PdAl prototypes [9]. In addition, the atom sequence in this system is X-X-Y-Z and the valence of the Y atom is higher than the X transition-metal element. According to Graf et al.[127], X and Z atoms form a NaCl structure to reach octahedral coordination for X. The other X and Y elements fill up the tetrahedral voids. Although Inverse Heusler alloys originated from Full-Heusler, they crystallize in the XA or Xα structure with $F\bar{4}3m$ symmetry (number 216). These alloys also present four interpenetrating FCC sublattices, but the X elements do not exhibit a simple cubic arrangement. They are located on the Wyckoff positions 4a (0,0,0) and 4c (¼, ¼, ¼), whereas the Y and the Z elements are placed at 4b (½, ½, ½) and 4d (¾, ¾, ¾) [127]. The crystal structure of the Inverse Heusler alloys is shown in Fig. 17.

Binary Heusler alloys exhibit the chemical formula X_3Z (3:1), X being transition metals and Z elements of the main group. These alloys have a face-centered cubic structure $D0_3$-type and present the space group $Fm\bar{3}m$ number 225. In the unit cell of X_3Z, tetrahedral and octahedral coordination are observed, depending on the X atom position. When two corresponding X atoms are encircled by four X and Z atoms, there is a tetrahedral position. Further, when one X atom is surrounded by eight X atoms, an octahedral position is achieved. The atomic sites in the unit cell of these alloys are (¼, ¼, ¼) for X(A), (¾, ¾, ¾) for X(C), (½, ½, ½) for X(B), and (0,0,0) for Z [128]. Fig. 18 presents the $D0_3$-type crystal structure.

As demonstrated by Felser's team [128,129], Binary Heusler alloys display many features, for instance, gapless semiconductors (V_3Al and V_3Ga), gapless half-metallic ferrimagnets (V_3Si and V_3Ge), half-metallic antiferromagnets (Mn_3Al and Mn_3Ga), half-metallic ferrimagnets (Mn_3Si and Mn_3Ge), and a spin gapless semiconductor (Cr_3Al). Due to these features, they are potential candidates for spintronics applications. Other examples of Binary Heusler alloys are Fe_2Z (Z = In, Sn, Sb, and As)[130] and Mn_2Z (Z = As, Sb, As) [131].

The last Heusler alloy family is called Quaternary Heusler, exemplified by LiMgPdSn-type (called of *Y*-type structure), such as CoFeMnSi alloy. Depending on the atom positions, three nonequivalent structures are obtained for the *Y*-type arrangement. The Quaternary Heusler compounds exhibit the chemical formula XX'YZ. However, X and X' are formed by different transition group elements and not by a single element. Another characteristic of these alloys refers to the valence of the elements, in which X atoms have higher valence than X', and Y atoms have a valence lower in comparison to both X and X' elements. The compounds also obey the same symmetry as Half and Inverse Heusler, $F\bar{4}3m$(number 216). Graf et al. [127], explained the fact that the X and X' atoms are located at the Wyckoff positions 4a (0,0,0) and 4b (½, ½, ½), while the Y and Z atoms occupy 4c (¼, ¼, ¼) and 4d (¾ ¾, ¾) positions, respectively. Due to stability along the FCC cube's diagonal, the sequence of atoms in Quaternary Heusler is X-Y-X'-Z. The crystal structure of the Quaternary Heusler alloys is demonstrated in Fig. 19.

The above classification describes the Heusler alloys based on stoichiometry. However, there are numerous Heusler compounds with off-stoichiometric composition. This explains why there are>1,500 Heusler compounds.

4. Electronic and magnetic properties of Heusler alloys

This section is important for the understanding of Heusler alloys since it provides the non-specialist with a good foundation on how to understand the different stoichiometries and how to determine the magnetic properties.

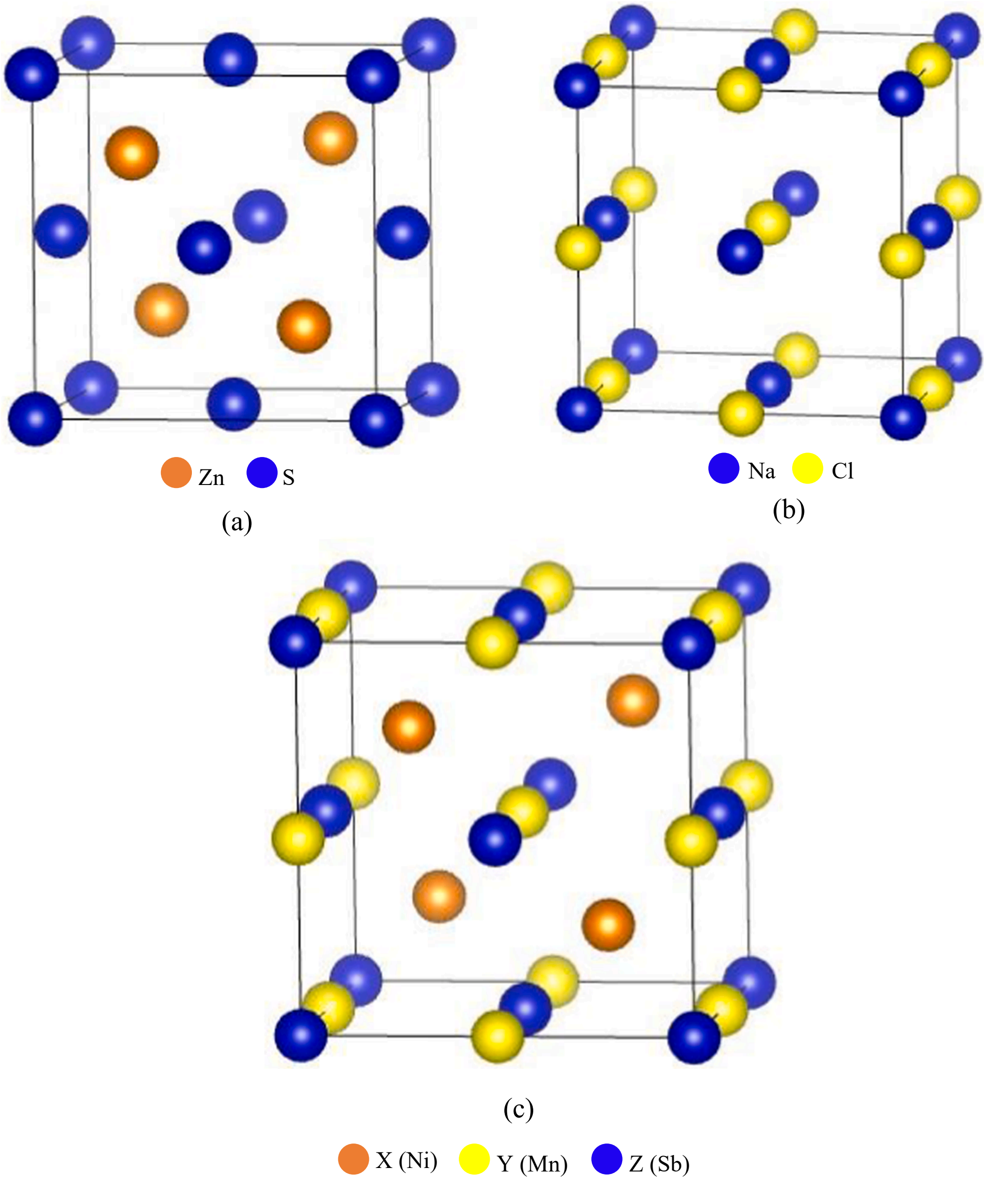

Fig. 15. ZnS and NaCl prototypes and their relationship with the Half-Heusler. (a) Zinc blend structure. (b) NaCl structure and (c) Half-Heusler structure (NiMnSb).

4.1. *Application of the Slater-Pauling rule to ferromagnetic Heusler alloys*

The electronic structure and the magnetic properties of Heusler alloys have been extensively studied due to the unique features of these materials. Understanding the electronic structure is important since the properties of these compounds can be estimated by the valence number. In general, Heusler alloys obey the Slater [132] and Pauling [133] rule. These researchers, working individually, discovered that for binary magnetic compounds, when adding one valence electron, it occupies spin-down states only and the total spin magnetic moment is reduced by about 1μB/f.u. (9.274×10^{-24} J T^{-1}). Notably, analogous behavior occurs in half-metallic Heusler alloys, where the extra valence electron is localized at spin-up states, increasing the total spin magnetic moment by nearly 1μB/f.u. (9.274×10^{-24} J T^{-1}). [71]. This rule demonstrates that the magnetic moment (M) of 3d transition elements can be predicted by the number of valence electrons (Z) per atom. The compounds are classified into two parts according to the electron valence. The first part of the Slater-Pauling curve is the region of low valence electron ($Z \leq 8$) and localized magnetism. Concentrated BCC structures are in this area. The second part is the region of high valence ($Z \geq 8$) and itinerant magnetism. The FCC and HCP structures are found in this region. Iron is situated at the border between localized and itinerant magnetism. Heusler alloys are positioned in the localized part of this curve, as shown in Fig. 20. The total magnetic moment is equal to:

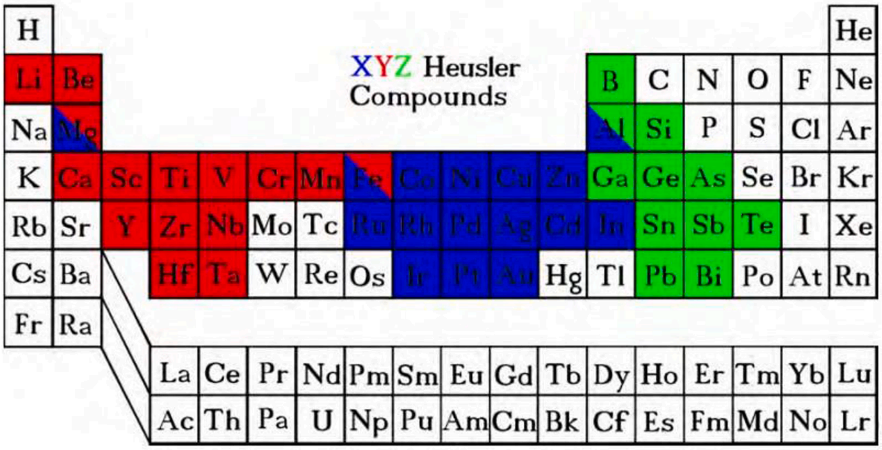

Fig. 16. Periodic table of the different elements that compose XYZ Half-Heusler alloys. Blue: X; red: Y; green: Z (From krez and Balke [318]). (For interpretation of the references to color in this figure legend, the reader is referred to the web version of this article.)

Table 3
Different site occupancies in $C1_b$-type structure. Atoms located on 4a and 4c Wyckoff position form a ZnS sublattice, while the atoms located on 4b fill the octahedral Holes. (From Graf et al. [7]).

	4a	4b	4c
I	X	Y	Z
II	Z	X	Y
III	Y	Z	X

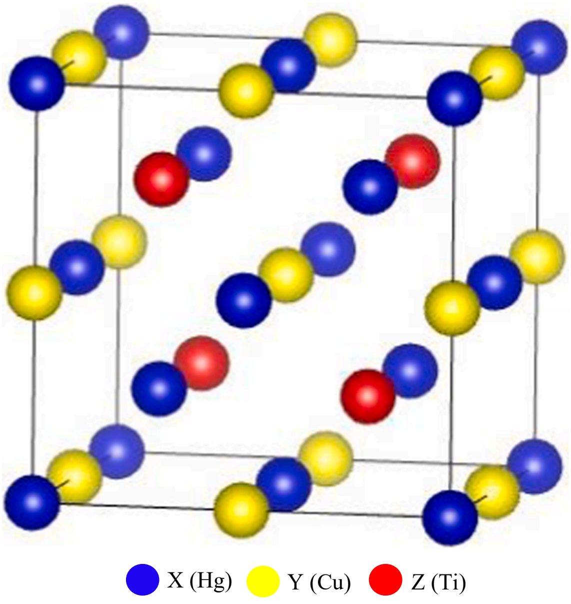

Fig. 17. Inverse Heusler structure (Hg_2CuTi prototype).

$$M_t = Z_t - 2N\downarrow \tag{3}$$

where M_t is the total magnetic moment, Z_t is the total number of valence electrons and $2N\downarrow$ refers to the number of electrons in the minority-spin band configuration. The magnetic moment is generated by electrons spinning around the nucleus, in a similar way to current circulating in a loop.

Half metallic ferromagnetic materials have a band gap in the spin-down density of states at the Fermi level. As a result, the number

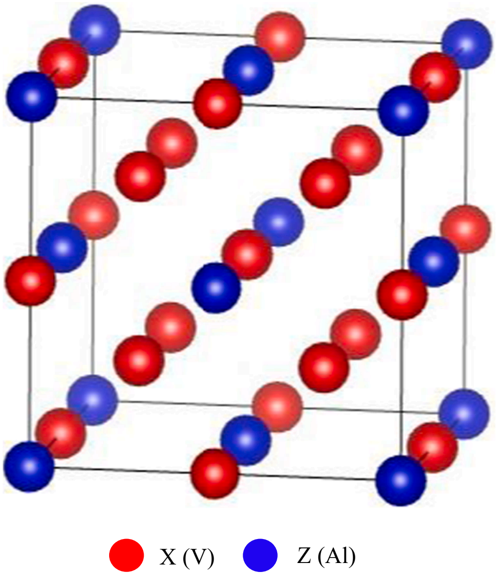

Fig. 18. Binary Heusler structure (V_3Al $D0_3$-type).

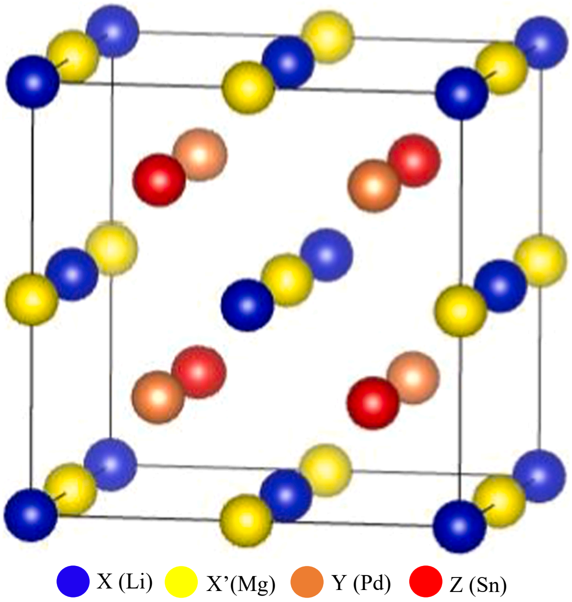

Fig. 19. Quaternary Heusler structure (LiMgPdSn prototype).

of occupied minority states is required to be an integer. However, this rule does not follow the integer number value if the total valence electrons are not an integer. As consequence, it is more appropriate to use the valence electron number per formula unit.

For the Full Heusler alloys ($L2_1$), the minority-spin band exhibits twelve electrons per unit cell. Then the corresponding Slater-Pauling rule is:

$$M_t = Z_t - \tag{4}$$

In the case of Half Heusler compounds ($C1_b$), the minority-spin band exhibits nine electrons per unit cell and the Slater-Pauling rule is:

$$Mt = Z_t - 18 \tag{5}$$

Fig. 21 shows the total spin magnetic moment as a function of the total number of valence electrons for Full Heusler alloys. As can be seen, the maximum magnetic moment for these alloys is approximately 7 μB/f.u. (6.49×10^{-23} J T^{-1}). Fig. 22 presents the same

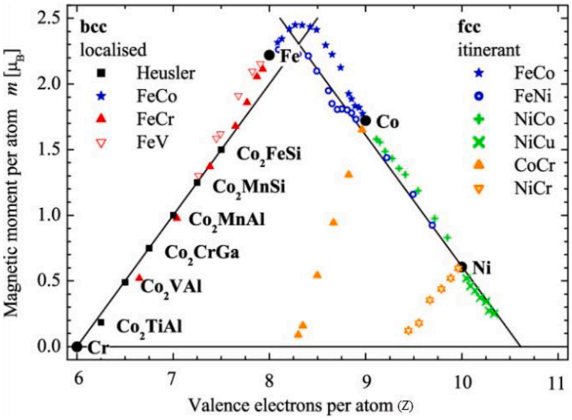

Fig. 20. Slater-Pauling curve for 3d transition metals and their respective alloys. (From Balke et al. [5]).

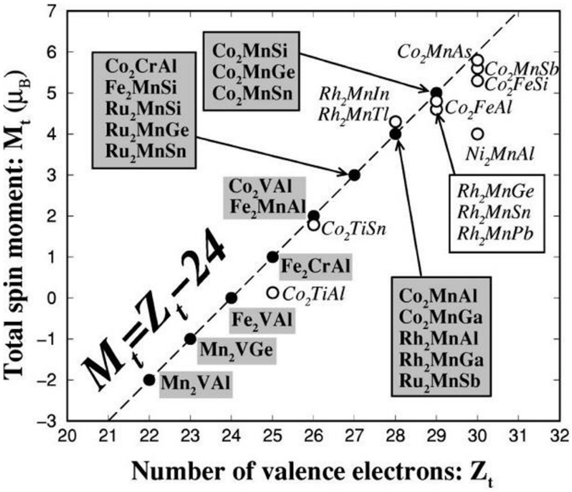

Fig. 21. The total spin magnetic moment for Full-Heusler alloys. The Slater-Pauling rule is represented by the dashed line. Open circles present the alloys that deviate from the Slater-Pauling curve. (From Galanakis et al. [65]).

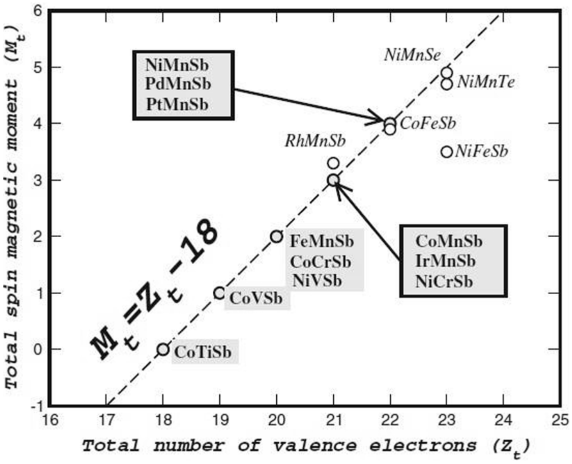

Fig. 22. The total spin magnetic moment for Half-Heusler alloys. The Slater-Pauling behavior is characterized by the dashed line. Compounds that deviate from the Slater-Pauling curve are presented with hollow circles. (From Galanakis et al. [69]).

behavior for Hall Heusler alloys, in which the maximum magnetic moment is equal to 5 μB/f.u. (4.63×10^{-23} J T^{-1}) This behavior indicates that several Heusler alloys can be produced with diverse magnetic moments.

Inverse Heusler alloys (Xα) exhibit three different forms of the Slater-Pauling rule. This interesting behavior depends on the chemical type of the component transition-metal atoms, and the hybridization of the *d*-orbitals of adjacent atoms. The Slater-Pauling rule is given by:

$$M_t = Z_t - 24 \tag{4}$$

$$M_t = Z_t - 18 \tag{5}$$

$$M_t = Z_t - 28 \tag{6}$$

Fig. 23 presents the relationships between the total spin magnetic moments per unit cell of various Inverse Heusler alloys as a function of the number of valence electrons. According to Skaftouros et al. [71], if the X atom is scandium or titanium, the total spin magnetic moment follows Equation 4. Differently, if the X atom is chromium or manganese, the rule is defined by Equation 3. Besides, if the X atom is vanadium, Slater-Pauling's behavior is established as material specific. The last modification of the rule happens when the X atom is chromium or manganese, and the Y atom is cooper or zinc. In this scenario, Cu or Zn *d*-states are completed, thus, they have low energy in comparison to the X *d*-states. Therefore, these alloys follow Equation 5. Furthermore, the authors demonstrated that many alloys described in Fig. 23 are half-metallic ferromagnetic. As a result, they obey the Slater-Pauling rule for the magnetic moment.

For Quaternary Heusler alloys, the Slater-Pauling rule obeys the same relationship as Full-Heusler compounds, i.e., Equation 4 ($M_t = Z_t - 24$). Fig. 24 presents the relationship between the magnetic moment and the number of valence electrons for Quaternary Heusler alloys. The lower magnetic moment values correspond to (CoCr)TiAl and (CoV)TiSi. In contrast, the higher magnetic moment value corresponds to (CoFe)MnAs.

4.2. Antiferromagnetic Heusler alloys

In addition to the ferromagnetism, some Heusler alloys have been found to be antiferromagnetic. Antiferromagnetism, discovered by Néel in 1948 [134], is obtained when the magnetic moments of Mn are in antiparallel alignment. This effect found applications in spin-valves, which are a basic component of hard disk drive read heads. The Mn-Ir alloy is the primary antiferromagnetic component used in these applications: it has a high corrosion resistance and excellent magnetic pinning to adjacent ferromagnetic layers. However, Ir is extremely rare and is listed as a critical raw material by the European Community and the US. Hirohata et al. [135] review the research on antiferromagnetic Heusler alloys and state that the concentration on the earth is 4×10^{-4} ppm, in comparison with Pt (3.7×10^{-3} ppm) and Ru (1×10^{-3} ppm). Iridium belongs to the platinum group and is extremely expensive. Thus, there is a great incentive to find alternative antiferromagnetic materials. This includes Heusler alloys, several of which are known to be antiferromagnetic. The ordered phases of the Ru_2YZ, Ni_2YZ and Mn_2YZ Heusler alloys are antiferromagnetic. Together with an Fe ferromagnetic layer, a pinning strength of up to 680 Oe at 3 K (Ru_2MnGe), 90 Oe at 10 K (Ni_2MnAl) and 120 Oe at 10 K (Mn_2VAl) can be reached. This approaches the pinning strength of the currently used Mn-Ir alloy, 1.4 kOe. Antiferromagnetic materials are important in magnetic recording, spark plugs, and crucibles. Half-metallic Mn_3Al and Mn_3Ga are also promising antiferromagnetic Heusler alloys for spintronic applications [128].

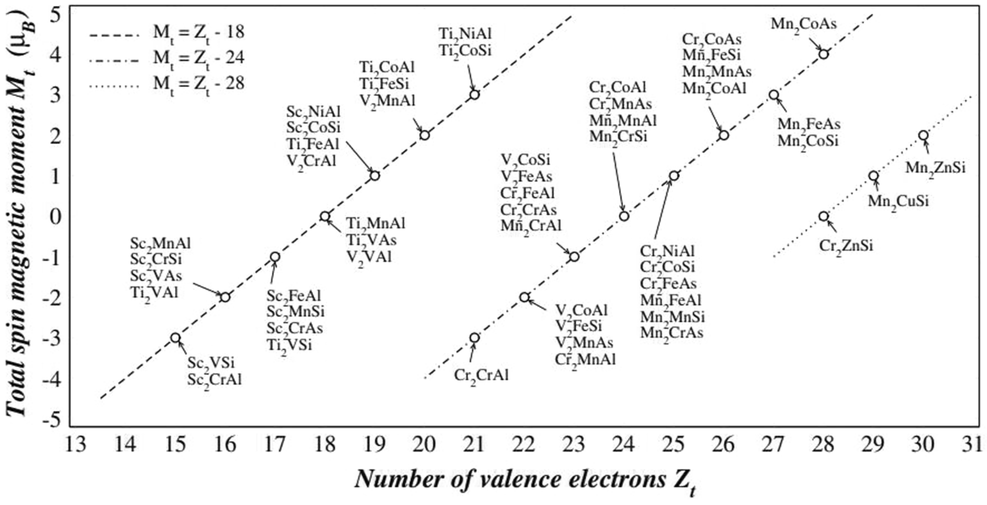

Fig. 23. The total spin magnetic moment for Inverse-Heusler alloys. The Slater-Pauling behavior for three variants is represented by the dashed lines. (From Galanakis et al. [71]).

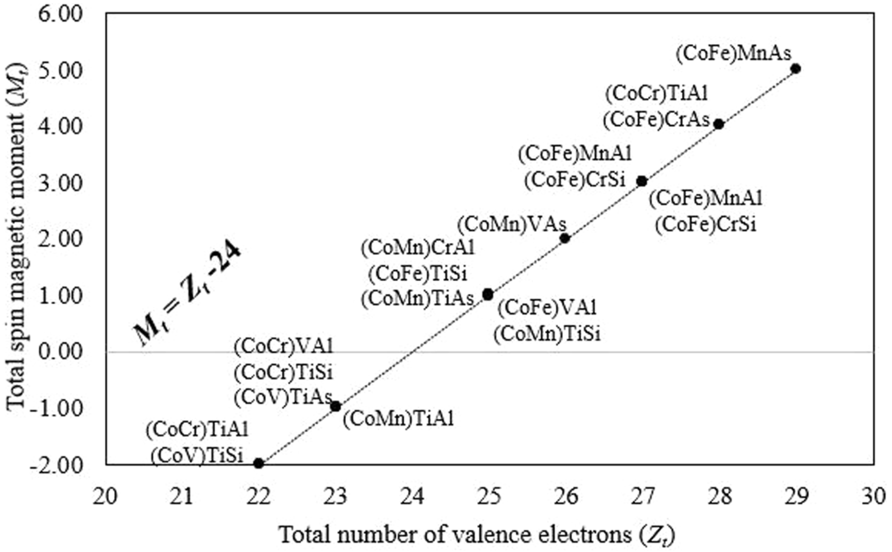

Fig. 24. The total spin magnetic moment for Quaternary-Heusler alloys. The Slater-Pauling behavior is characterized by the dashed line. (Adapted from Galanakis et al. [72]).

5. Half-Metallicity

Half-metallicity is a feature found in materials that display a unique behavior in their spin-band structure. They are described as hybrids between metals and semiconductors. The majority spin-band has a metallic behavior, whereas the minority spin-band shows a semiconducting (or insulator) character with a gap at the Fermi energy (E_F) [136]. Due to the gap, 100 % spin polarization (P) is achieved in these materials. Fig. 25 represents the density of states for half-metallicity materials.

The spin polarization P at the Fermi energy (E_F) is a helpful measure to define the electronic properties. P which is defined as:

$$P = \frac{\rho\uparrow(\in_F) - \rho\downarrow(\in_F)}{\rho_\uparrow(\in_F) - \rho_\downarrow(\in_F)} \tag{7}$$

where $\rho_\uparrow$ (E_F) and $\rho_\downarrow$ (E_F) represent the spin-dependent density of states. The arrows describe the majority and minority states. For paramagnetic or antiferromagnetic materials, even below the magnetic transition temperature, the spin polarization value is neglected. In contrast, for ferromagnetic or ferrimagnetic materials below the Curie temperature, there is a finite value in spin polarization. The electrons at the Fermi energy are completely spin-polarized (P = 1) when either $\rho_\uparrow$ (E_F) or $\rho_\downarrow$ (E_F) is zero [6].

In 1983, de Groot et al. [1] based on ab-initio calculation discovered the half-metallicity behavior for NiMnSb, which is classified as a Half Heusler compound. Fig. 26 shows the density of states calculations for this alloy. As can be seen, there is a gap at the Fermi level located in the minority spin-band. The gap comes from the stable hybridization between the *d* sates higher valence transition atom (Ni) and lower valence transition atoms (Mn), promoting the establishment of bonding and antibonding bands with a gap between them. The bonding band is developed by the atom with the higher valence electrons, while the antibonding state is formed by a lower valence electron atom [64]. Fig. 27 presents the gap for the NiMnSb alloy.

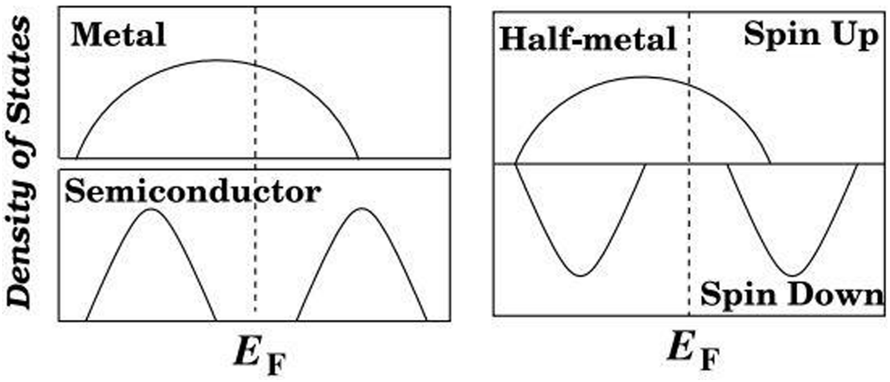

Fig. 25. Illustration of the density of states for a half-metal compared to metal and semiconductor. (From Galanakis and Dederichs [136]).

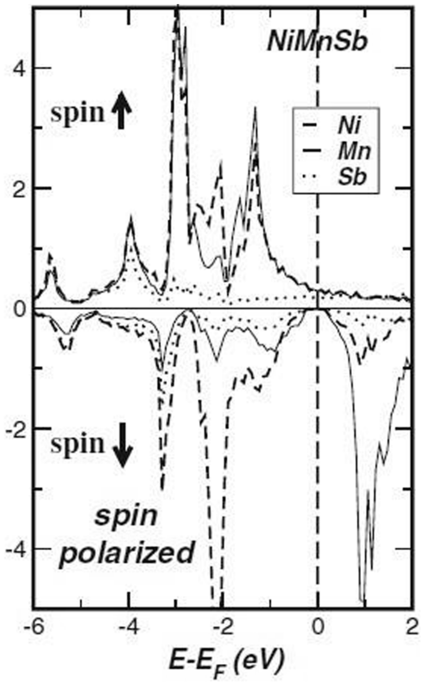

Fig. 26. The density of states calculations for ferromagnetic NiMnSb alloy. (From Galanakis et al. [136]).

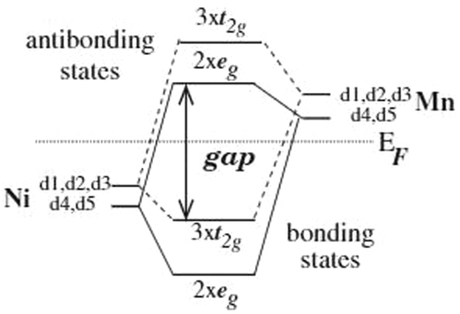

Fig. 27. Development of the gap for minority spin-band in NiMnSb Half-Heusler alloys. (From Galanakis et al. [136]).

After the pioneering work by de Groot et al. [1], many investigations have been carried out to find the half-metallicity in other types of Heusler alloys. Galanakis' group [64,67,69] studied Half Heusler alloys based on X-MnSb (X = Fe, Co, Ni, Cu, Rh, Pd, Ag, Ir, Pt, and Au). Their calculations, based on the density of states, pointed out that only FeMnSb, CoMnSb, and NiMnSb exhibit the half-metallic behavior with a gap in the spin-down channel. In the case of PdMnSb, PtMnSn, and IrMnSb compounds, the Fermi energy slightly indicates non-half metallic properties. For the RhMnSb alloy, the Fermi level falls in the minority valence band leading to the loss of half-metallicity. Table 4 shows the results of spin magnetic moments for XMnSb alloys.

Ksenofontov et al. [75] also studied the half metallicity for CoMnSb alloys. Their experimental work demonstrated through X-ray powder diffraction that the CoMnSb structure is part of the group $Fm\overline{3}m$, instead of $F\overline{4}3m$ as expected for a $C1_b$ type. Furthermore, this

Table 4
Spin magnetic moments (μB/f.u.) for XMnSb Heusler alloys [69].

m spin (μB)	X	Mn	Sb	Void	Total	Half-metallic
NiMnSb	0.264	3.705	−0.060	0.052	3.960	Yes
PdMnSb	0.080	4.010	−0.110	0.037	4.017	No
PtMnSb	0.092	3.889	−0.081	0.039	3.938	No
CoMnSb	−0.132	3.176	−0.098	0.011	2.956	Yes
RhMnSb	−0.134	3.565	−0.144	< 0.001	3.287	No
IrMnSb	−0.192	3.332	−0.114	−0.003	3.022	No
FeMnSb	−0.702	2.715	−0.053	−0.053	1.979	Yes

alloy crystallizes in a superstructure with a supercell containing eight elementary $C1_b$ cells that are built from varying Co_2MnSb and MnSb structural units. The band structure calculations revealed that there is no gap in the density of states, as shown in Fig. 28. These results proved that the CoMnSb compound does not exhibit a half-metallic behavior, as previously considered by Galanakis et al. [67,69].

Half Heusler alloys based on Li atoms have been studied due to their potential applications in optoelectronic and spintronic devices [137,138]. Damewood et al. [82] conducted a series of calculations using the density functional theory to examine the half-metallicity in β-LiMnZ (Z = N, P, and Si) alloys. An investigation in other Half Heusler based on α and γ phases also was carried out. The results demonstrated half-metallic properties for α-LiMnN, α-LiMnP, C-LiMnSi, β-LiMnP, and γ-LiMnSi compounds. In addition, it was shown that the half-metallicity is preserved if the lattice constant is increased slightly. Through the tetragonal cell, it was verified that α-LiMnN, α-LiMnP, and β-LiMnP are antiferromagnetic, whereas the β and γ phases of LiMnSi are ferromagnetic [82].

The half-metallic behavior is not exclusive of Half Heusler alloys. The groups led by Ishida et al. [139,140] and Fujii et al. [141] were the first to predict half-metallicity behavior for Full-Heusler alloys. Ishida et al. [139,140], based on *ab-initio* electronic structure calculations found this behavior in Co_2MnZ alloys (Z represents Si and Ge elements). Fujii et al. [141] observed half-metallicity for Fe_2MnZ (Where Z is Al, Si, and P). Kübler et al. [142] also noticed the half-metallicity for Co_2MnAl and Co_2MnSn alloys. Galanakis et al. [65,69] used first-principles calculations to investigate the half-metallicity and the gap formation in Full Heusler alloys composed of Co, Fe, Rh, and Ru. Their calculations indicated that many alloys studied, such as Co_2MnZ (Z = Al, Si, Ga, Ge, and Sn) compounds, exhibit the half-metallic character. Fig. 29 shows the density of states for these alloys and the presence of the gap in the Fermi energy. Galanakis et al. [65] explain that the origin of the gap in Full Heusler alloys is more complex compared to Half Heusler alloys due to the presence of two X atoms. Fig. 30 presents the gap in the spin-down band for Co_2MnZ compounds. The gap originated from the hybridization of d states occurs between the two atoms of Co. Due to the interaction, d_4 and d_5 orbitals create bonding e_g and antibonding e_u states. Each coefficient ahead of the orbitals is given by the degeneracy. It is important to mention that the d_1, d_2, and d_3 orbitals of each Co atom also hybridize forming triple-degenerated bonding (t_{2g}) and antibonding (t_{1u}) states (Fig. 30 a). Secondly, the hybridization occurs between the two atoms of Co and Mn. The double-degenerated e_g orbitals hybridize with d_4 and d_5 of the Mn atom. Then, they form a double-degenerated bonding (e_g) that exhibits lower energy and an antibonding state which is unfilled and above the Fermi energy. Continuing, the $3 \times t_{2g}$ Co orbitals combine with the d_1, d_2, and d_3 of the Mn and form six new orbitals (three are bonding and occupied, while the remaining are antibonding with high energy). Lastly, the $2 \times e_u$ and $3 \times t_{1u}$ Co orbitals are not able to combine with any of the Mn d orbitals because none of them is transforming with u representations (Fig. 30 b)[65].

Jourdan et al. [81] experimentally demonstrated the half-metallicity in the Co_2MnSi alloy. To show this phenomenon, thin films of Co_2MnSi were prepared and analyzed *in situ* through an ultrahigh vacuum cluster. The first step was to create an epitaxial buffer layer of Co_2MnGa (30 nm) compound on the substrate containing MgO (1 0 0) through radiofrequency technique at room temperature. In the second step, Co_2MnSi (70 nm) was sputtered over it, also by radio frequency at room temperature. Different annealing temperatures (T_a) were utilized to obtain an ordered structure ($L2_1$). Fig. 31 shows the intensities of Co_2MnSi thin film through the high energy electron diffraction (RHEED) and X-ray diffraction (XRD) under different annealing temperatures. The results showed that at low temperatures (T_a = 300 °C) there was an increase in the intensity of the peaks peculiar to the $L2_1$ structure. On the other hand, the XRD showed no (1 1 1) peak for the $L2_1$ order at temperatures lower than 400 °C. This feature, as explained by Jourdan et al. [81] implies that the ordered structure is not present in the thin film bulk, but only at the film surface. The (1 1 1) peak was observed for annealing temperatures above 400 °C. In addition, for temperatures over 500 °C, some Ga atoms, located in the buffer layers, diffused to the Co_2MnSi surface. Besides, the Jourdan et al. [81] determined the spin polarization *in situ* via the spin-resolved ultraviolet-photoemission spectroscopy (UPS) method. Fig. 32 presents the spin polarization of thin films at different annealing temperatures. The results reveal that samples annealed between 300 °C and 450 °C exhibit a higher room temperature spin polarization in the range of 90–93 % of the Fermi level at ambient temperature. This investigation was able to demonstrate the direct observation of half-

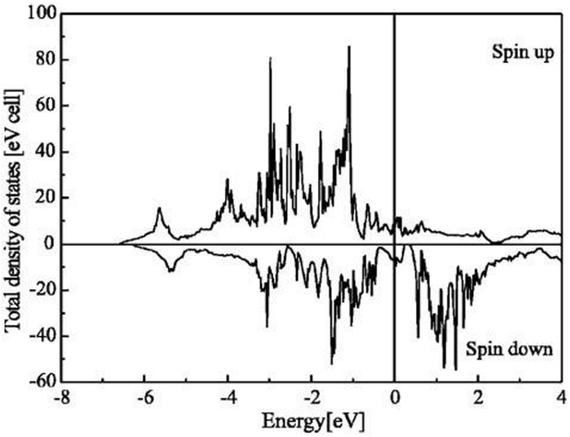

Fig. 28. The density of states (DOS) of ordered CoMnSb calculated by WIEN2K.The Fermi level is indicated by the vertical line. (From Felser et al. [75]).

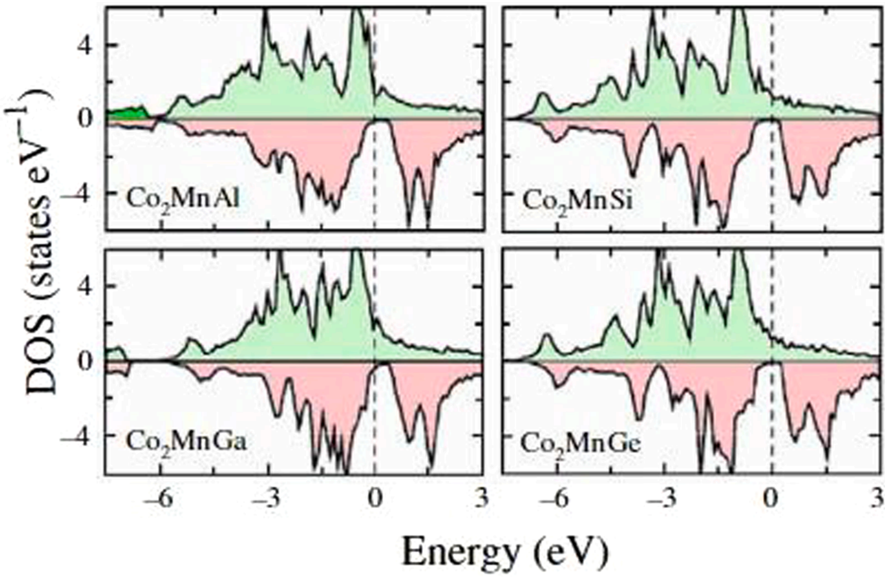

Fig. 29. Density of states calculations for Co_2MnZ alloys (Z = Al, Si, Ga and Ge). (From Galanakis et al. [65]).

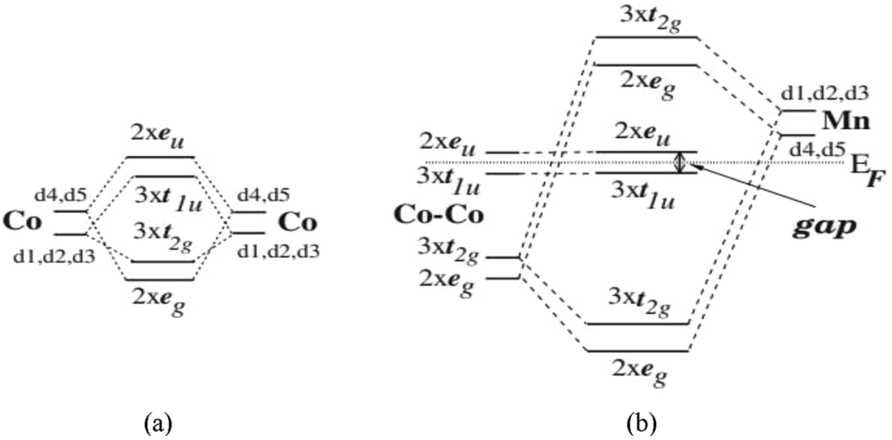

Fig. 30. Schematic of gap formation for Full-Heusler alloys. (a) hybridization between Co-Co atoms and (b) Hybridization between Co atoms and Mn orbital. (From Galanakis et al. [136]).

metallicity on the surface area of a Heusler alloy, providing solid evidence for 100 % spin polarization in the bulk of the thin films.

The half-metallicity in Inverse Heusler alloys has been demonstrated theoretically in several works [143,143–145]. Skaftouros et al. [71], for instance, reported through first-principles calculations the half-metallic behavior for Sc_2CrAl, Cr_2CrAl, Cr_2ZnSi, Ti_2NiAl, Mn_2CoAs, and Mn_2ZnSi compounds. Fig. 33 shows the density of states for these alloys, and as can be observed, the gap is situated in the minority spin-band, as expected for half-metallic materials. As discussed in Section 4, Inverse Heusler alloys follow three different forms of Slater-Pauling rules. As a result, the gap formation depends on the chemical composition of the compound. For example, if the X atoms are Cr or Mn, the *d* states energy position of the Cr^A (Mn^A) and Y atoms are closer, and the antibonding minority-band t_{1u} states are filled like in the Full Heusler alloys. Fig. 34 shows the gap for Inverse Heusler alloy based on Cr or Mn atoms.

The half-metallicity behavior is demonstrated in some Quaternary Heusler alloys. Dai et al. [77] developed an experimental investigation to search for half-metallicity in the CoFeMnSi compound. The samples were produced by arc melting and analyzed by the XRD. The magnetic properties and band structure calculations also were measured. As explained in Section 3, Quaternary Heusler alloys of LiMgPdSb-type exhibit three non-equivalent structures. Thus, three different structures are expected for the CoFeMnSi alloy, designated Type I, Type II, and Type III; they are indicated in Table 5. The density of states calculations in Fig. 35 reveals that the Fermi level of type I CoFeMnSi has an energy gap of 0.75 eV located in the minority band channel. Type II exhibited an electronic structure similar to type I, but the Fermi level leads to a pseudo gap. As can be seen from Fig. 35, the type III structure does not show any gap in the spin-down state, indicating that for this atomic arrangement the half-metallicity is destroyed. Through theoretical and experimental analyses, Dai et al. [77] demonstrated that type I and type II structures present the half-metallic behavior, whereas type III

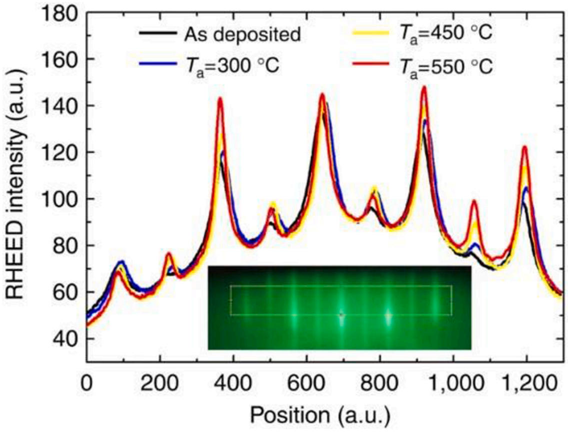

Fig. 31. Co_2MnSi (1 0 0) thin films' intensities analyzed by high energy electron diffraction (RHEED). The yellow (internal) rectangle corresponds to the intensities of samples at different annealing temperatures (T_a). (From Jourdan et al. [81]). (For interpretation of the references to color in this figure legend, the reader is referred to the web version of this article.)

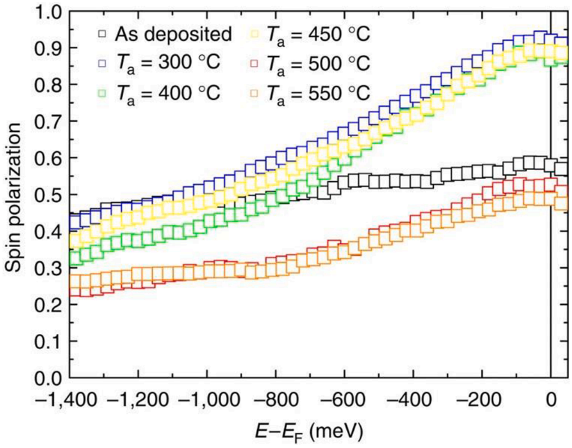

Fig. 32. Spin polarization measured via *in situ* spin-resolved ultraviolet-photoemission spectroscopy (SRUPS). (From Jourdan et al. [81]).

displays metallic character. In addition, it was demonstrated that among the three types of structure, type I is energetically favorable for CoFeMnSi with 100 % spin polarization, being considered a candidate in spintronics applications.

Alijani et al. [79] investigated both experimentally and theoretically the half-metallicity for CoFeMnZ (Z = Al, Ga, Si, and Ge) Quaternary Heusler compounds. The samples were synthesized by arc melting, and the electronic properties were analyzed through X-ray photoelectron spectroscopy. Three nonequivalent atomic arrangements occur for these alloys since they belong to a *Y*-type structure. The half-metallicity for all compounds was investigated via *ab-initio* calculations. The results demonstrated that CoFeMnAl, CoFeMnGa, CoFeMnSi, and CoFeMnGe are half-metallic materials with a gap located at the spin-down channel. Fig. 36 shows the structure and density of states for CoFeMnAl and CoFeMnSi compounds as well as the gap located at the minority spin band.

Özdoğan et al. [72] developed a theoretical investigation of sixty LiMgPdSn- type alloys based on *ab-initio* electronic structure calculations. The results demonstrated that forty-one compounds exhibit the half-metallicity property, nine compounds are semiconductors, and eight alloys are classified as spin gapless semiconductors. As demonstrated by this research, many Quaternary Heusler alloys present the half-metallic behavior making them strong candidates in spintronic and magnetoelectronic applications.

As mentioned earlier, half-metallicity is one of the most important phenomena in the Heusler alloys. This property has a strong influence on the crystal structure. In disordered arrangements, such as B2, A2, and $D0_3$, the half-metallicity is drastically affected [146,147]. The major challenge in Heusler alloys is to produce thin films in an ordered structure to maintain the half-metallicity. This property is not exclusive to Heusler alloys. Some oxides (Fe_3O_4 and CrO_2)[148], double perovskites (Sr_2FeReO_6)[149], pyrites (CoS_2) [148], and others are examples of half-metallic compounds. These materials attract much attention for application in spintronic devices. Heusler alloys, in special, are the most attractive because of their relatively high Curie temperature [136].

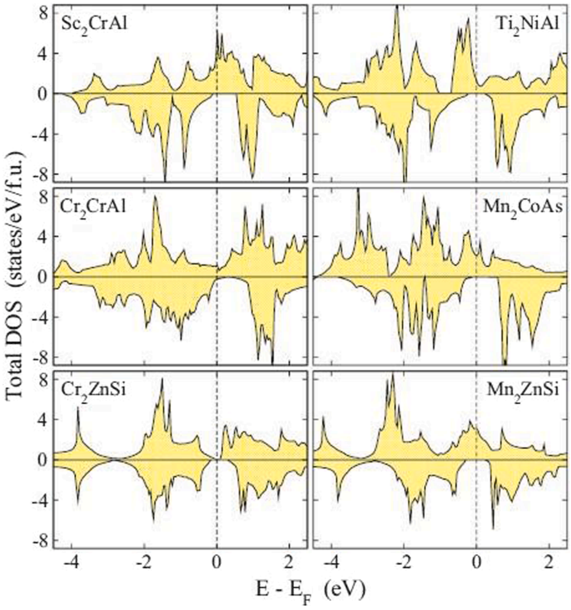

Fig. 33. Density of states calculations for Inverse Heusler alloys. (From Skaftouros et al. [71]).

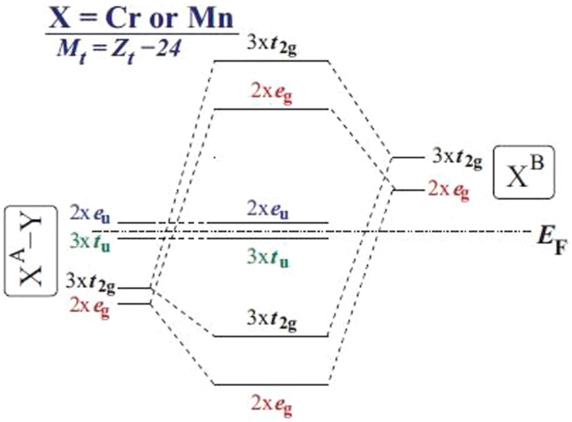

Fig. 34. Hybridization and origin of the gap for Inverse Heusler alloy based on Cr or Mn atoms. (From Skaftouros et al. [71]).

Table 5
Different site occupancies in Y-type structure [77].

	4a	4b	4c	4d
I	Fe	Mn	Co	Si
II	Mn	Fe	Co	Si
III	Mn	Co	Fe	Si

6. Spintronics and Heusler alloys

Spintronics or spin electronics is a new field of solid-state physics, discovered in the past 30 years, which explores the influence of spin currents on electrical conduction [150]. Electrons are characterized by having two important degrees of freedom (DOF): electron charge and spin. In conventional electronic devices, the information is conducted and stored exclusively by the electron charge. On the other hand, spintronic devices apply the spin of the electron to carry and store information [151,152]. Compared to conventional electronic devices, spintronics demonstrated several advantages such as universal memory, reduction in electric power, rise in data processing rate, and increase integration densities. The discovery of the giant magnetoresistance effect (GMR) initiated studies on spintronics technology [153].

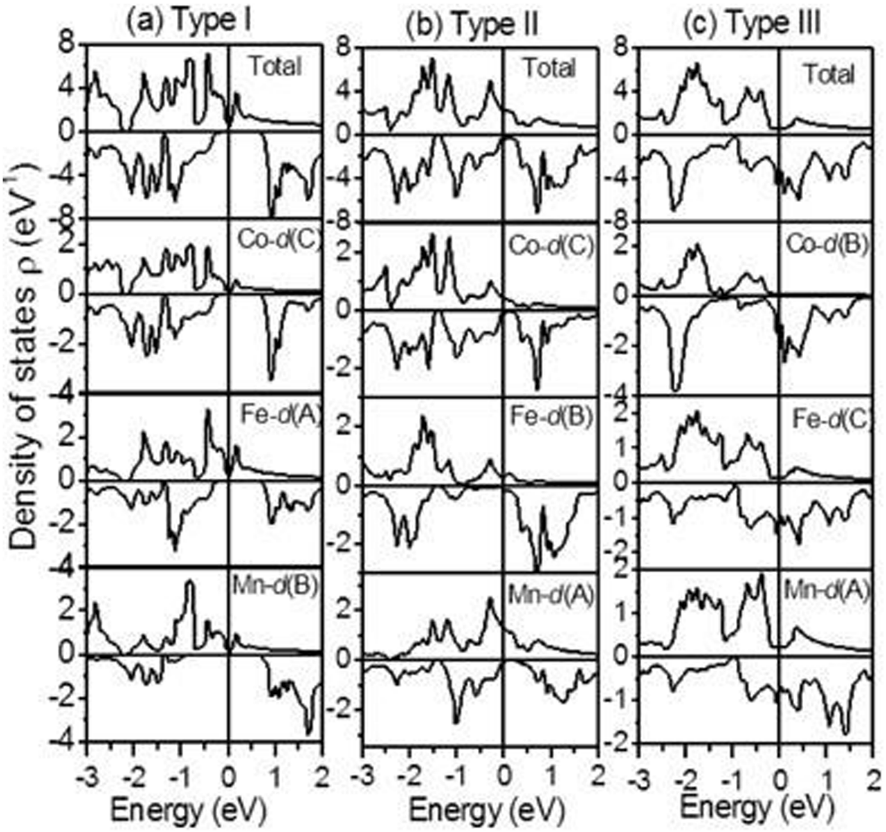

Fig. 35. Density of states for different types of CoFeMnSi alloys. (From Dai et al. [77]).

The magnetoresistance (MR) effect was discovered independently by Peter Grünberg's group [154] and Albert Fert's group [155], in 1988. This discovery transformed the scientific community, in special, computer science. In 2007, Grünberg and Fert received the Nobel Prize in Physics due to this breakthrough [156]. The GMR structure is formed by two or more thinner magnetic layers, which are separated by a nonmagnetic material. This structure can occur in two geometries: current-in-plane (CIP) or current-perpendicular-to-plane (CPP). In the first case, the electric current flows parallel to the layers while for the CPP, the electric current is perpendicular to the layers. Fig. 37 presents the CIP and CPP geometries.

A drastic reduction in the electrical resistance is reached if the magnetic multilayers exhibit the same orientation of the magnetization. As a result, the spin of the electron can flow through the device without finding any barrier. In contrast, if these magnetic layers have an antiparallel configuration of the magnetization, a higher electrical resistance is achieved. Fig. 38 (a) shows the GRM multilayers system while Fig. 38 (b) illustrates the change in the resistance due to the configuration of ferromagnetic layers. In 1997, the first application of spintronic devices based on the giant magnetoresistance effect was introduced by IBM [157], in the hard disk drive (HDD) read heads. Fig. 39 presents the read-head hard drive based on the GMR effect. Two properties are vital to building the new generation of ultrahigh density HDDs: ultra-low resistance-area (RA) and large magnetoresistance (MR) ratio. Fig. 40 shows potential materials for HDD read-head applications. The magnetoresistance ratio is defined as:

$$MRratio = \frac{\Delta R}{R} = \frac{R_{AP} - R_P}{R_P} \tag{8}$$

where R_P and R_{AP} correspond to the resistance measured for parallel and antiparallel systems of the ferromagnetic magnetizations.

Nowadays most HDD read heads produced use spintronics and many experimental works have been conducted in this field. Nakatani et al. [158] based themselves on the current-perpendicular-to-plane giant magnetoresistance to produce thin films of Quaternary Heusler alloy ($Co_2Fe(Al_{0.5}Si0_{.5})$) with Ag as a space layer in a crystalline substrate (MgO-001). The results showed a magnetoresistance ratio of 80 % and the resistance change-area product (ΔRA) equal to 17 m $\Omega\mu m^2$ at 14 K, while at room temperature the MR and the ΔRA were 34 % and 8 m $\Omega\mu m^2$ in a B2-structure. Chen et al. [159] studied the epitaxial growth current-perpendicular-to-plane GMR devices using a Si (0 0 1) wafer rather than MgO (0 0 1) substrate, which is costly for mass production and non-compatible with the current manufacturing techniques. They produced Quaternary Heusler ($Co_{49.3}Fe_{24.6}Ga_{12.9}Ge_{13}$)-based CCP-GMR that grew up on the NiAl buffered Si (0 0 1) substrate. The NiAl as a buffer layer offers several advantages due to its excellent thermal stability (melting point equal to 1620 °C), small lattice mismatch with Si substrate, and excellent lattice mating (<1%) with Co-Heusler alloys [160,161]. The magnetoresistance ratio and the resistance change-area product at room temperature obtained by

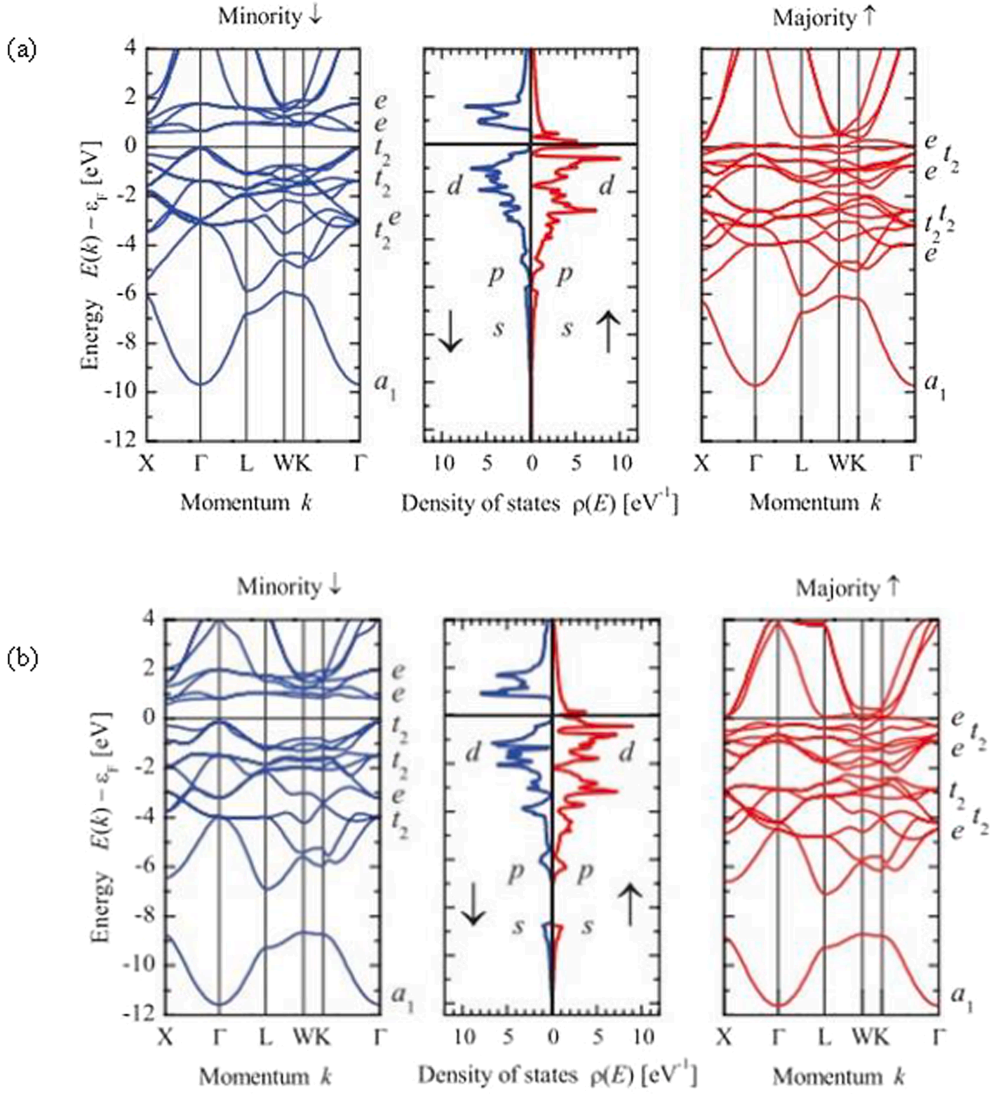

Fig. 36. Density of states for Quaternary Heusler compounds. (a) CoFeMnAl and (b) CoFeMnSi. The blue lines represent the densities in the minority-spin band. The red lines represent the densities in the majority spin-band. The arrow up represents the spin-up densities while the arrow down represents the spin-down densities. (From Alijani et al. [79]). (For interpretation of the references to color in this figure legend, the reader is referred to the web version of this article.)

Chen et al. [159] were 27.8 % and 8 m Ωμm^2, similar to Nakatani et al.'s [158] results.

Chen et al. [162] produced Heusler films through CPP-GMR on Si (001) substrate with CoFe/NiAl buffer layers. They used a three-dimensional (3D) integration process, called direct wafer bonding, to join the film to a poly-crystalline electrode. This process allows for achieving better quality in epitaxial CPP-GMR films grown on the Si (001) substrate. Fig. 41(a) shows the cross-section image by high-angle annular dark-field scanning transmission electron microscopy (HAADF-STEM) of a CPP-GMR film on the Si (001) wafer and the poly-crystalline electrode while Fig. 41(b) presents the bonding interface between them. As observed in the image, the epitaxial structure of CPP-GMR was bonded on the poly-crystalline electrode. Furthermore, the structure layers were homogeneous, and the bonding interface did not exhibit any defects. The resistance change-area was 9.54 m Ωμm^2, and the magnetoresistance was equal to 37.1 %, higher than previous work.

Another progress related to spintronics was the development of tunnel magnetoresistance (TMR), which is a magnetoresistive effect present in a magnetic tunnel junction (MTJ). The magnetic tunnel junction is formed by two magnetic electrodes which are separated by an ultrathin insulation spacer [163]. The substitution of a non-magnetic layer with insulating materials increased the magnetoresistance by ten times compared to the GMR spin-valve [7]. The alteration of the resistance due to the tunneling magnetoresistance effect depends on the magnetic configuration of the electrodes. A parallel configuration of two electrodes leads to a low resistance state. As a result, the spin currents can flow without obstacles. However, if the electrodes are in antiparallel alignment, a high

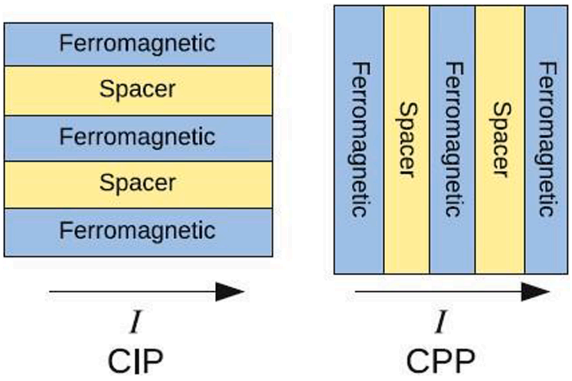

Fig. 37. Different designs of Giant Magnetoresistance (GMR) devices. (From Zhang and Butler [319]).

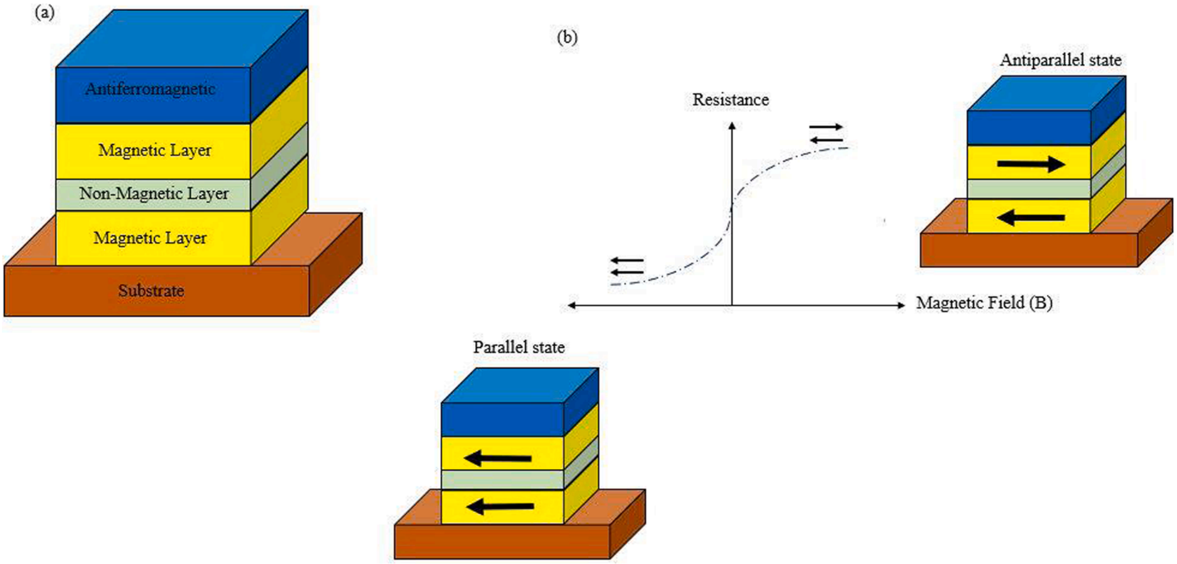

Fig. 38. (a) Giant Magnetoresistance system (GMR), and (b) Effect of magnetic field on resistance. In a parallel state, low resistance is accomplished. In the Antiparallel state, high resistance is achieved.

resistance state is reached. Consequently, the tunneling current is drastically decreased. Fig. 42 (a) shows the MTJ system and Fig. 42 (b) the change in the resistance due to the configuration of two ferromagnetic electrodes.

The first investigation of tunnel magnetoresistance was reported in 1975 by Jullière [164]. In 1982, Maekawa and Gäfvert [165] also studied this effect. However, these initial studies did not advance since it was not possible to replicate them. In 1995, the groups led by Moodera [166] and Miyasaki [167] reproduced a large tunnel magnetoresistance (around 24 %) utilizing an ultrathin tunnel barrier made of oxidized aluminum at 4.2 K. Sakuraba et al. [168] obtained a high tunneling magnetoresistance of 570 % at 2 K and 67 % at 300 K in Co_2MnSi (electrode)/Al-O (barrier). Fig. 43 presents the high-resolution images of the Co_2MnSi/Al-O/Co_2MnSi structure by transmission electron microscopy (TEM). No defect was observed in the film, and the MTJ exhibited a remarkable smooth and flat morphology. Furthermore, the interface between the aluminum oxide and the Heusler alloy was very flat and sharp.

From these important contributions, new investigations were performed to improve the magnetic tunnel junction to obtain a higher magnetoresistance at room temperature. The replacement of a magnetic tunnel junction made of amorphous materials (oxidized aluminum barrier) to a magnetic tunnel junction of a single-crystal (oxidized magnesium) [169] is an example. Fig. 44 shows the progress in tunnel magnetoresistance ratios based on AlO_x and MgO barriers with both the traditional ferromagnets and the Heusler alloys as electrodes. In 2004, a larger tunnel magnetoresistance (~200 % at room temperature) in magnetic tunnel junction using a MgO barrier was demonstrated by Tsukuba [170] and IBM [171]. An outstanding work conducted by Ikeda et al. [172] demonstrated a tunnel magnetoresistance up to 604 % at room temperature, using an electrode of CoFeB and MgO barrier. Since 2007, the read heads of hard disks based on the giant magnetoresistance were replaced by magnetic tunnel junctions, because a higher magnetoresistive effect is achieved in this system. IBM [173] was the first company to produce a magnetic random-access memory (MRAM) sensor applying the tunneling magnetoresistance effect. Fig. 45 presents the MRAM based on magnetic tunnel junction.

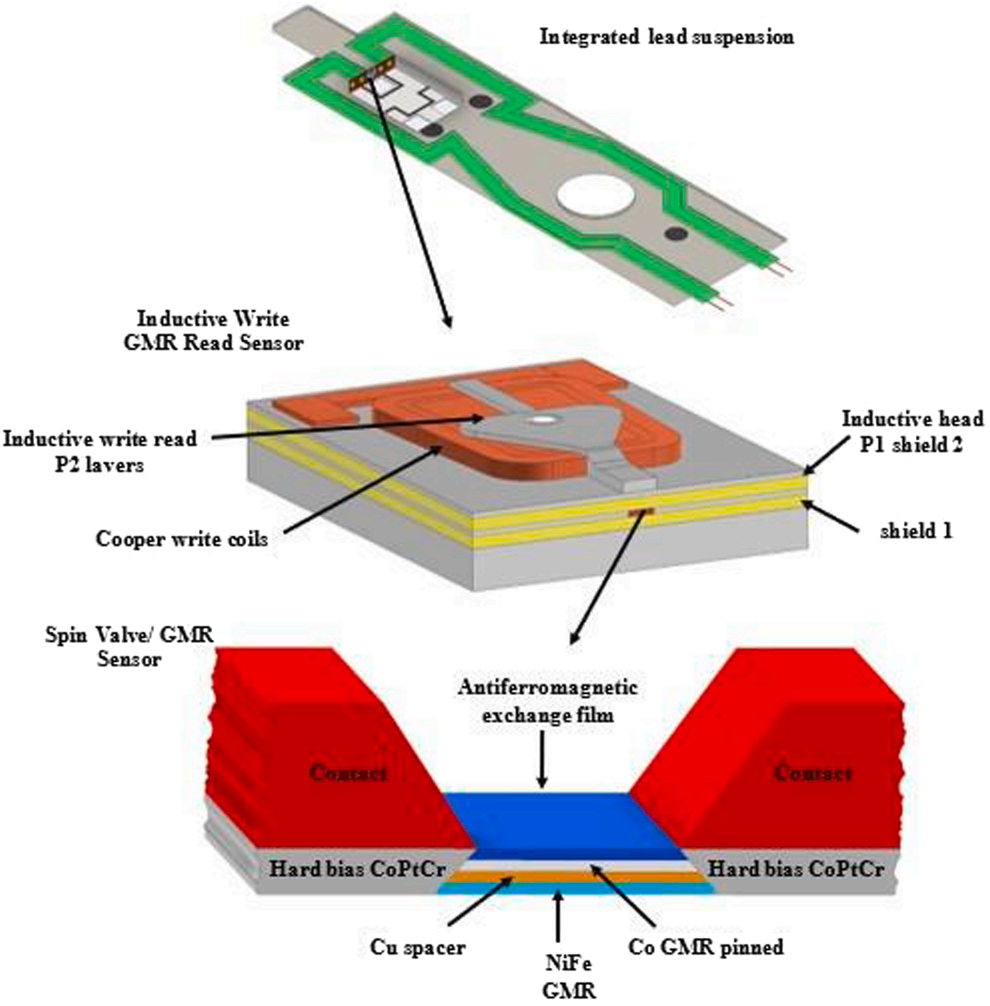

Fig. 39. Schematic of the read-head hard drive disk based on giant magnetoresistance (GMR) effect. (Adapted from Baibich et al. [155]).

The most important aim of spintronics is to develop devices with a maximum tunneling magnetoresistance effect. This goal can be achieved in two different manners: The first is designing an insulation barrier [174]. The second is to replace a conventional magnetic electrode with 100 % spin-polarized materials, such as half-metallic ferromagnetic oxides [175] and half-metallic ferromagnetic Heusler alloys [176]. In this scenery, Co_2YZ Heusler alloys (Y is a transition metal and Z is the main group element), in special, have attracted much attention for applications in spintronic due to their half metallicity and high Curie Temperature [139,177,178]. Thin films of these alloys have been extensively explored in magnetic tunnel junctions in arrangement with a MgO barrier [176,179]. Inomata et al. [180] produced a film by epitaxial growth of Quaternary Heusler alloy, $Co_2FeSi_{1-x}Al_x$, on the MgO (0 0 1) substrate for magnetic tunnel junctions. Fig. 46 shows the TEM at low and high magnifications of the multilayer structure. A good quality morphology of the magnetic tunnel junction with a smooth interface between the electrode and the barrier was observed at low magnification. Excellent epitaxial plane matching was achieved for upper and lower Heusler alloy and MgO barrier, as demonstrated by high magnification. The magnetoresistance values obtained were 200 % at room temperature, and 380 % at 5 K. In addition, the XRD results demonstrated that the (1 1 1) intensity of the $L2_1$ structure was formed in the film at annealing temperatures (T_a) higher than 450 °C, whereas the B2 structure was formed by annealing below 400 °C. Fig. 47 presents the XRD patterns.

Wang et al. [181] fabricated fully epitaxial magnetic tunnel junctions through Co_2FeAl (electrode) and MgO (tunnel barrier) on a MgO (0 1 1) substrate by a sputtering technique. The results showed a tunneling magnetoresistance of 330 % at room temperature in a B2-structure, making this alloy a strong material for building spintronic devices. Liu et al. [182] reported a tunnel magnetoresistance above 1,995 % at 4.2 K and 354 % at 290 K for epitaxial $Co_2MnSi/MgO/Co_2MnSi$ magnetic tunnel junctions. Liu et al. [182] explain that the giant tunnel magnetoresistance achieved is due to two interdependent factors: the half-metallicity of Co_2MnSi electrodes, and the coherent tunneling contribution of the MgO barrier. Fig. 48 shows the cross-sectional image of Heusler compound MTJ structure layers by high-resolution TEM. Fig. 48 (a) shows each layer that forms the MTJ structure, which grew epitaxially; no damage was detected. Fig. 48 (b) and (c) illustrate the lower and upper Co_2MnSi electrodes by nano-beam electron diffraction patterns. The 111 spots indicate the $L2_1$ structure, while the 022 indicate B2 arrangements. From these results, the $L2_1$ structure is present in both the

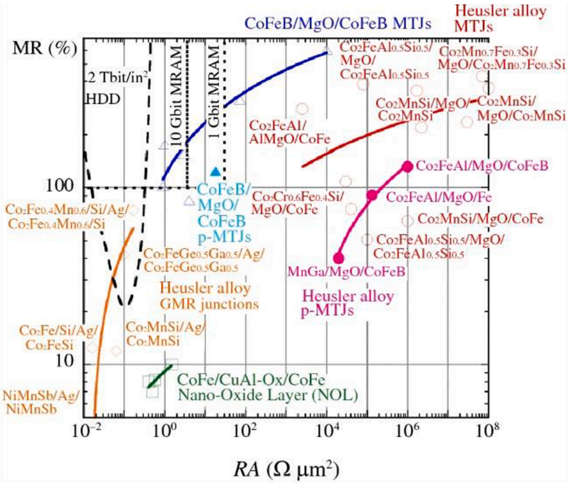

Fig. 40. Magnetoresistance versus the electrical resistance of surface for several magnetic tunnel junction (MTJ) and Giant Magnetoresistance (GMR) materials. Heusler alloys are in red; orange symbols are for Heusler alloys for the Giant Magnetic resistance (GMR) effect. The plot also shows the regions for 1 and 10 Gbit/in^2 memory density for the hard disk drives. 2Tbit/in^2 is for the HDD read heads. (From Hirohata et al. [157]). (For interpretation of the references to color in this figure legend, the reader is referred to the web version of this article.)

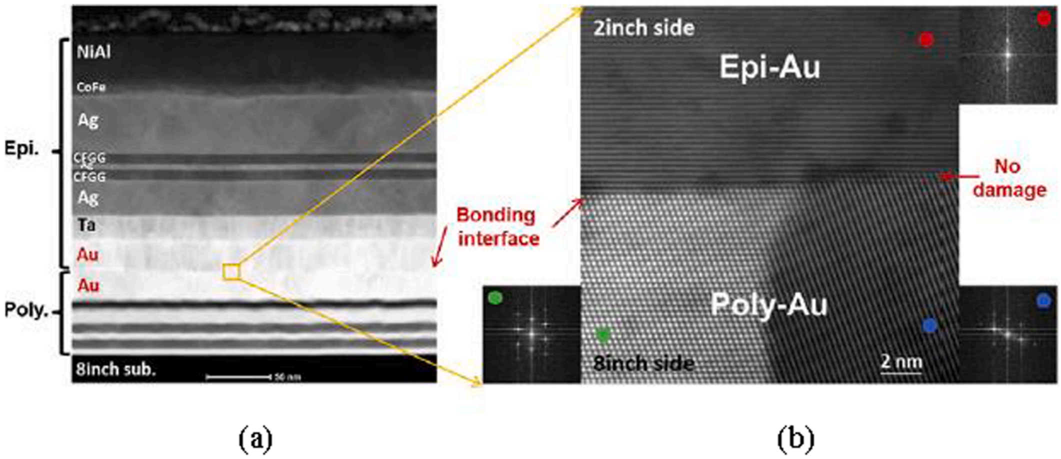

Fig. 41. (a) Cross-sectional image via HAADF-STEM of polycrystalline and epitaxial grown Heusler alloy. (b) Bonding interface area at high magnification in HAADF-STEM. (From Chen et al. [162]).

lower and upper layers. Recently, Kabanov et al. [183] produced a magnetic tunnel junction film using Full Heusler alloys, as a free layer. The magnetoresistance obtained at room temperature was 149 %. Co_2FeSi alloy has received much attention in the spintronic field owing to the high Curie temperature (1100 K), highly spin-polarized transport, and large saturation magnetization (~6 μB/f.u.; or 5.56×10^{-23} J T^{-1}) [73]. Therefore, Co_2FeSi ($L2_1$-ordered) films demonstrate attractive properties for combination into the magnetic sensor as well as memory device due to the low Gilbert damping (0.0018), moderate magnetic anisotropy, and high exchange stiffness (31.5p J/m) [184–186].

The fundamental challenge of the spintronic industry is developing new technologies and devices. Two examples are included in these tasks: fourth-generation magnetic random-access memory (MRAM) and energy-assisted magnetic recording. To achieve these requirements, new materials, notably Heusler alloys with half-metallic nature, are essential. For the new generation of MRAM, is necessary a ferromagnetic Heusler alloy that exhibits huge spin-orbital torque and/or magnetic anisotropy voltage control to achieve low energy magnetization reversal. For the second device, a ferromagnetic Heusler alloy exhibiting a high magnetic anisotropy followed by low damping constants is required to reach fast magnetization reversal at the free magnetoresistance junction [187].

7. All-*d*-Metal Heusler alloys

Conventional Heusler alloys are characterized by the covalent bond between the main group (*p*-group) and the transition metals (*d*-group) elements, thus forming a *p*-*d* Hybridization [188]. On the other hand, all-*d*-metal Heusler alloys are formed only by transition

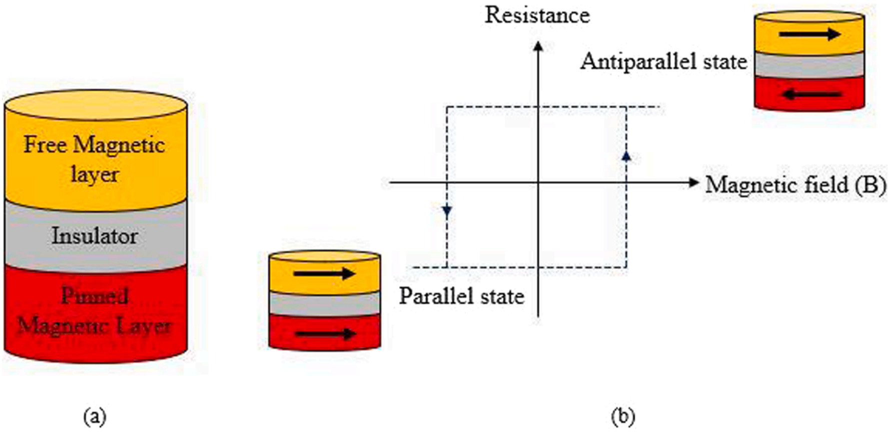

Fig. 42. (a) Magnetic tunnel junction (MTJ). (b) Effect of magnetic field on resistance. In a parallel configuration, low resistance is achieved. On the other hand, in an antiparallel state, high resistance is reached.

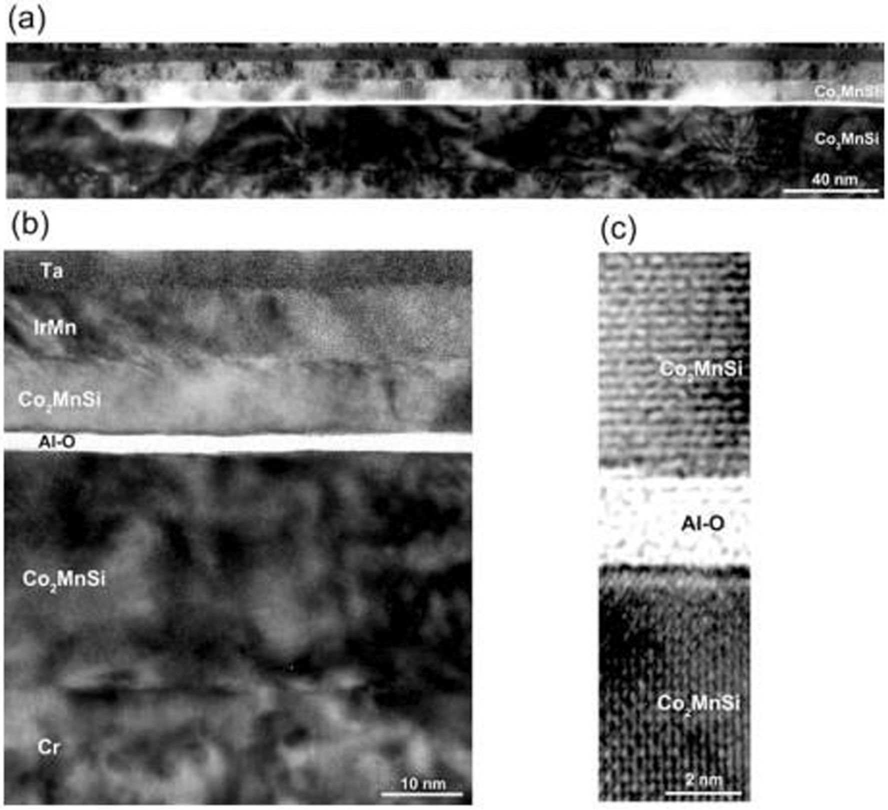

Fig. 43. (a) Low-magnification image of Magnetic tunnel junction via TEM technique in Co_2MnSi/Al-O/Co_2MnSi film. (b) and (c) Upper and lower Co_2MnSi layer at high magnification. (From Sakuraba et al. [168]).

metals. As a result, the covalent bonds form a *d-d* hybridization. Fig. 49 illustrates the difference between conventional and all-*d*-metal Heusler alloys in terms of chemical elements and hybridization.

In conventional Heusler alloys, the *p-d* hybridization has a strong effect on the magnetic response, atomic ordering, and stabilization of the parent phase [188]. The *d-d* hybridization influences the martensite transformation, as reported by Roy et al. [189]. Martensite transformation plays an important role in shape memory alloys and other magnetic compounds. The first investigations of all-*d*-metal Heusler alloys are attributed to Muldawer [190] in 1966 and Murakami et al. [191] in 1980. These authors studied the crystal structure and magnetic properties of $AuAgZn_2$ and $CuAuZn_2$ alloys. Using X-rays, they demonstrated ordered ($L2_1$) and disordered (B_2) structures for both compounds. In addition, they display a nonmagnetic behavior, invalidating their application as

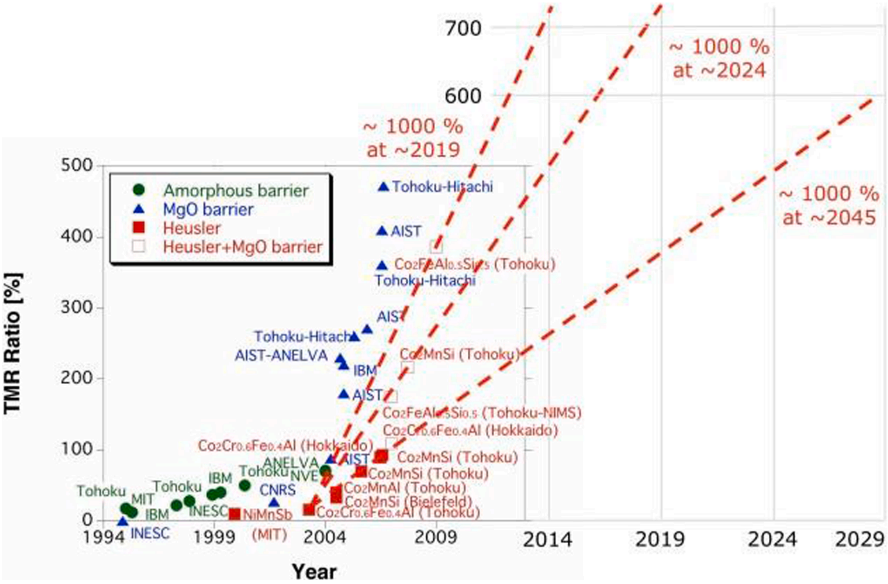

Fig. 44. Development in tunneling magnetoresistance ratios (From Hirohata et al. [320]).

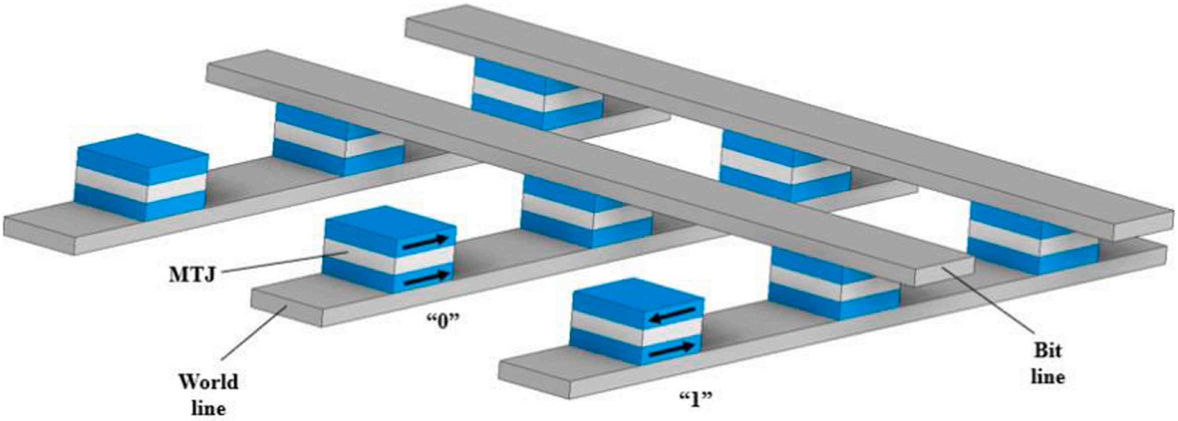

Fig. 45. Schematic drawing of magnetic random-access memory (MRAM) based on magnetic tunnel junction. 0 (parallel) and 1(antiparallel) represent the binary information. (Adapted from Chappert et al. [321]).

ferromagnetic shape memory alloy.

Surprisingly, in 2015 Wei et al. [188] reported that ferromagnetic shape memory alloys (FSMAs) in Heusler states are formed by only 3*d* metals. In the first stage, they added Ti to the binary alloy NiMn, creating a ternary compound, Ni-Mn-Ti. The Ti atom promotes the formation of the Heusler phase through *d*-*d* hybridization between Ni/Mn and Ti. In the second step, through the addition of Co atoms, strong ferromagnetism was reached and FMSAs were produced in the $Ni_{50\text{-}x}Co_xMn_{50\text{-}y}Ti_y$ system.

In a subsequent investigation, Wei's group [192] studied the magnetostructural martensitic transformation followed by volume change and magneto-strains in the $Mn_{50}Ni_{40\text{-}x}Co_xTi_{10}$ all-*d*-metal Heusler alloy. They observed that Ti atoms were responsible for the formation and stabilization of the Heusler alloys. Besides, the magnetostructural transformations were promoted through Co atoms which produced local ferromagnetic Mn-Co-Mn arrangements. A large magneto-strain equal to 6900 ppm and a volume change of −2.54 % were obtained for the $Ni_{50\text{-}x}Co_xMn_{50\text{-}y}Ti_y$ all-*d*-metals alloy. The authors explain that after phase transformation no cracks were observed in the samples because of the high mechanical toughness promoted by *d*-*d* hybridization in these alloys. Fig. 50 shows the volume changes ($\Delta V/V$) by the martensite transformation strain for some Heusler alloys and other ferromagnetic shape memory alloys. $Mn_{50}Ni_{30.5}Co_{9.5}Ti_{10}$ synthesized by Wei et al. [192] has a higher volume change and strain compared to conventional Heusler alloys and other shape memory alloys such as NiTi and FePt that underwent a martensitic transformation.

After the results obtained by Wei et al. [188,192], several research groups studied the properties of all-*d*-metal Heusler alloys [193–196]. This new class of Heusler alloys has received much attention due to its high mechanical properties and potential application in solid-state refrigeration, since these alloys undergo a first-order phase transition. Section 9 presents some examples of all-*d*-

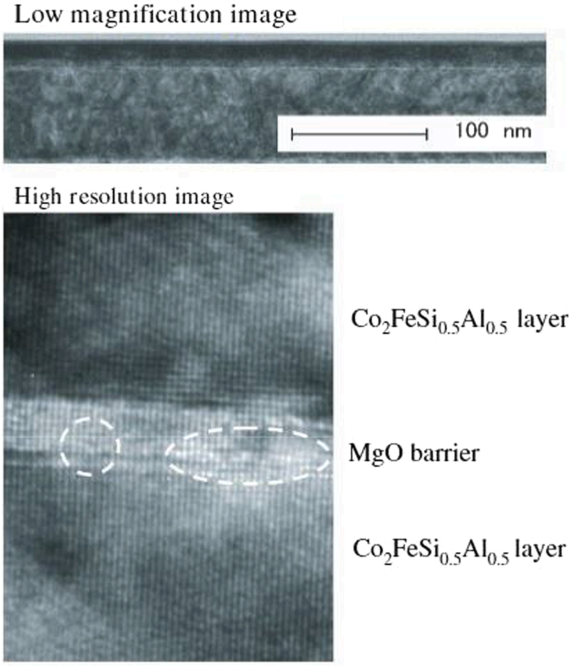

Fig. 46. TEM cross-sectional images with low (top) and high-magnifications (bottom) of Heusler alloy electrode and MgO barrier with magneto-resistance of 220% at room temperature. (From Inomata et al. [180]).

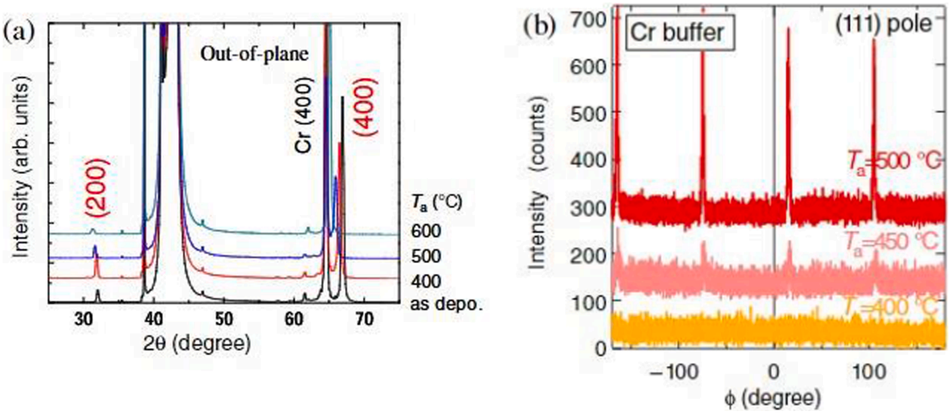

Fig. 47. XRD patterns of Quaternary Heusler alloy films deposited on a Cr-buffered MgO substrate at different post-annealing temperatures. (a) out of plane spectra for 30 nm thick specimen. (b) The (1 1 1) intensity scans. (From Inomata et al. [180]).

Heusler alloys for applications in solid-state refrigeration and Section 11 shows the mechanical response for these new Heusler alloys.

8. Magnetic shape memory alloys

It was observed by Korenko and Cohen [197] in the 1970 s that magnetic fields can accelerate the martensitic transformation in iron-nickel alloys both by increasing the Gibbs free-energy difference between the product and parent phases and by allowing the reaction to take place at higher temperatures.

Magnetostriction is the spontaneous deformation of a solid in response to its magnetization. Martensitic transformations also produce a spontaneous deformation of a solid, upon lowering the temperature. Since the martensitic transformation can also be induced by a magnetic field, magnetostriction can be generated in this manner. In the Ni_2MnZ system (Z: Ga, Al, In, Sn, Sb), the martensitic transformation, shown in Fig. 51, creates the *L*10 tetragonal structure. This martensitic transformation has an associated strain. James and Wuttig [198] developed a theory for magnetostriction in a highly cited paper. Fig. 52 shows his theory, compared with experimental results for Fe_3Pd. It is also applicable to Heusler alloys. The martensitic crystallography and magnetic structure of

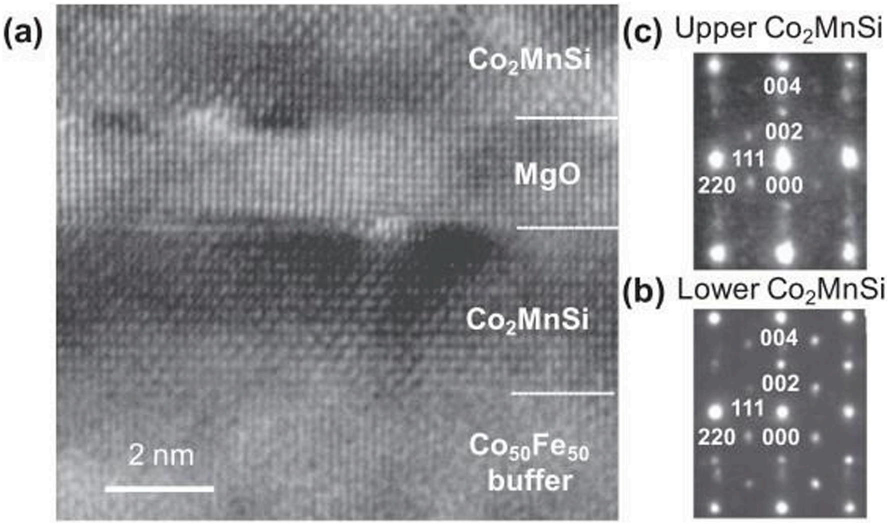

Fig. 48. (a). Cross-sectional image by high-resolution TEM of CoFe/Co_2MnSi/MgO/Co_2MnSi magnetic tunnel junction multilayers. (b) and (c) Nano-beam electron diffraction patterns for the lower and upper Heusler compound electrodes. (From Liu et al. [182]).

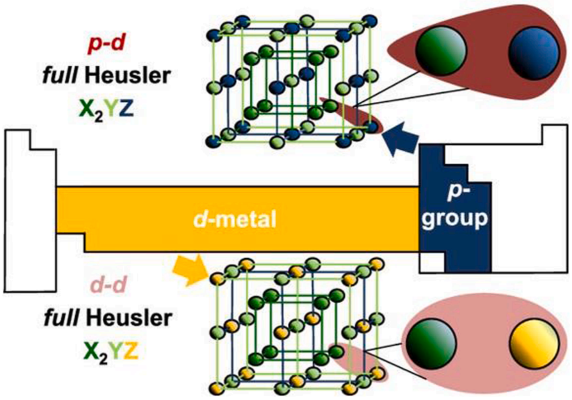

Fig. 49. Difference between conventional Heusler alloys and all-*d*-metal Heusler alloys. Conventional Heusler alloys are formed by transition metals (*d*-metals) and main group (*p*-group) which is presented by Z atoms (D sites) All-*d*-metals Heusler are formed exclusively by transition metals, which means the Z atoms are also a transition metal (D sites). (From Paula and Reis [322]).

Ni_2MnGa are similar to those of Fe_3Pd, but with apparently different easy axes. Other interesting alloy systems for the study of the magnetostriction of martensite are Heusler alloys near the composition Ni_2MnGa. This magnetoelastic effect was apparently discovered by Vasil'ev et al. [199] but is widely attributed to Ullakko et al. [84]. Chernenko et al. [200] investigated systematically 23 compositions close to the stoichiometric Ni_2MnGa and found large differences in the M_s temperature. Ullakko et al. [84] demonstrate field-induced strains of 0.2 % in Ni_2MnGa.

Mn-based Heusler alloys are known to undergo a martensitic transformation from a high-temperature $L2_1$ or B2 crystal structure to a low-temperature one having less symmetry: tetragonal, orthorhombic, or monoclinic (*L*10, 10 M, and 14 M). Such a transformation for Ni_2MnGa is shown in Fig. 51. The magnetism of the two phases is quite different and these alloys are known to exhibit a range of effects under the influence of magnetic fields, stresses, or pressure. Two of these effects are the magnetic shape effect (MSE) and the superelastic effect (SE). These magnetic shape memory alloys have an analogous classification to the stress-driven SMAs. These are the shape memory and the superelastic effects. In conventional SM alloys, the austenite is transformed to martensite by virtue of the external stresses.

There is additional complexity in the SME. In the martensitic state, the sample is composed of several structural domains; two of them are shown in Fig. 53. Below the Curie point, there are magnetic domains within each martensitic variant with the magnetization pointing along the easy axis and organized in such a way that they minimize the magnetostatic energy. Upon the application of a magnetic field, the magnetic moments will align with this applied magnetic field. If the magnetic anisotropy is weak, the magnetic moments will rotate within each martensitic variant. This will result in almost no change in the sample dimensions other than those corresponding to conventional magnetostriction. However, if the magnetic anisotropy is high, rotation of magnetic domains requires a

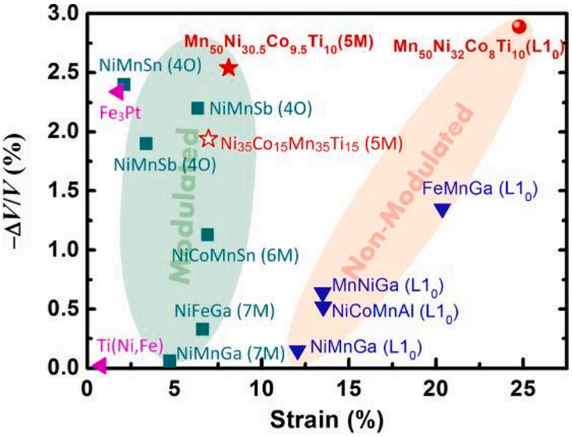

Fig. 50. Volume change versus strain in martensitic phase transformation for some Heusler and other ferromagnetic shape memory alloys. All-*d*-metals ferromagnetic shape memory alloys (FSMAs) are represented by a filled star, red hollow star, and red circle. (From Wei et al. [192]). (For interpretation of the references to color in this figure legend, the reader is referred to the web version of this article.)

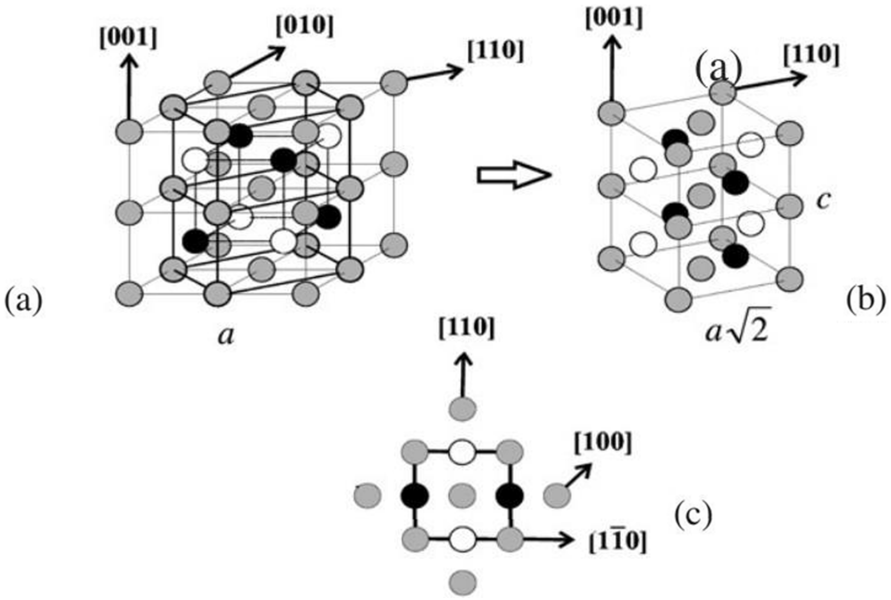

Fig. 51. Martensitic transformation in Ni_2Mn Ga Heusler alloy: grey atoms: Ni; white atoms: Mn; black atoms: Ga. The structure changes from the cubic $L2_1$ to the tetragonal $L1_0$. (From Planes et al. [205]).

significant increase in magnetic energy. Provided that the energy to move twin boundaries is low enough, there will be a rotation of the structural domains in such a way that their easy axis becomes aligned with the externally applied field.

Entel et al. [201] modeled the phase diagram of magnetic shape memory alloys of the Heusler type $Ni_{2+x}Mn_{1-x}Ga$ alloys by using the phenomenological Ginzburg–Landau theory. Ullako et al. [84] obtained a magnetic field-induced strain (MFIS) of 0.2 % in a single crystal of Ni_2MnGa; since then, much higher strains have been reported: Murray et al. [202] reported MFIS of 6 % in ferromagnetic martensitic $Ni_{49.8}Mn_{28.5}Ga_{21.7}$ alloy at room temperature. Sozinov et al. [203] declared that they acquired giant MFIS of 9.5 % in $Ni_{48.8}Mn_{29.7}Ga_{21.5}$ orthorhombic seven-layered martensitic phase in the field of<1 T at ambient temperature. The latter result is shown in Fig. 54. These magnetic shape memory alloys (MSMAs) lead to a number of important functional properties such as giant magnetoresistance, shape recovery, metamagnetic properties, and large magnetocaloric effect. These are presented in subsequent sections.

Some materials undergo significant strains (up to 10 %) in response to externally applied magnetic fields. This effect can be used in many applications, such as sensors, actuators, transducers, micromechanical systems, and even magnetic refrigerators.

As mentioned earlier, some Heusler alloys undergo martensitic transformations, and these are altered by external fields. Ullakko et al. [84] discovered this effect in the full Heusler alloy Ni_2MnGa. It should be mentioned that most Heusler alloys do not exhibit

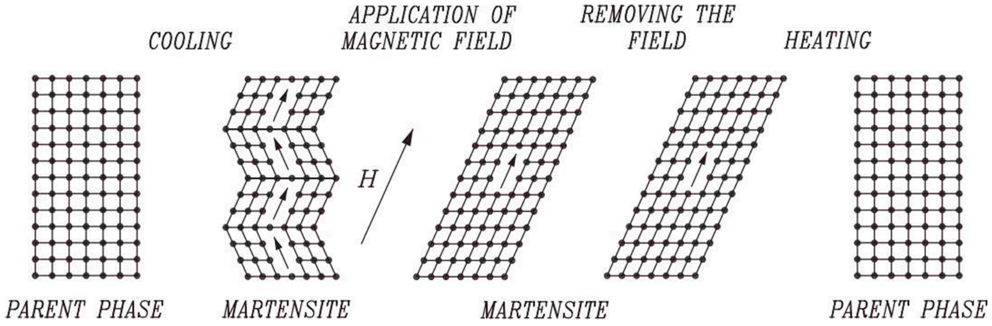

Fig. 52. Magnetic shape memory effect. Cooling below M_s generates the martensite structure, and the variants, under the effect of the magnetic field, align with the magnetic field, with associated strains. Upon removal of the field, the one-structure remains. Upon heating, the austenitic structure is recovered. (From Planes et al. [205]).

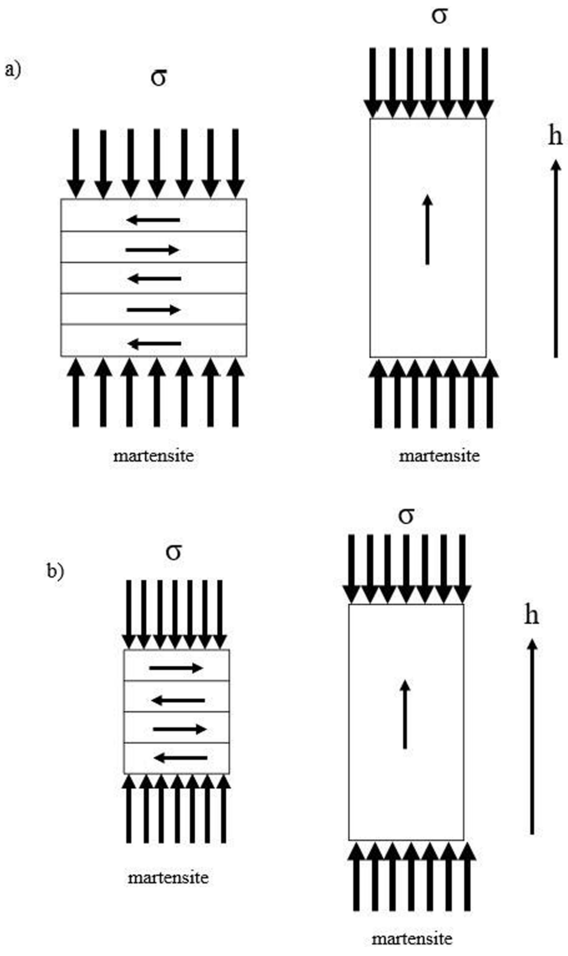

Fig. 53. Strain induced by the application of a magnetic field h on the (a) Martensitic and (b) Austenitic structures. (a) The martensite variants are altered creating the magnetic superelastic effect. The application of a field shifts the transition to a higher temperature, thus inducing the forward martensitic transition. (b) The application of a field shifts the transition to a lower temperature, thus inducing the reverse martensitic transition in (b) the austenite transforms to martensite. (From James and Wuttig [198]).

martensitic transformations. After this discovery, a significant number of Heusler alloys were found to have this effect. The following alloys undergo these effects:

- Ni-Mn-Ga

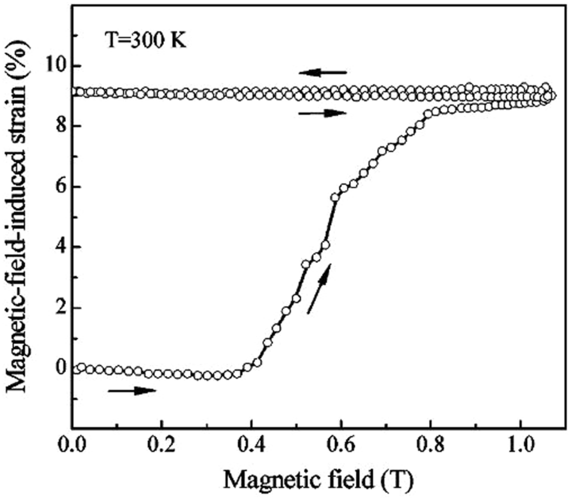

Fig. 54. Magnetic field induced strain for a $Ni_{48.8}Mn_{29.7}Ga_{21.5}$ alloy at 300 K measured perpendicular to magnetic field applied along [100] direction reaching 9.5 %. (From Sozinov et al. [203]).

- Ni MnX (X = Al, In, Sn, or Sb)
- Ni Co MnX (X = In, Sn, Sb, or Al)

Ni-Mn-Al also undergoes a martensitic transition, even though it does not exhibit a large magnetization change like the others, because the magnetic state changes from antiferromagnetic to paramagnetic. Thus, they are limited in their use for magnetic refrigerators or magnetic shape memory materials; nevertheless, the martensitic transition is there.

This magnetic shape memory effect manifests itself through two microstructural processes:

- Twin boundary motion (inside the martensite).
- Martensitic transformation.

The typical martensitic structure for such alloys is shown in Fig. 55. The martensite is twinned rather than dislocated and this is the typical microstructure of martensite in the metallic alloys undergoing the shape memory and super-elastic effects. Fig. 56 shows the effect of external magnetic fields on M_s and A_s in a $Ni_{45}Co_5Mn_{36.6}In_{13.4}$ alloy. A field of 70 kOe reduces M_s by 30 K. The Clausius-Clapeyron equation can be modified for the magnetic field and has this form [119].

$$\frac{dB}{dT} = \frac{\Delta S}{\Delta M} or \Delta T_t \approx \left(\frac{\Delta M}{\Delta S}\right)\Delta B \tag{9}$$

where B is the applied magnetic field, ΔT_t is the change in transition temperature, ΔS is the entropy difference between the two phases, and ΔM is the difference in magnetization between the two phases (austenite and martensite).

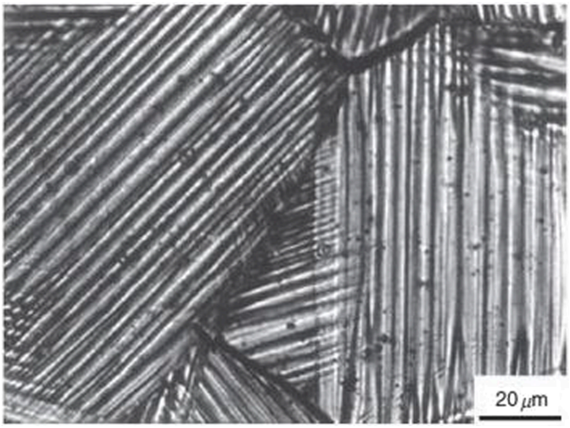

Fig. 55. Martensite in a $Ni_{54}Mn_{25}Ga_{21}$ alloy (close to the composition of Heusler alloy Ni_2MnGa where this effect was first discovered). (From Ma et al. [323]).

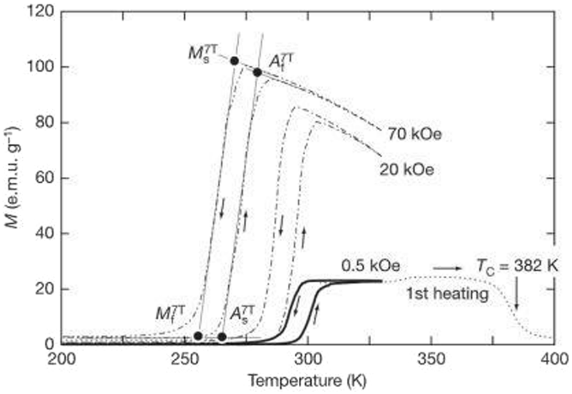

Fig. 56. Cooling and heating curves for $Ni_{45}Co_5Mn_{36.6}In_{13.4}$; notice downward shift with the increasing external applied field. The high-temperature phase is ferromagnetic. (From Kainuma et al. [324]).

A better representation of the Clausius-Clapeyron equation (Eq. (9)) is:

$$\Delta S = \frac{\Delta M}{\Delta T_t/\Delta B} \tag{9a}$$

The change in entropy increases with ΔM and is also influenced by the shift in ΔB and the transition temperature. For the alloy shown in Fig. 56, the austenite (high temperature) phase is ferromagnetic, and the martensite is nonmagnetic (either antiferromagnetic or paramagnetic). Thus, the magnetization difference (ΔM) between them is very large. The martensitic transformation for this alloy has a strain of 3 %, at 70 kOe. The stress of 108 MPa was obtained through the transformation, which is very significant.

In other alloys, the magnetic field produces the motion of internal twin boundaries. This is best explained by an illustration in Fig. 57. The external magnetic field causes the twin variant aligned with it to grow at the expense of the other ones, resulting in an increase in the length of the specimen.

On the other hand, an applied stress causes the opposite motion of the boundaries. The latter is the classic shape memory effect which can also cause superelasticity. This is leading to the design of new Heusler alloys using density functional and Monte Carlo simulations. The phase diagrams of magnetic shape-memory Heusler alloys, in particular, ternary Ni-Mn-Z and Quaternary (Pt, Ni)-Mn-Z alloys with Z (¼Ga, Sn) can be constructed, and important parameters unraveled, as explained by Siewert et al. [204].

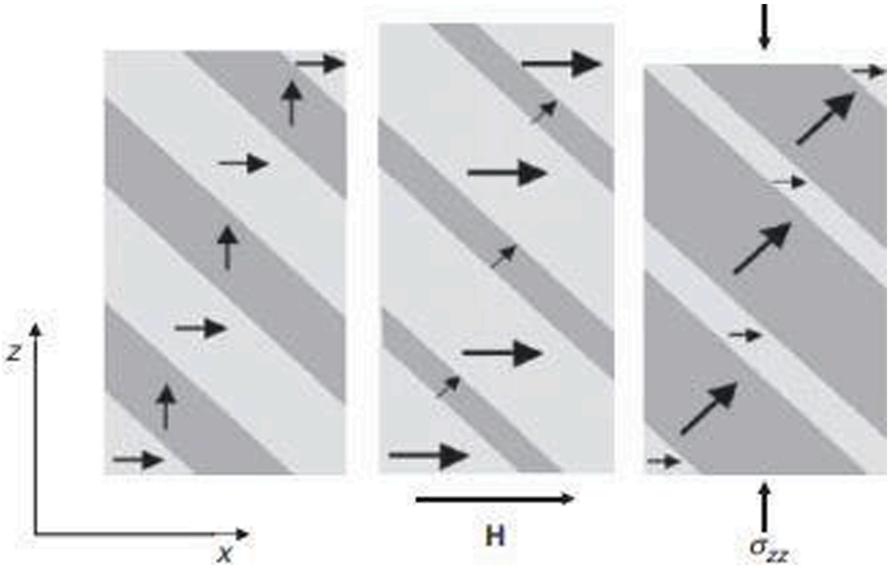

Fig. 57. Movement of two twin variants in martensite in response to horizontal external magnetic field H and vertically applied stress σ_{zz}, producing opposite strains; expansion of light gray variant increases the length of the specimen and dark grey variant reduces it. (From Acet et al. [325]).

9. Caloric properties in Heusler alloys

The caloric effect is described as an adiabatic temperature change (ΔT_{ad}) or an isothermal entropy change (ΔS_{iso}) resulting from external stimulus application in a solid material [205]. These stimuli may be carried out by a magnetic field (H), hydrostatic pressure (P), mechanical stress (σ), or an electric potential (E), producing magnetocaloric, mechanocaloric (barocaloric and elastocaloric), or electrocaloric effects, respectively. The magnetocaloric effect (MCE) is the most studied among all caloric effects. Recently, a combination of these stimuli (magnetic field and stress), called multicaloric effects has been explored [206–208].

9.1. Magnetocaloric effect

The magnetocaloric effect was theoretically predicted by William Thomson in 1878 [209]. Through thermodynamic studies, Thomson explained the cooling and heating of iron due to the presence of a magnetic field. In 1881, Warburg [210] experimentally reported the magnetocaloric effect in iron. In 1917, Weiss and Piccard [211] were the first to measure a temperature change of 0.7 K in Ni under a magnetic field of 1.5 T. In 1933, Giauque and MacDougall [212] were the pioneers to reach sub-Kelvin temperature (0.25 K) under adiabatic magnetization by using a paramagnetic salt ($Gd_2(SO_4)_3.8H_20$)). Due to this investigation, in 1949, Giauque received the Nobel Prize in chemistry. In 1976, Brown [213] built a magnetic refrigerator using gadolinium plates. From this experiment, Brown reached the temperature of 47 K after 50 cycles without a heat load. In 1997, Pecharsky and Gschneider [214] discovered a compound ($Gd_5(Si_2Ge_2)$) that exhibits a giant magnetocaloric effect. This effect had been known before but was much smaller. If such a material is subjected to a magnetic field adiabatically, there is a decrease in temperature which can be used in a thermodynamic cycle such as Carnot or Rankine. This is better understood by analyzing the second law of thermodynamics (More details in Franco et al. [215]):

$$dU = \partial Q - \partial W \tag{10}$$

where U is the internal energy, Q is the heat, and W is the work., respectively. The work W can be considered as composed of two components: mechanical (PdV) and magnetic ($\mu_0 HdM$):

$$\partial W = PdV - \mu_0 HdM \tag{11}$$

where H is the applied magnetic field, μ_0 is the magnetic permeability, and M is the magnetic moment.

The adiabatic temperature change upon the application of a magnetic field H is expressed as:

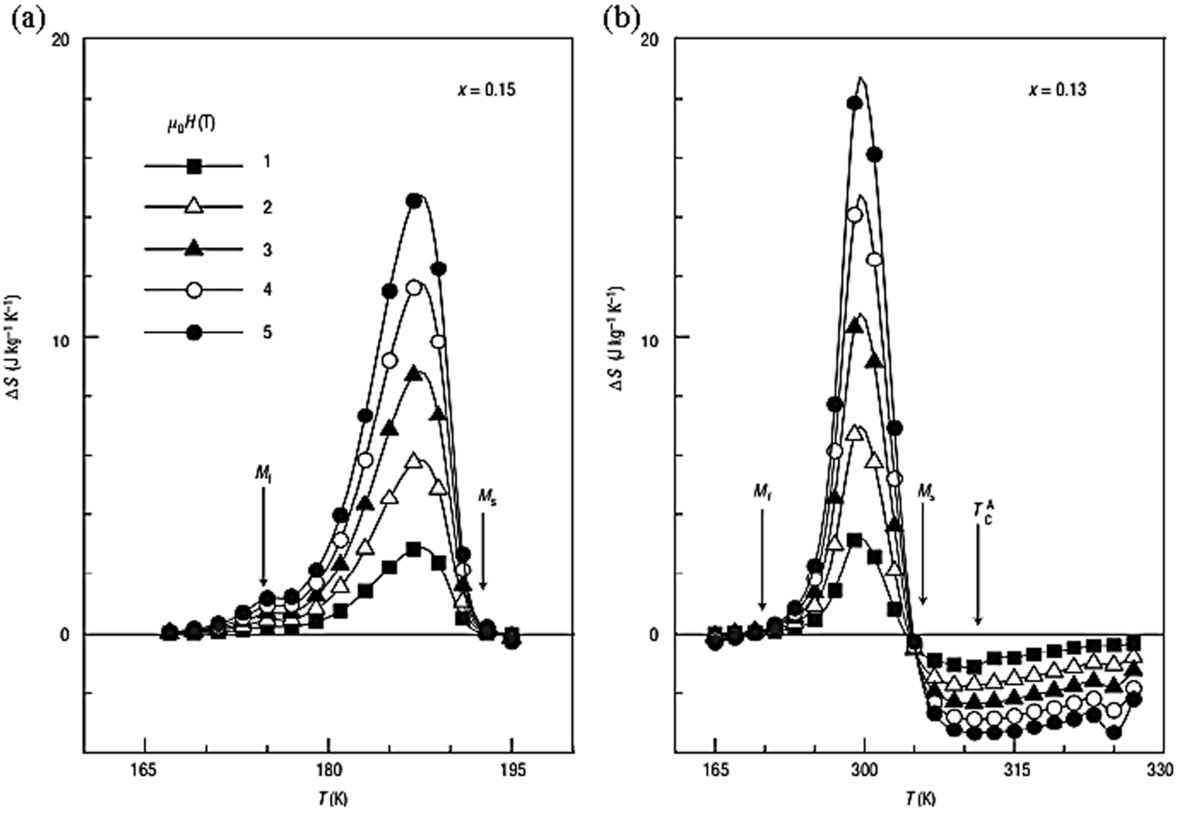

Fig. 58. Entropy change (ΔS.) (a) For × = 0.15 and (b) For × = 0.13. The ΔS is positive for two compositions for the temperature between $M_f < M_s$ (From Krenke et al. [92]).

$$\Delta T_{ad} = -\mu_0 \int_{H_i}^{H_f} \frac{T}{C_{P,H}} \left(\frac{\partial M}{\partial T}\right)_{P,H} dH \tag{12}$$

where H_i and H_f are the initial and final magnetic fields, respectively. The magnitude of the magnetocaloric effect is often expressed by the entropy change as proposed by Tishin et al. [216].

$$S(T,H) = \mu_o \int_{H_i}^{H_f} \left(\frac{\partial \mathrm{M}}{\partial T}\right)_H dH \tag{13}$$

where the ΔS sign is governed by the $\partial M/\partial T$ sign.

The following, materials have been found to exhibit this effect: Laves phases [217], Gd [217], $Gd_5(Ge,Si)_4$, and the related $Gd_5(Si_xGe_{4\text{-}x})$ alloys [214,218], $La_{0.8}Ca_{0.2}MnO_3$ [219], $La(Fe,Si)_{13}$, $AlFe_2B_2$ [217], $Tb_5Si_2Ge_2$ [220], MnAs and $MnAs_{1\text{-}x}Sb_x$ compounds [221], $MnFeP_{0.45}As_{0.55}$ and related $MnFeO_xAs_{1\text{-}x}$ alloys [222], FeRh [223], Fe_2P-based alloys [224]. Heusler alloys based on Ni-Mn-X (X = Ga, In, Sn, Sb) also are materials that exhibit a magnetocaloric effect. Furthermore, multifunctional properties, for instance, the magnetic shape memory effect [205], magnetoresistance [205,225], magnetic superelasticity [93], elastocaloric [102,103] and barocaloric [100] effects are present in many Heusler alloys. In particular, Ni-Mn-Ga single crystals have been extensively studied due to the highest magnetocaloric effect value ($\Delta S = -86$ J kg^{-1} K^{-1} at 50 KOe field) reported by Pasquale et al. [226]. In Heusler alloys, the magnetocaloric effect is associated with the reversible martensitic transformation induced by a magnetic field (magnetic shape memory). Since magnetic refrigeration requires the magnetocaloric effect to operate close to room temperature, the Heusler alloys amenable to this effect should have a M_s close to it.

It should be mentioned that some Heusler alloys also can exhibit the inverse magnetocaloric effect. This is the most common case. For this situation, the increase of a magnetic field leads to a decrease in the temperature. The inverse magnetocaloric effect was first observed in $Ni_{0.50}Mn_{0.50\text{-}x}Sn_x$ alloys, by Krenke et al. [92]. It was observed that the structural and magnetic phase transformation occurs in the range of composition between $0.13 \leq x \leq 0.15$. Krenke et al. [92] also evaluated the field-induced entropy change (ΔS) around the martensitic transformation at different compositions through Equation 11. For both compositions (x = 0.15 and × = 0.13), the entropy change is positive between $M_f \leq T \leq M_s$. Therefore, for the highest magnetic field (5 T), the entropy variation in function of temperature was 15 J K^{-1} kg^{-1} for × = 0.15 (Fig. 58a), and 18 J K^{-1} kg^{-1} for × = 0.13 (Fig. 58b). A particular behavior is observed in Fig. Xb, the entropy change values are negative when the temperature (T) is higher than the austenite phase Curie temperature (T_C^A) since $\partial M/\partial T < 0$, in this case. Krenke et al. [92] explain that the lower values of entropy change in this temperature range are due to the second-ordered magnetic transition and the magnetization (M) changes over a wider temperature limit than for the first-order martensitic transformation.

The inverse magnetocaloric effect is also present in other Heusler alloys: Ni-Mn-In [93] and Ni-Mn-Sb [94,96]. Bourgault et al. [97] reported a large inverse magnetocaloric in Quaternary Heusler alloy, $Ni_{45}Co_5Mn_{37.5}In_{12.5}$. They obtained an entropic temperature change of 30 J kg^{-1} k^{-1} applying a magnetic field of 5 T at 355 K. Liu et al. [98] demonstrated a giant magnetocaloric effect in the $Ni_{45.2}Mn_{36.7}In_{13}Co_{5.1}$ alloy. The adiabatic temperature change (ΔT_{ad}) was − 6.2 K in a moderate magnetic field (1.9 T). Fig. 59 presents the adiabatic temperature change at 2 T for various magnetic refrigerants. Ni-Mn-In-Co alloy is indicated by a solid pink circle, and its ΔT_{ad} value is exceptionally high compared to the other Heusler alloys in the plot. Liu et al. [98] explain that this result is mainly due to the structural transition contribution, which promotes a very large cooling effect. Fig. 60 illustrates the contribution of the

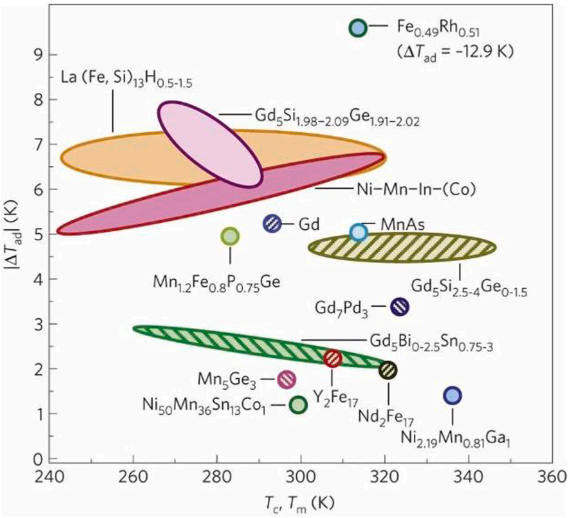

Fig. 59. Adiabatic temperature change at 2 T for many of the most studied ambient temperature magnetic refrigerants. Compounds under second-order transition (magnetic transition temperature T_c) are indicated by hatched patterns, whereas compounds under first-order transition (magnetostructural transition temperature T_m) are identified by solid fill patterns). (From Liu et al. [98]).

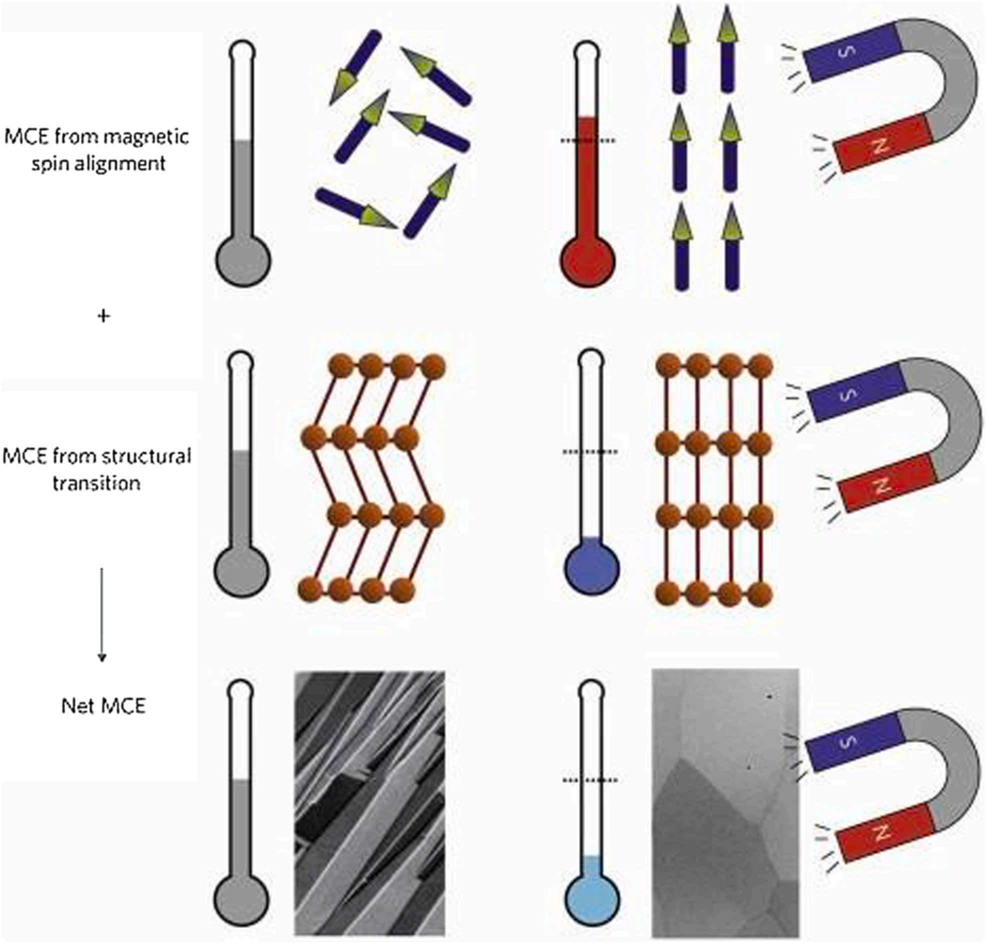

Fig. 60. Magnetic and structural contributions for a first-order magnetic transition to the Magneto Caloric Effect (MCE) using the Ni-Mn-based Heusler alloys as an example. (From Liu et al. [98]).

magnetic and structural components of the first-order magnetic transition to the magnetocaloric effect in Ni-Mn-based Heusler compounds. As observed from the schematic drawing, in the first contribution, the alignment of the magnetic moment via adiabatic magnetization, promotes the heating of the material (top). At the same time, the structural transition (second contribution) from the low-magnetization and twinned martensite phase to the high-magnetization and symmetric austenitic phase results in a very large

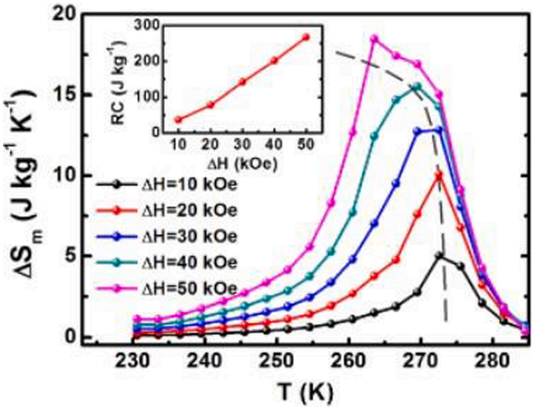

Fig. 61. Magnetic-entropy changes as a function of temperature under different magnetic fields. The refrigerator capacity (RC) is shown in the insert. (From Wei et al. [188]).

cooling effect (middle). The sum of these opposite contributions leads to a net cooling of the material (bottom). The highest value in adiabatic temperature change for Heusler alloys was obtained by Gottschall's group [99]. It reached a ΔT_{ad} equal to − 8 K at 1.95 T for $Ni_{45.7}Mn_{36.6}In_{13.5}Co_{4.2}$ Quaternary Heusler alloy through the first-order magnetostructural transition. However, because of the huge thermal hysteresis (10 K) of this alloy, the high adiabatic temperature change was not achieved in a cycling manner. In spite of this, Gottschall et al. [99] were able to achieve a reversible magnetocaloric effect of − 3 K, a surprisingly high value that competes with the ΔT_{ad} of ~ 3.2 K for $LaFe_{13}Si_{13}Co_{13}$ obtained by Liu et al. [227].

All-*d*-metal Heusler alloys, formed by only transition metals, also exhibit the magnetocaloric effect. Wei et al. [188] added Ti and Co to Ni-Mn-based Heusler alloys. A certain amount of Ti stabilizes the austenitic phase and decreases the temperature, while strong ferromagnetism is achieved due to the Co atoms. Through the arc melting process, followed by annealing and quenching, the samples were produced. Fig. 61 shows the values of the magnetic-entropy changes (ΔS_m) for different applied magnetic fields and the refrigerant capacity (CR) to $Ni_{35}Co_{15}Mn_{35}Ti_{15}$ alloy. The highest value achieved was 18 J $kg^{-1}K^{-1}$ in a field of 50 kOe at 263 K. The refrigerant capacity (CR) obtained for this alloy under a magnetic field of 50 kOe is 267 J kg^{-1}. This result indicates that all-*d*-metal Heusler alloys are strong magnetocaloric candidates. Therefore, the magnetoresistance effect of this alloy close to room temperature was investigated. For an applied field of 70 kOe, the MR is equal to 37 %, while in a higher magnetic field, 120 kOe, the MR is 46 %. Recently, Gottschall's group [195] also investigated the magnetocaloric effect in Ni-Co-Mn-Ti (all-*d*-metal) Heusler alloys. The samples were prepared by arc melting under a controlled atmosphere. The composition of Co and Ti was varied due to the stability of the austenitic phase promoted by Co, and an increase in the austenitic Curie temperature (T_C^A) favored by Ti. Among the different compositions, the highest isothermal temperature change (ΔS_{iso}) value of 38 J kg^{-1} K^{-1} was obtained for the $Ni_{37}Co_{13}Mn_{34}Ti_{16}$ alloy, in a magnetic field of 2 T at 250 K (Fig. 62a). Besides, for the first field application, the maximum ΔT_{ad}, equal to − 3.5 K was also obviously achieved in the $Ni_{37}Co_{13}Mn_{34}Ti_{16}$ compound. For the reversibly field cyclic effect, the ΔT_{ad} was − 0.5 K (Fig. 62b). Gottschall et al. [195] demonstrated that this alloy has a very sharp phase transition, and the magnetic field used was not sufficient to promote a fully induced phase transition. This behavior is due to the low displacement of the transition temperature at the applied magnetic fields. The addition of Co improves the magnetocaloric effect for this alloy and resolves this issue.

9.2. Mechanocaloric effect

The mechanocaloric effect can be described as the thermal response (isothermal temperature change and adiabatic temperature change) of a material due to the application of an external mechanical stimulus [228]. If the stimulus is promoted by pressure, the barocaloric effect occurs. On the other hand, if the external stimulus is produced by uniaxial stress, the elastocaloric effect emerges [229].

The barocaloric effect (BC) controlled by hydrostatic pressure (P) is expressed as:

$$\Delta S = -\int_0^P \left(\frac{\partial V}{\partial T}\right)_{P'} dP' \qquad (14)$$

where V is the volume of the system.

This mechanism occurs in materials that undergo a first-order transformation with an appreciable volume change [230]. There are few investigations on the barocaloric effect for Heusler alloys because many of them do not exhibit large volume change at the martensitic transition. In addition, due to the small volume change, the measurement of the entropy is imprecise [100,231]. Mañosa's group [232] demonstrated that hydrostatic pressure has a strong influence on the martensitic transition, implying that Ni-Mn-In alloy could be a promising material for exhibiting a large barocaloric effect. Later on, Mañosa et al. [100] studied the barocaloric effect in magnetic shape memory Ni-Mn-In Heusler alloys. They obtained an entropy change equal to 24.4 J Kg^{-1} K^{-1} at 260 MPa, a value 20 times higher than the elastic heating effect ($\simeq \beta V \Delta P = 1.2$ J kg^{-1} K^{-1}). Mimosa et al. [100] explain that this alloy displays a large barocaloric effect due to the volume and entropy discontinuities at a magnetostructural transition. Besides the barocaloric effect, this alloy also shows magnetocaloric properties, as mentioned in Sub-section 8.1.

Taulats et al. [233] evaluated the barocaloric and magnetocaloric effects for different compositions of Ni-Mn-In alloys. It was demonstrated that the absolute value of entropy change increases when both the hydrostatic pressure and the magnetic field increase. Fig. 63 shows the effect of pressure and magnetic field on the entropy change. Taulats et al. [233] noted that when the martensite transformation occurs above the austenite Curie temperature, the samples exhibited a larger barocaloric effect. Concerning the magnetocaloric effect, when the martensite and magnetic transition are close, the entropy change reaches the maximum value. The barocaloric effect is found in all-*d*-metal Heusler alloys. Aznar et al. [234] studied this property for the $Ni_{50}Mn_{31.5}Ti_{18.5}$ alloys, with a small amount of B (0.2 at.%). An isothermal entropy change equal to 74 J kg^{-1} K^{-1} at an applied pressure of 400 MPa was found. Therefore, the refrigerant capacity for this alloy corresponds to 1100 J kg^{-1}. These results are superior to the other shape memory Heusler alloy previously investigated. Table 6 compares the results of some shape memory Heusler alloys with the $Ni_{50}Mn_{31.5}Ti_{18.5}$ all-*d*-metal Heusler alloy. Aznar et al. [228] demonstrate the feasibility of these alloys to be applied in solid-state refrigeration. The giant barocaloric effect is also present in other materials, such as ferroelectric [235,236] and ferrielectric [237], hybrid perovskite [238], fluorides [239,240], elastomeric polymers [241,242], and natural rubber [243,244].

The elastocaloric effect (eC) arises from the combination between the lattice and the external applied stress. This property can be expressed in terms of entropy change, ΔS, (under isothermal conditions) or temperature change, ΔT (under adiabatic conditions):

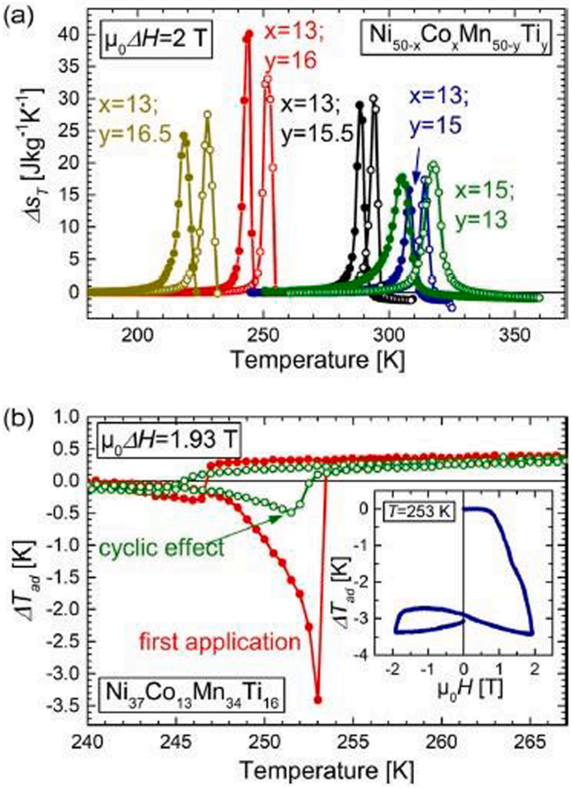

Fig. 62. (a). Isothermal temperature change (ΔS_T) curves for different compositions of $Ni_{50\text{-}x}Co_xMn_{50\text{-}y}Ti_y$ samples under magnetic field change of 2 T. Heating is designated by open symbols, while cooling is characterized by full circles. (b) Adiabatic temperature change measurement for $Ni_{37}Co_{13}Mn_{34}Ti_{16}$. The first field application is represented by the red line. The reversible effect due to the second magnetic field cycle is marked by the green row of open circles. The inset (blue line) refers to the magnetic field dependency on adiabatic entropy change starting at 253 K for the first two magnetic fields. (From Taubel et al. [195]). (For interpretation of the references to color in this figure legend, the reader is referred to the web version of this article.)

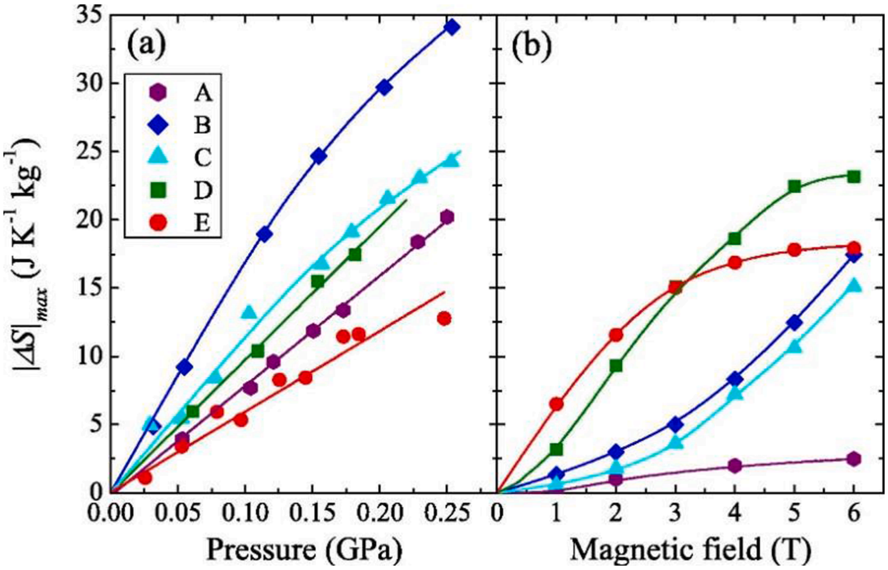

Fig. 63. (a). Effect of hydrostatic pressure on isothermal entropy change (barocaloric effect). (b) Effect of magnetic field on the isothermal entropy change (magnetocaloric effect). A ($Ni_{2.02}Mn_{1.36}In_{0.62}$); B ($Ni_{2.05}Mn_{1.30}In_{0.65}$); C ($Ni_{1.99}Mn_{1.37}In_{0.64}$); D ($Ni_{1.99}Mn_{1.34}In_{0.67}$); E ($Ni_{2.00}Mn_{1.32}In_{0.68}$). (From Taulats et al. [233]).

Table 6

Comparison of properties of various Heusler alloys with ferromagnetic shape memory Heusler alloys with $Ni_{50}Mn_{31.5}Ti_{18.5}$ [234].

Samples	$\lvert\Delta S_t\rvert$(J Kg^{-1} K^{-1})	dT/dp (K kbar^{-1})	Δp (kbar)	$\lvert\Delta S\rvert_{iso}$ (J Kg^{-1} K^{1})	$\lvert\Delta T\rvert_{ad}$ (K)	RC (J Kg^{-1})	Ref
$Ni_{49.26}Mn_{36.08}In_{14.66}$	27	1.8	2.6	24.4	–	–	[100]
$Ni_{51.2}Mn_{32.5}In_{16.3}$	40.8	1.65	2.5	32	4	200	[233]
$Ni_{42.47}Co_{8.87}Mn_{31.67}Ga_{14.98}In_{2.01}$	22.8	3.2	2.5	16	–	200	[329]
$Ni_{58.3}Mn_{17.1}Ga_{24.6}$	16	0.4	10	13.5	2.8	56	[330]
$Ni_{44.6}Co_{5.5}Mn_{35.5}In_{14.4}$	16	4.4	6	15.6	6	399	[331]
$Ni_{42.3}Co_{7.9}Mn_{38.8}Sn_{11.0}$	28	4.7	6	23	10	786	[332]
$(Ni_{50}Mn_{31.5}Ti_{18.5})_{99.8}B_{0.2}$	85	3.3	4	74	12	1001	[234]

$$\Delta S = V_0 \int_0^{\sigma} \left(\frac{\partial \varepsilon}{\partial T}\right)_{\sigma'} d\sigma' \tag{15}$$

where V_0 refers to the equilibrium system volume, while ε and σ' represent the strain (elongation) and stress in the system, respectively.

$$\Delta T = -V_0 \int_0^{\sigma} \frac{T}{C} \left(\frac{\partial \varepsilon}{\partial T}\right)_{\sigma'} d\sigma' \tag{16}$$

where C is the heat capacity.

If the temperature change is insignificant and the heat capacity does not change significantly in a span of stress, the adiabatic temperature change is expressed by:

$$\Delta T_{ad} \approx -\frac{T}{C}\Delta S \tag{17}$$

The negative isothermal entropy above evolves to a positive adiabatic temperature change, which means a conventional elastocaloric effect, i.e, the applied stress leads to heating of the material ($\Delta T_{ad} > 0$), while it cools down when the stress is removed ($\Delta T_{ad} < 0$). Conversely, a positive isothermal entropy promotes a negative adiabatic temperature change, resulting in an inverse elastocaloric effect, i.e, the material cools under applied stress, and heats when the uniaxial stress is removed [245]. Fig. 64 illustrates the conventional and inverse elastocaloric effect.

The Clausius-Clapeyron equation can be used to evaluate the elastocaloric effects close to the first-order transitions.

$$\Delta S = -V_0 \Delta\varepsilon \frac{d\sigma}{dT} \tag{18}$$

where Δε refers to the change in length during the transformation along the applied stress direction.

Materials undergoing a stress-induced first-order transformation are expected to show a large elastocaloric effect [229]. Elastocaloric materials must exhibit two vital effects to reach a large and reproducible effect: (a) the transformation entropy change (ΔS_{tr}) needs to be large to offer enough potential for reaching a large elastocaloric effect; (b) good mechanical properties to endure the stress necessary to fully induce the martensite phase [103]. Volume change is an important feature of the first-order phase transition. Especially, for martensitic transformation, the larger the volume change ($\Delta V/V_0$) across the transformation, the stronger will be the

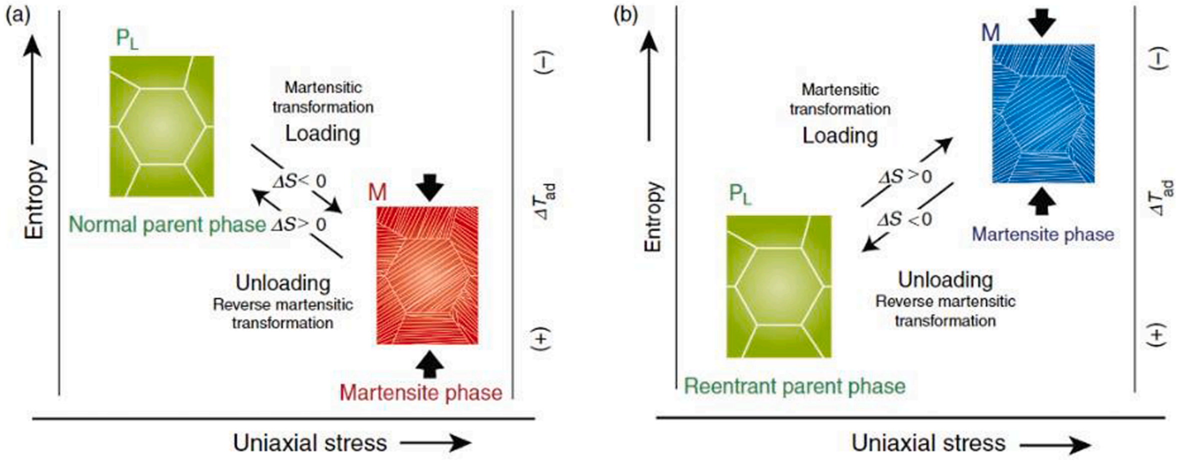

Fig. 64. Entropy and temperature change under uniaxial stress loading. (a) Conventional elastocaloric effect. (b) Inverse elastocaloric effect. (From Odaira et al. [245]).

first-order transition. Consequently, a larger ΔS_{tr} is reached [103,246]. Recently, the elastocaloric effect has gained attention because of the large latent heat and adiabatic temperature changes coupled with the martensitic phase transformation [247].

Large elastocaloric effects have been found in ferroelastic phase-transition materials, including Cu-based SMAs [229,248,249], Ni-Ti-based SMAs [247,250,251], and Ni-Mn-based Heusler compounds [252,253]. Among these alloys, the Ni-Ti system has been extensively studied due to the giant elastocaloric effect [247,254,255]. The Ni-Mn-based Heusler alloys have alluring multicaloric properties (such as magnetocaloric, barocaloric, and elastocaloric effects). However, they are brittle due to the weak grain-boundary cohesion, leading to poor cyclic stability for the elastocaloric effect. The addition of microalloying elements, such as boron, can solve this issue since it promotes the refinement of the grains, consequently, improving the mechanical properties [256]. Fig. 65 shows a schematic illustration of boron effect on the grain boundary.

The elastocaloric effect is present in all-*d*-metal Heusler alloys. Wei et al. [257] studied this effect in NiMnTi(Co) all-*d*-Heusler compounds. Two compositions were prepared, $Ni_{50}Mn_{32}Ti_{18}$ and $Ni_{35}Co_{15}Mn_{35}Ti_{15}$. For $Ni_{50}Mn_{32}Ti_{18}$, a large but irreversible adiabatic temperature change equal to 10.7 K was observed at a strain equal to 3.9 %. On the other hand, for $Ni_{35}Co_{15}Mn_{35}Ti_{15}$, a reversible elastocaloric effect with an adiabatic temperature change of 9.0 K was observed at a strain of 4.6 %. The reversibility of the elastocaloric effect obtained for the $Ni_{35}Co_{15}Mn_{35}Ti_{15}$ compound is attributed to the improvement of *d*-*d* hybridization initiated by the Co element. The elastocaloric effect in all-*d*-metal Heusler alloys is not only observed by Wei et al. [257]. There are many other examples in the literature as reported by Cong et al. [103], Yan et al. [122], and Shen et al. [258].

9.3. Multicaloric effect

It is known that the hysteresis coupled with the phase transition decreases the caloric efficiency and affects the reversibility of the caloric effect. These limitations can be overcome by combinations of external fields, such as magnetic and stress. This mechanism is called multicaloric effect [98,208,259]. Liu et al. [98] applied more than one external stimuli (magnetic field and hydrostatic pressure) to reduce the hysteresis of Ni-Mn-In-Co alloy. They observed that the hysteresis drastically reduced when the sample was magnetized in the absence of bias stress but demagnetized beneath a low external pressure (130 MPa); this behavior is illustrated in Fig. 66. The hysteresis is indicated by the grey area in the schematic drawing. Moreover, it was noted that the cooling power increased by simultaneously varying the magnetic field and pressure when compared to the cooling power reached by the variation of only the magnetic field. This agrees with the theoretical prediction by Oliveira [260].

Gràcia-Condal et al. [121] investigated the multicaloric effects in Ni-Mn-In alloys by combining the uniaxial stress and magnetic field. Fig. 67 shows the results of multicaloric properties (isothermal temperature changes) under the application of magnetic field and uniaxial stress. Fig. 68 shows the same effect for adiabatic entropy changes. A maximum value of entropy equal to 24 J kg^{-1} K^{-1} was obtained for the stress of 20 MPa and a magnetic field equal to 3.1 T at 297 K (Fig. 67d). Under a low magnetic field (1 T) and removal of the uniaxial stress (40 MPa), higher entropy changes ($\Delta S_{iso} = 10.5$ J kg^{-1} K^{-1} at 297 K and 13.9 J kg^{-1} K^{-1} at 298 K) were achieved in comparison with the single caloric effect (ΔS_{iso} = 4 J kg^{-1} K^{-1} and 6 J kg^{-1} K^{-1}). The same behavior was noted for the magnetocaloric effect. The maximum value of isothermal temperature change was − 5.9 K at 298 K (Fig. 68e), which was higher compared to the single caloric effect. From these results, can be implied that the combination of more than one stimulus improves the caloric properties.

Gottschall et al. [207] explored hysteresis to create an alternative multicaloric cooling cycle for materials that are subject to first-order phase transitions. Fig. 69(a) and (b) present the conventional active magnetic refrigeration (AMR) cycle and the new device produced by Gottschall's group, respectively. Fig. 69(c) shows how the hysteresis cycle occurs. As observed, this cycle is divided into six stages. In the first one, the material (Ni-Mn-In) is adiabatically magnetized followed by a decrease in the temperature because it

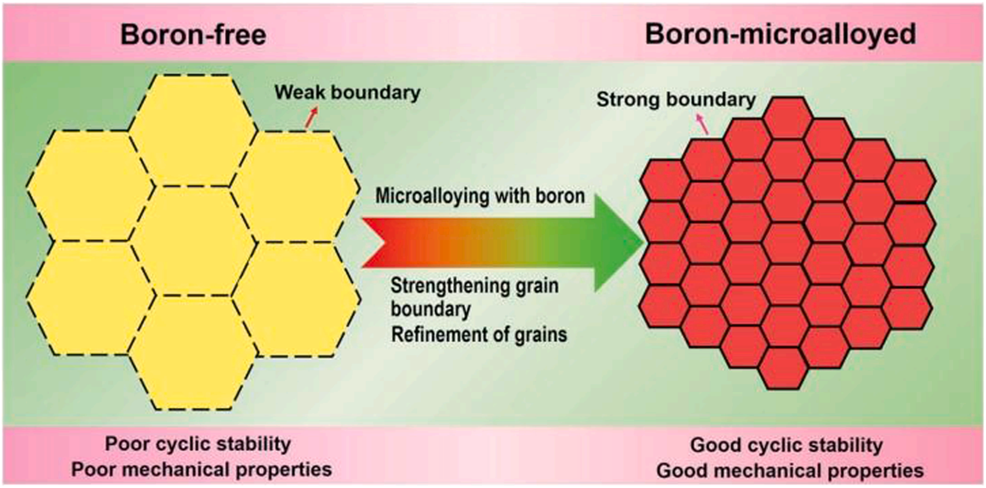

Fig. 65. Schematic illustration of boron effect on grain size. (From Yang et al. [273]).

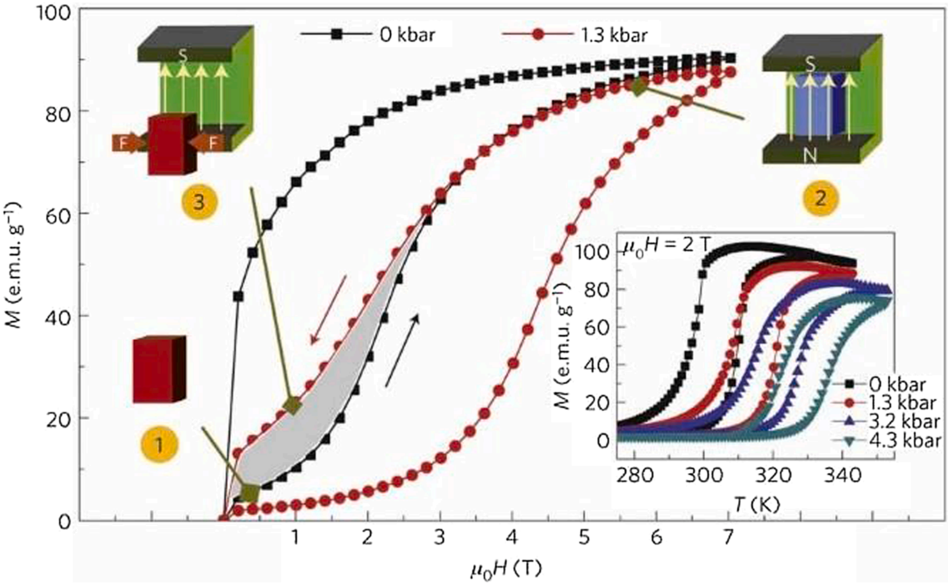

Fig. 66. Magnetization as a function of the magnetic field beneath 0 and 130 MPa (1.3 kbar) hydrostatic pressure at 308 K. The inset represents the shift of martensite transition temperatures due to the application of pressure up to 430 MPa (4.3 kbar). In a low field, the forward and reverse transitions can be generated (the shadowed area represents the hysteresis) as long as the sample is magnetized without pressure but demagnetized beneath an external pressure. (From Liu et al. [98]).

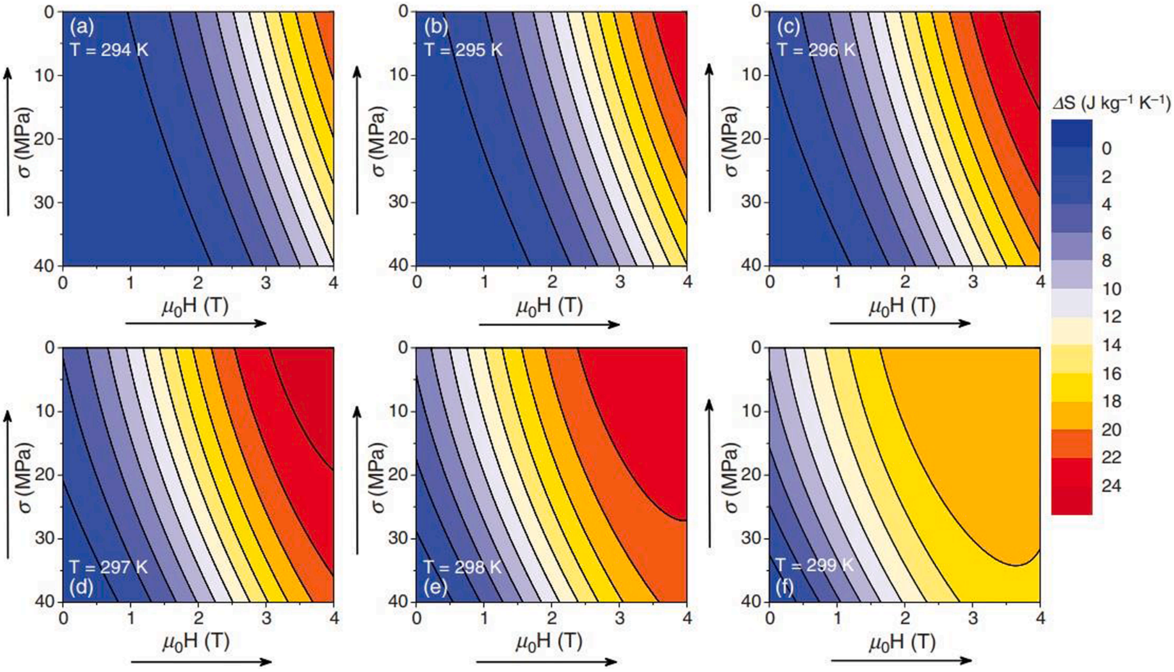

Fig. 67. Color maps for the multicaloric isothermal entropy change (ΔS_{iso}) due to the applied magnetic field and removal of the uniaxial stress. (From Gràcias-Condal et al. [121]).

exhibits an inverse MCE. In the second step, the thermal hysteresis is adjusted, therefore the reverse transition does not occur during the magnetization. As magnetostructural reversibility is absent in this system, it is possible to reduce the magnetized volume significantly. As a result, the large and costly rare-earth-element (REE) magnets needed to produce a magnetic field over a large volume are not required anymore. This is the major difference between the conventional AMR cycle and Gottschall's device. In the third step, after locking the alloy in a ferromagnetic phase, the heat is removed from the cooling compartment without a magnetic field. In order to

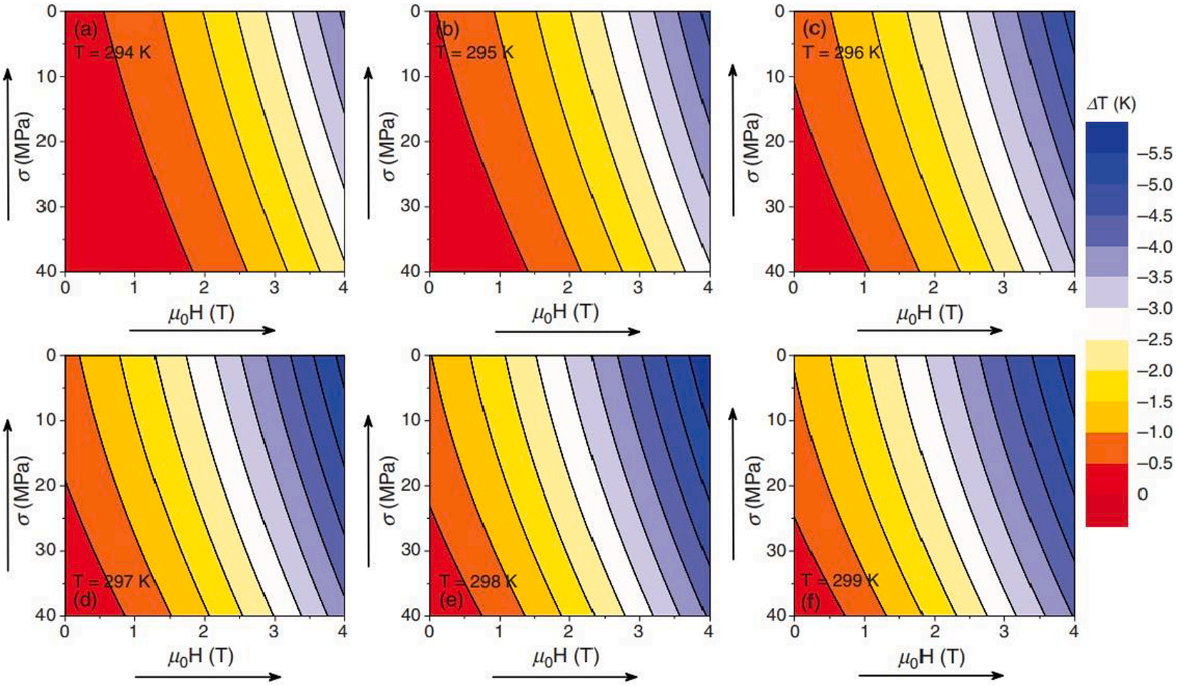

Fig. 68. Color maps for the multicaloric adiabatic temperature change (ΔT_{ad}) due to the applied magnetic field and removal of the uniaxial stress. (From Gràcias-Condal et al. [121]).

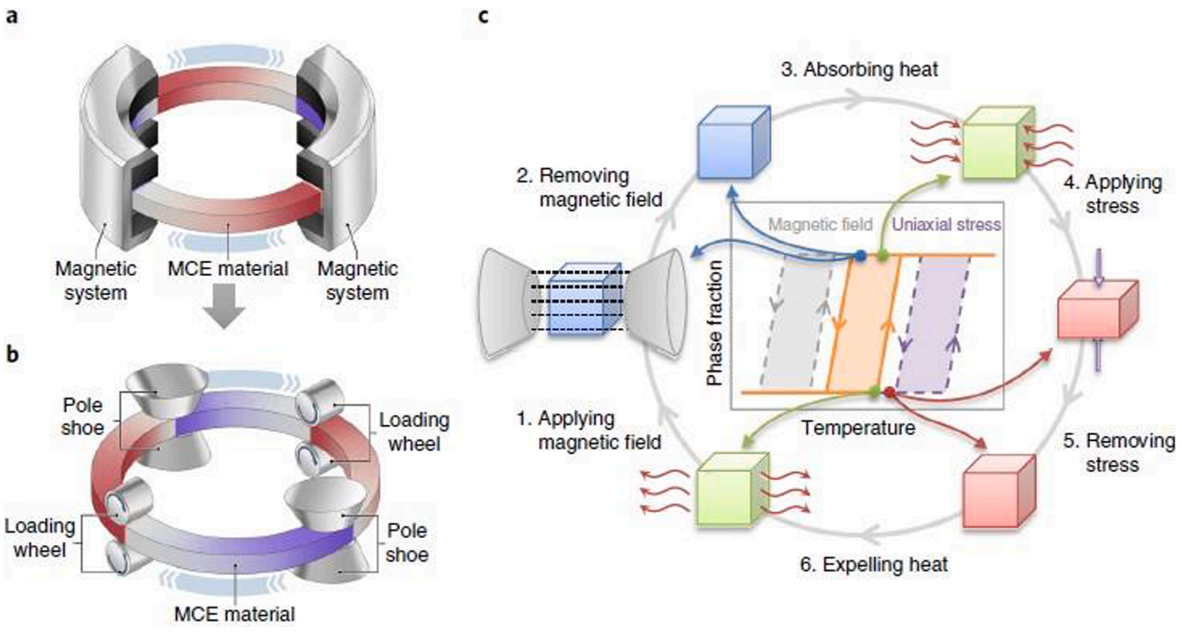

Fig. 69. Comparison between the thermal hysteresis cycle and the conventional magnetocaloric cooling cycle. (a) Conventional active magnetic refrigeration with large mass of permanent magnets. (b) New design of cooling cycle based on thermal hysteresis of magnetocaloric materials. (c) The six stages of the hysteresis cycle. The boxes represent multicaloric materials. The blue box indicates low temperature, the green box refers to the room temperature, and the red one indicates high temperature. The diagram shows the hysteresis of the multicaloric transition due to the phase fraction as a function of temperature in the absence of an external field (orange), in a magnetic field (grey), and under the effect of uniaxial stress (purple). (From Gottschall et al. [207]). (For interpretation of the references to color in this figure legend, the reader is referred to the web version of this article.)

return the alloy to its original form, a mechanical force (loading wheel) is required. Steps four and five are marked by a hefty heating effect because the reverse transformation is induced. In the last stage, the excess heat can be expelled to the outside. From this investigation, we can imply that Gottschall et al. [207] transformed hysteresis, which is a bottleneck, into an opportunity to improve the multicaloric effects.

10. Topological insulators in Heusler alloys

Solids materials are traditionally classified into three groups: metals, which can conduct electricity; insulators, which cannot conduct electricity; and semiconductors. It is possible to distinguish them from the valence and conduction bands. When the valence band is fully complete and separated from the conduction band through an energy gap, it can be an insulator or a semiconductor. For insulating materials, electrons are not able to be excited from the valence to the conduction band due to the large energy gap between them. On the other hand, in semiconductors, the energy gap between these two states is small; thus, some electrons located at the valence band can migrate to the conduction band. In the case of metals, there is an overlap between the valence and conduction bands, resulting in an undefined band gap. Due to this overlap, the electrons are able to conduct from 0 K until all finite temperatures [115].

Topological insulators belong to the new class of materials which cannot be classified purely as insulators, semiconductors, or metals because they have an insulator behavior in the bulk and metallic behavior at the surface [104,115,117,261,262]. Fig. 70 presents the electronic bands for solid state materials described above.

Topological insulators can arise in two and three-dimensional materials. The first observation of 2D topological insulators was in the binary semiconductor HgTe quantum wells (QWs). This quantum well is a thin layer of HgTe (topological) which is evolved by two insulating layers of CdTe (trivial semiconductors) [106,263,264]. CdTe exhibits a band ordering with s-orbital Γ_6 (conduction band) and p-orbital Γ_8 (conduction valence), which are separated by a substantial energy gap (~1.6 eV) [112]. As Hg is a heavy element compared to Te, a strong change in properties is expected due to the interaction between them. As a consequence, an inverted band ordering occurs for HgTe compounds, which means that the s band is shifted below the p band [110,112]. A 3D topological insulator was observed in a single crystal of Bi_2Se_3 in which the surface states form an odd number of Dirac cones [109,112,265–267]. Other single crystals such as Bi_2Te_3 and Sb_2Te_3 were identified as 3D topological insulators [265]. An odd number of band inversions (BIs) between the conduction and valence bands is the most important condition for a material to be a topological insulator. This band inversion originated from the relativistic effect, for example, the spin-orbital coupling (SOC), which is improved by using heavier elements instead of light elements [112]. Heusler alloys are versatile materials; due to their properties, there are wide possibilities to adjust the band gap and set up the desired band inversion by choosing appropriate classes with hybridization strength and the magnitude of spin-orbital coupling. Thus, these alloys can be topological insulators [111]. Among them, the important candidates for being tunable topological insulators are Half Heusler alloys [110,261,268].

Incidentally, Lui et al. [113] observed the topological surface in YPtBi and LuPtBi superconducting Half Heusler alloys. Felser's group [110,112], based on the first-principle calculations shows that approximately fifty Half Heusler alloys exhibit a band inversion similar to HgTe. These alloys can be adjusted from a trivial state to a topological insulator through two different strategies: (a) the first one is to vary the lattice constant by applying pressure or growing the alloy on a specific substrate; (b) the second way is to substitute the elements, which can be achieved by electronegative alteration or the strength of the spin-orbital coupling (SOC) (nuclear charge number, Z) [110]. Fig. 71 shows some Half Heusler alloy candidates to be topological insulators; for comparison HgTe and CdTe were inserted in the figure. Compounds located below zero energy, i.e, when the energy difference between ($\Gamma_6 - \Gamma_8$) the bands has a negative value, are topological insulators, following HgTe. By contrast, when the energy difference between the bands is positive, the compounds are trivial insulators, such as CdTe. Lin et al. [261] also investigated topological insulators in Heusler alloys. This behavior was found in several Half Heusler alloys such as LaPtBi, LuPtSb, LuPdBi, LuPtBi, YPdBi, YPtBi, and YAuPb, as predicted previously by Chadov et al. [110].

11. Mechanical properties

The mechanical properties of Heusler alloys have received much less attention than the electronic and magnetic properties because

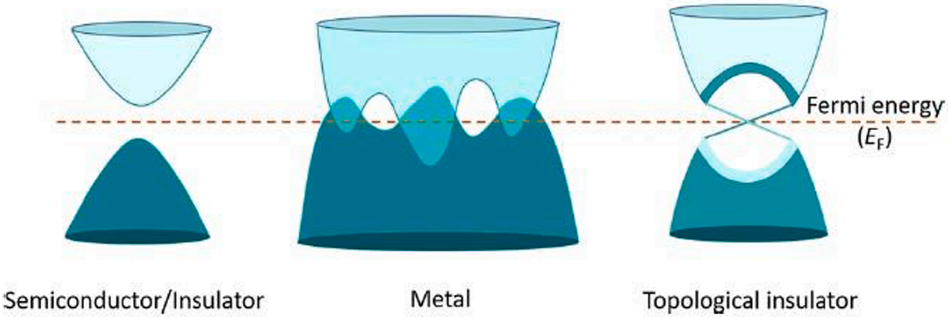

Fig. 70. Electronic bands in different solid-state materials. (From Kumar et al. [115]).

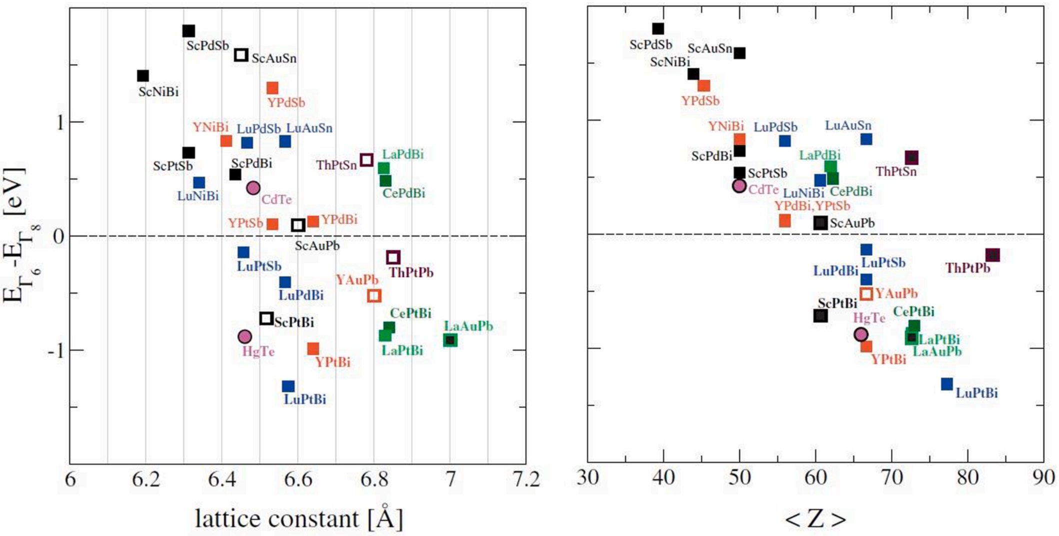

Fig. 71. Energy difference $\Gamma_6 - \Gamma_8$ bands calculated for several Half Heusler as function of lattice constant (left) and average nuclear charge Z (right). Each subgroup is represented by a specific color. The diverse shapes of markers refer to different component elements. Compounds with $\Gamma_6 - \Gamma_8 < 0$ are topological insulator candidates, while those with $\Gamma_6 - \Gamma_8 > 0$ are trivial insulators. (From Chadov et al. [110]).

the applications are classified into functional and structural: magnetocaloric, thermoelectrics, magnetic shape memory, and spintronics belong to the functional group. Experimental results are mostly limited to hardness (including nanoindentation) and elastic property measurements on half-Heusler alloys. Density Functional Theory (DFT) and Molecular Dynamics (MD) were also used to obtain a correlation between elastic modulus.

The results by Rogl et al. [118] presented in Fig. 72 are noteworthy. Clathrates (are compounds in which molecules of one component are physically trapped within the crystal structure of another) and Skutterudites (are cobalt arsenide mineral containing variable amounts of nickel and iron) are grouped with ceramics, and their covalent and ionic bonding establishes a linear relationship of hardness and Young's modulus with slope H^3/E^2, in the log–log plot. The half-Heusler alloys fall into this line, the hardness being superior, at a specific Young's modulus, to metals/steel. This is the direct result of their intermetallic character and superlattices, making the movement of dislocations more difficult by virtue of their larger Burgers vectors and high Peierls-Nabarro stresses. The limited experimental results were somewhat amplified by He et al [269] who performed nanoindentation experiments on additional Heusler alloys.

The use of Molecular Dynamics to estimate the hardness of Heusler alloys has been widely implemented and the results are shown in Fig. 73 represent the summary of many (~80) sources. The results of Rogl et al [118] and He et al [269] are shown in the same plot

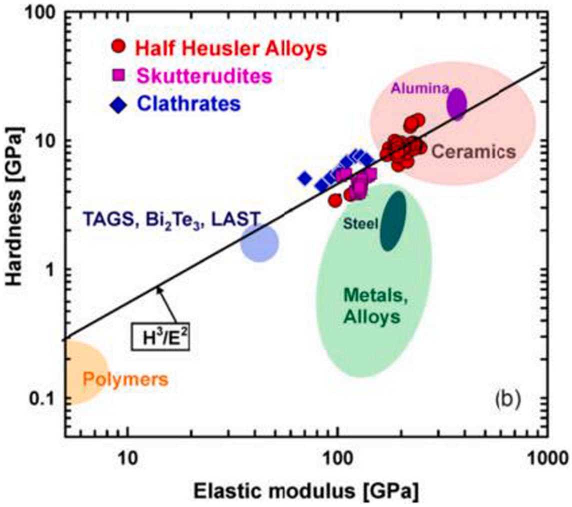

Fig. 72. Experimental results correlating elastic moduli and hardness for a range of materials; Half Heusler alloys fall into the ceramic range, rather than metals and alloys. (From Rogl et al. [118]).

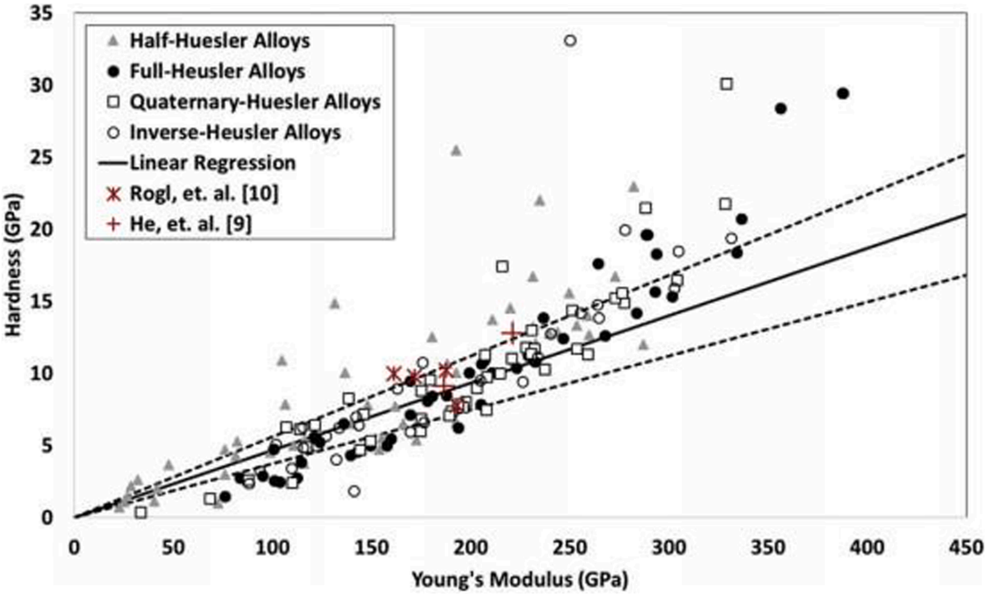

Fig. 73. The hardness of Heusler alloys as a function of Young's modulus. Experimental results by Rogl et al. [118] and He et al. [269] compared with MD simulation predictions. (From Everhart and Newkirk [119]).

and are consistent with calculations. Straight lines were used to correlate the hardness and elastic moduli. It is obvious that there is a correlation between hardness and young's modulus as the least square fit shows. However, the complexities of grain size, solid solution hardening, temperature, and other effects create effects that are beyond a simple correlation. However, within the realm of Heusler alloys with their characteristic ordered structure, superlattice, and order hardening, this correlation seems to hold, and the equation proposed by Yousef [270] applies:

$$H = \frac{(1-2\nu)E}{6(1+\nu)} \tag{19}$$

where E is Young's modulus, H is the hardness, and ν is Poisson's ratio.

For fracture toughness, the crack length at the edges of the indentations can be used to estimate the resistance of the material (see Fig. 74). If the ductility is high, such as copper, no crack is generated. On the other hand, if the toughness is limited, such as in intermetallics, a crack is generated whose length can be used to obtain a measure of toughness. The Evans-Charles equation has the form:

$$K_c = \beta\left(\frac{E}{HV}\right)^{1/2}\frac{F}{c^{3/2}} \tag{20}$$

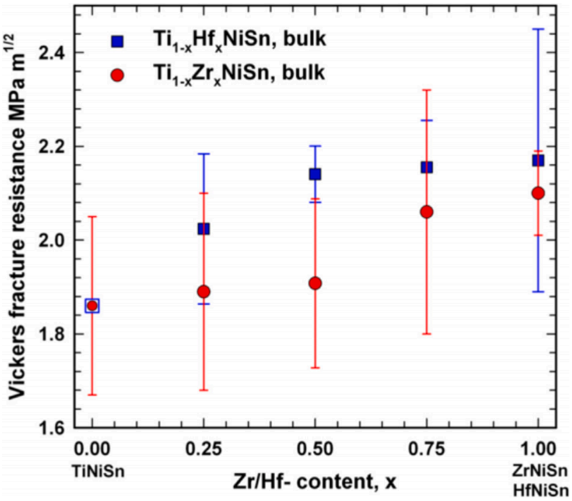

Fig. 74. Fracture toughness (from microhardness tests) for different Heusler alloys as a function of a varying Zr/Hf ratio (From Rogl et al.[118]).

where *HV* is the Vickers hardness, *F* is the indentation load, and *c* is the radial crack length from the center of the Vickers indentation. β is a function of the indenter angle; for Vickers indentation, it is equal to β = 0.016.

Microindentation was used to obtain approximate values of the fracture toughness, which is indeed very low, in the range of ceramics. This confirms the brittle nature of these Heusler alloys and is probably a characteristic of all. One of the authors (MAM) remembers preparing powders for X-ray diffraction and more rapid cooling by the use of a mortar and pestle, a technique that is appropriate for ceramics and minerals. The Cu-Mn-Sn alloy is comminuted into fine powder.

One of the few reports on mechanical testing is the compressive deformation of the Ni-Mn-In alloy which exhibits a martensitic transformation from $L2_1$ to B2. The compressive upsetting (6x6mm) of cylinders to a true strain of 1 was conducted at 773, 873, and 973 K (see Fig. 75(a) [271]; it shows significant ductility and dynamic recrystallization at the two higher temperatures, whereas at 773 KK microcracks were observed throughout the entire structure. Although M_s for this alloy is equal to 260 K, twins were formed and are seen in Fig. 75(b) after deformation at 973 K. This was attributed to an increase in M_s by plastic deformation. Interestingly, the other conditions did not exhibit it.

Elastic properties are more easily obtained than plastic and fracture responses. The latter requires experiments because of the complex interplay between dislocations, twins, and phase transitions with the existing structure. For the elastic response, first-principle calculations provide reliable results. Wen et al. [272]calculated the bulk, shear, and Young moduli for Ni_2XAl 1alloys (where X = Sc, Ti, or V). They also estimated the hardness using the Yousef empirical equation [139]. The values obtained are 9.48 GPa (for Ni_2ScAl), 8.09 GPa (for Ni_2TiAl), and 4.57 GPa (for Ni_2VAl). These are only first-order estimates. However, the anisotropy of elastic properties is obtained successfully. There are dramatic differences as shown in Fig. 76. The Young moduli are highest along with the [111] directions and lowest along [100]. Ni_2VAl shows the highest anisotropy.

11.1. Mechanical properties in mechanocaloric alloys

Solid-state refrigeration is a technique that presents great potential because the conventional processes involving vaporization are avoided. In particular, materials exhibiting the shape memory effect through martensitic transformations are amenable to be used in a solid-state refrigeration cycle. This effect can be used by means of magnetic, electrical, or mechanical input, respectively named magneto, electro, and mechanocaloric. The adiabatic temperature change associated with the martensitic transformation in NiTi is typically below 15 K. Some Heusler alloys also display this effect. The NiMnIn alloy exhibits a significant temperature change between 3 and 9.6 K (Huang et al. [120]). The compressive mechanical properties of a $Ni_{50}Mn_{31.7}In_{15.2}$ synthesized by three techniques (arc melting, suction casting, and directional solidification) are compared in Fig. 77 and the different stages of transformation and deformation are indicated. The samples fractured in a brittle manner at strains between 7 (suction casting) and 12 pct (directional solidification). The brittle fractures are shown in Fig. 77(b) to (d). This limited ductility is characteristic of Heusler alloys.

Yang et al. [273] studied the cyclability of elastocaloric effect in Ni-Mn-In Heusler alloys microalloyed with boron addition to improve the cyclic stability and the mechanical properties. By an arc-melting process under a high-purity argon atmosphere, a series of samples were produced with varying boron composition: $(Ni_{51.5}Mn_{33}In_{15.5})_{100\text{-}x}B_x$ (x = 0, 0.1, 0.2, 1.3, 0.4, 0.6; at.%). The best results of the elastocaloric effect were achieved for the $Ni_{51.5}Mn_{33}In_{15.5}B_{0.3}$ sample. In this composition, an adiabatic temperature change of 6.6 K at 550 MPa, was obtained and an isothermal stress-induced entropy change (ΔS_σ) of 20 J kg^{-1} K^{-1} at an applied stress of 300 MPa. Higher cyclic stability over 150 cycles was achieved for the $Ni_{51.5}Mn_{33}In_{15.5}B_{0.3}$ alloy, while the $Ni_{51.5}Mn_{33}In_{15.5}$ sample (boron-free) degraded with 20 cycles. These outstanding results are due to the improvement of grain boundary cohesion and grain refinement produced by boron microalloying. Fig. 78 compares the effect of boron grain size for different compositions. It is observed that all samples which contain boron exhibit a smaller grain size (~20 μm) compared to the samples without boron (~100 μm).

Tang et al. [274] added Cu to a NiMnIn alloy. Boron was also added to enhance the ductility and the following compositions were

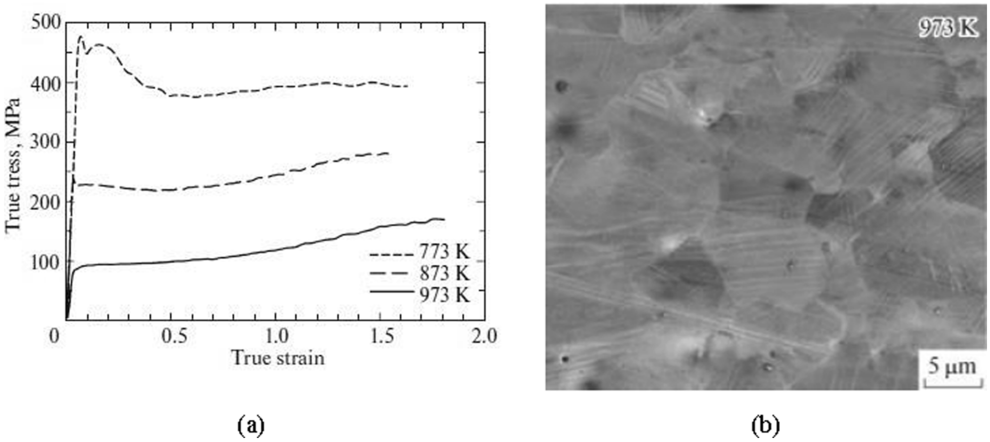

Fig. 75. (a) Compressive true-stress vs true-strain curves for Ni-Mn-In alloy at 773, 873, and 973 K. (b) Structure composed of different twin variants observed on cooling to room temperature. (From Musabirov et al. [271]).

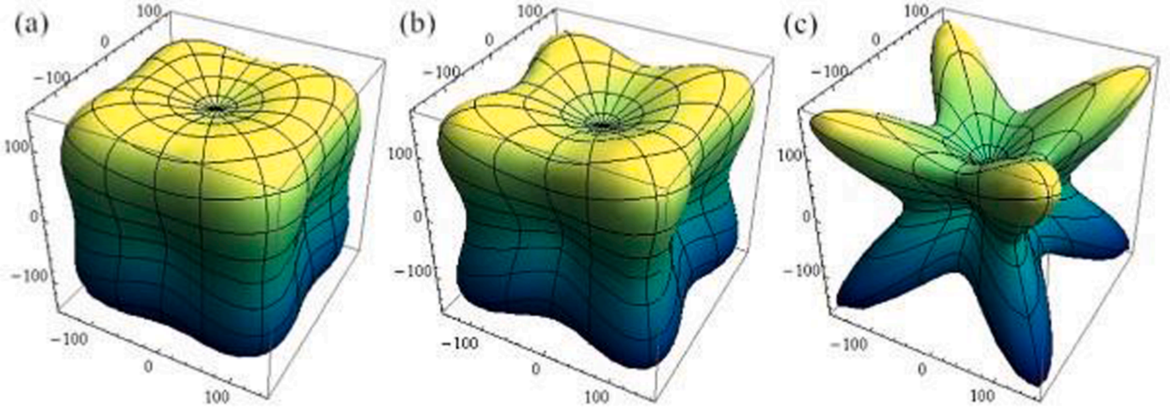

Fig. 76. Polar plots showing anisotropy of elastic moduli of three Heusler alloys Ni_2ScAl, Ni_2TiAl, and Ni_2VAl (From Wen et al. [272]).

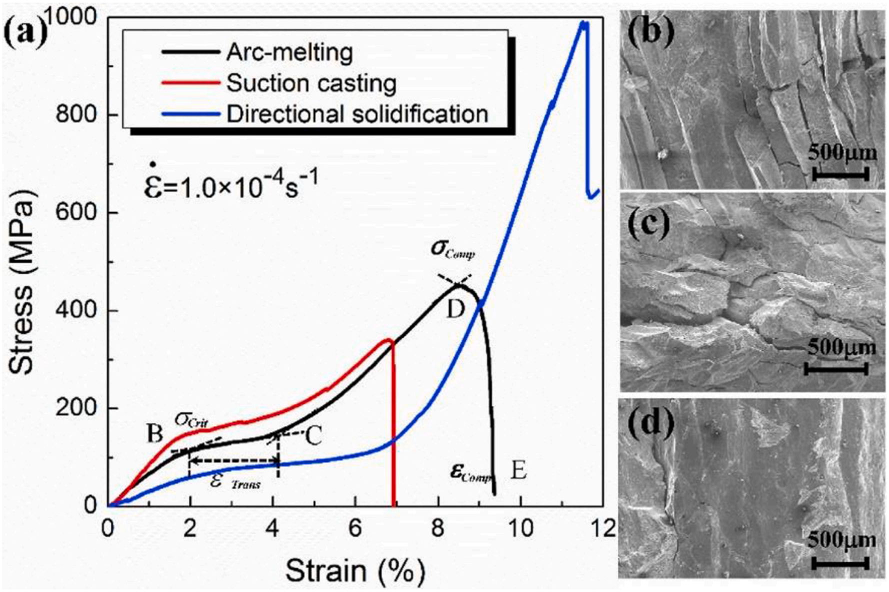

Fig. 77. Mechanical response for $Ni_{50}Mn_{34.8}In_{15.2}$ alloy prepared by three different methods: arc melting, suction casting, and directional solidification. (a) Compressive stress–strain curves up to failure (indicated by the drop in stress). (b-d) surfaces showing brittle failure for arc melting (b), suction casting (c), and directional solidification (d). (From Huang et al. [120]).

investigated: $(Ni_{52}Mn_{31}In_{17\text{-}X}Cu_x)B_{0.2}$ (x: 0, 1, 2, 3). This had a positive effect on the fatigue loading of the alloy up to 100 cycles (Fig. 79). No cracks were detected, and the addition of boron enhanced the properties of the grain boundaries. The adiabatic temperature change was ~ 9.5 K. A major enhancement of ΔT_{ad} to 31.5 K with an associated isothermal entropy change of 45 J/kg^{-1}K^{-1} was obtained by Cong et al. [103] for a NiMnTi all-*d*-metal Heusler alloy. An added advantage is that the working temperature can be tuned to the required heating and cooling applications. The mechanical robustness of these alloys is important in applications. Two ratios of elastic properties provide a good indication of ductility: B/G (where B is the bulk modulus and G is the shear modulus) and the Cauchy pressure C_{11}-C_{44}. The high value of these ratios, in comparison with other Heusler alloys, suggests that the mechanical properties are favorable. The change in volume with transformation, $\Delta V/V_0$ is also considerably higher (Fig. 80). The compressive stress–strain curves obtained at a strain rate of 1.3x10^{-4} s^{-1} for the alloy $Ni_{50}Mn_{31.5}Ti_{18.5}$ microalloyed with boron have a characteristic plateau in which the stress-induced martensitic transformation takes place. The transformation is completely reversible as shown in the insert of Fig. 81, and the entropy change associated with the process can be calculated. This microalloying with boron, similar to the work of Tang et al. [274], enhances the ductility in a manner similar to what has been observed in intermetallics and especially Ni_3Al [275]. It enhances the grain-boundary cohesion and thus overcomes the grain-boundary brittleness.

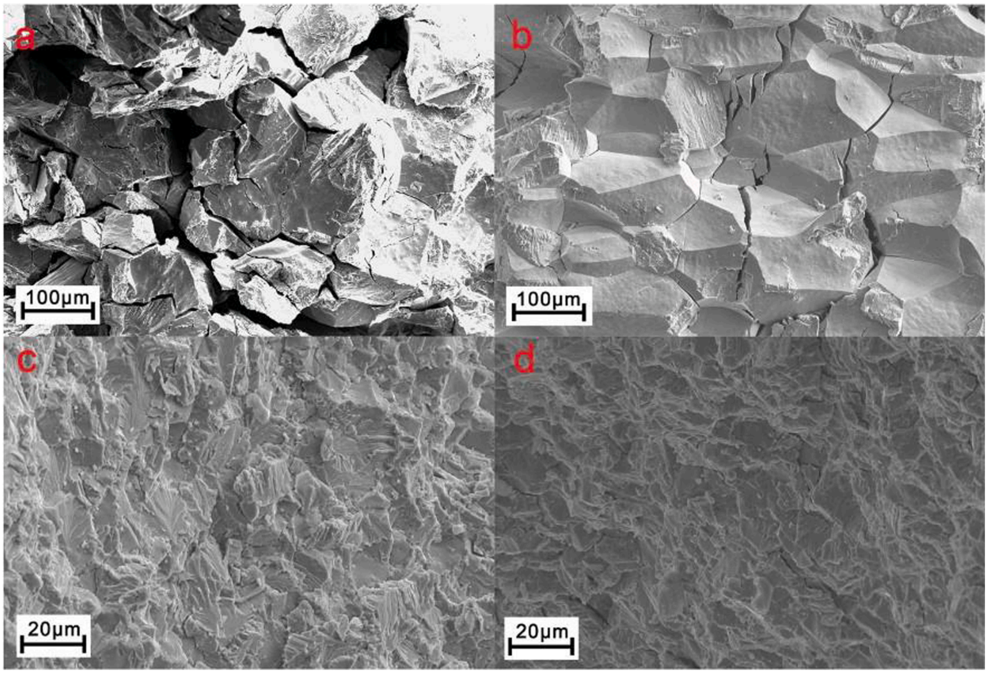

Fig. 78. SEM fractographs showing the reduction of grain size with boron addition. (a) $Ni_{51.5}Mn_{33}In_{15.5}$, (b) $Ni_{51}Mn_{33}In_{14}Fe_2$, (c) $(Ni_{51.5}Mn_{33}In_{15.5})_{99.4}B_{0.6}$ and $(Ni_{51}Mn_{33}In_{14}\ Fe_2)_{99.4}B_{0.6}$ (d). (From Yang et al. ([273]).

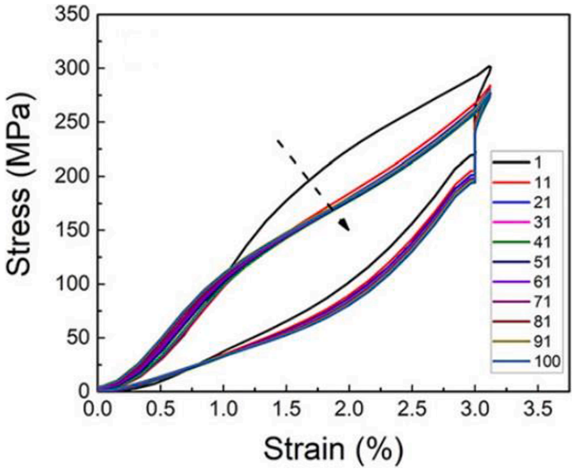

Fig. 79. Stress–strain curves in loading and unloading for $(Ni_{52}Mn_{31}In_{17\text{-}x}Cu_x)B_{0.2}$ (B addition to enhancing grain-boundary properties) at every 10th of the cyclic loading experiment to test the cycling stability of the mechanocaloric effect. There is a drop in the curve *s* for the first ten cycles with subsequent stabilization. (From Tang et al. [274]).

12. Current technological applications

The synthesis of the first "Heusler" alloy dates from the last part of the 19th century. The addition of manganese by Friedrich Heusler was intended to replace the phosphor that collected the oxygen during smelting but contributed to the brittleness of phosphor bronzes, which were originally invented by Georges Montefiori-Levi. Thus, the Cu_2MnSn alloy was initially a structural material. The copper-manganese-tin alloys were successful and other similar alloys followed such as the copper-manganese-nickel alloys known to this date as manganin. The latter have a low-temperature dependence on the electrical resistivity, making them attractive in measuring devices. The discovery of ferromagnetism in the Cu_2MnSn alloy puzzled the scientific community and the underlying reason was finally obtained. Heusler alloys fell in disfavor, and it is fortuitous that one of us (MAM) was given this alloy as a research theme in 1970. The original goal was to measure the enthalpy of ordering through solution calorimetry. Heusler alloys were well suited for this study

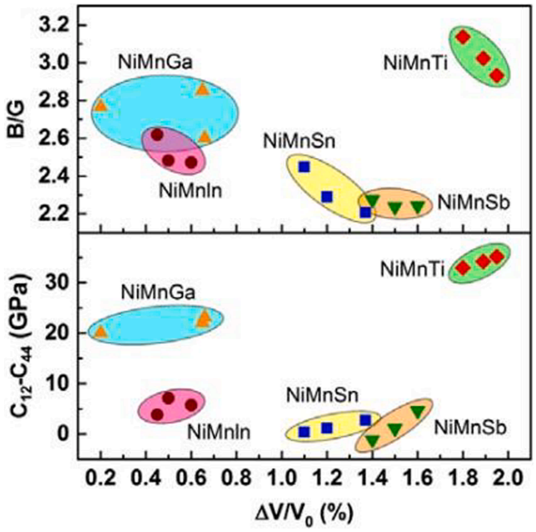

Fig. 80. Top. The ratio between elastic constants B/G for NiMnTi alloys with boron micro addition (top right) and compared to other alloys. Bottom. (C_{12}-C_{44}) for the same materials. Calculations from first principles. (From Cong et al. [103]).

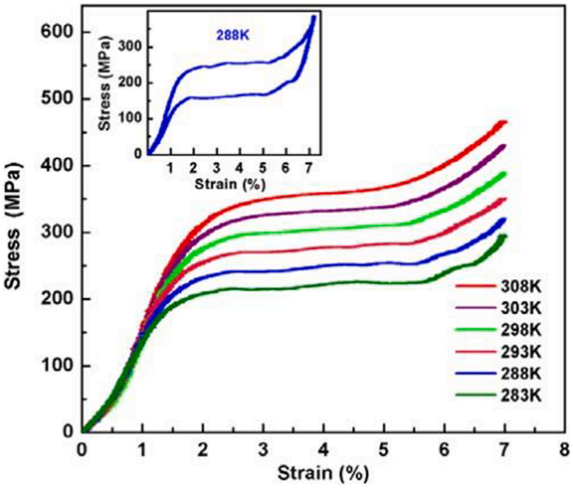

Fig. 81. Compressive stress–strain curves (for the loading cycle only) for $Ni_{50}Mn_{31.5}$ $Ti_{18.5}$ at different temperatures. Only one curve with the full loading–unloading cycle is shown in the insert (From Cong et al. [103]).

because they can be produced in both the ordered and disordered states. It was the discovery of half metallicity by de Groot, in 1983, that reinitiated intense activity around Heusler alloys because of the giant magnetoresistive effect discovered. This era of intense activity has as its goal the development of improved functional properties and new applications. There is not yet a documented functional utilization of Heusler alloys, but they are candidate materials for several concepts.

Among the main applications envisaged for Heusler alloys, spintronics, tunnel junctions, and magnetic thermoelectric devices stand out. There is a broad range of sensors and actuators that can evolve from the half metallicity, magnetocaloric, and giant magnetoresistive properties.

We start with the spintronics area, which is already having a significant impact on information storage. Fig. 82 shows the range of spintronics applications, a highly specialized field subdivided into spin memories, spin sources, and spin transistors. There are basically-two approaches to making Heusler materials for these applications: epitaxial and polycrystalline films. The latter are made by sputtering. Hirohata et al. [157] conclude that polycrystalline films have great advantages over epitaxial films for implementation into GMR or TMR nano-pillar junctions for next-generation HDD read heads or STT-RAM.

The second important application is solid state refrigeration using both the semiconducting properties of Heusler alloys or their multicaloric (mechanocaloric or magnetocaloric, both conventional and inverse) effects (e. g. Mañosa et al. [276]). Usually, the material's entropy decreases when an external field (mechanical, electrical, or magnetic) is applied isothermally, and its temperature increases when a field is applied adiabatically. However, some materials, including Heusler alloys, exhibit the inverse effect. The

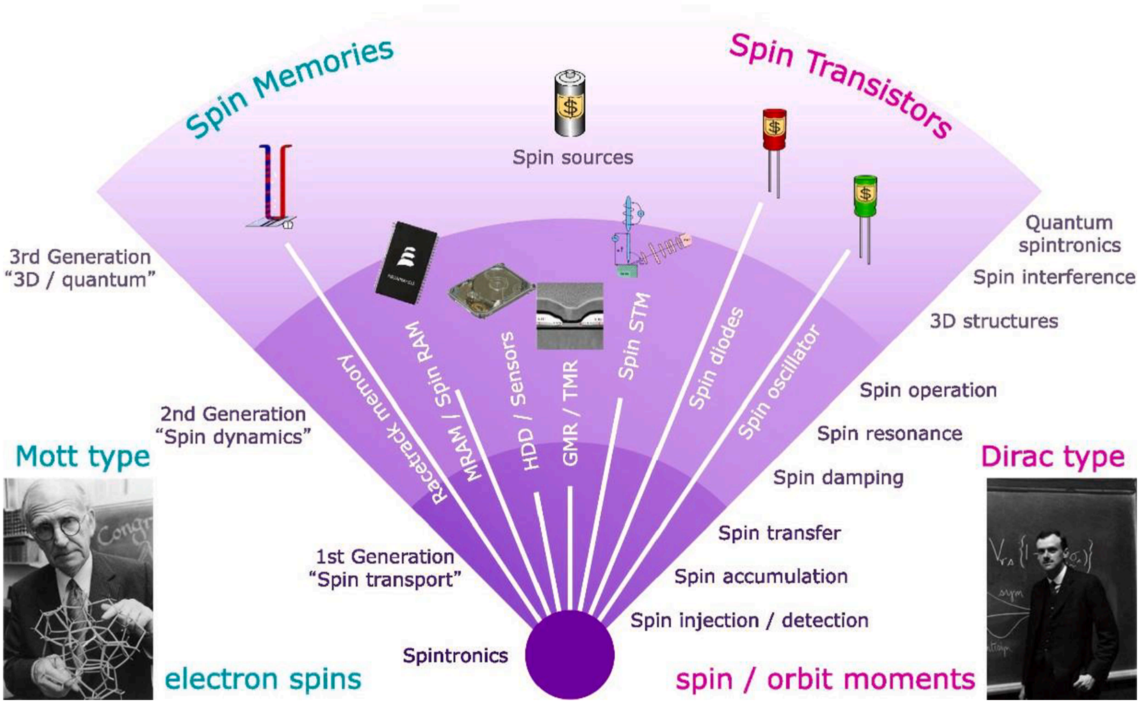

Fig. 82. Application fan of spintronics. (From Hirohata et al. [157]).

conventional and inverse magnetocaloric effects can be obtained in NiMnGa alloys close to the stoichiometric Ni_2MnGa composition (Fig. 83). Fig. 84(a) shows the principle of operation of magnetic solid-state refrigeration. When the field is applied, the temperature rises. Conversely, the specimen cools on the removal of the magnetic field. The change in temperature can be used to create the refrigeration cycle. The corresponding changes in ΔT_{ad} and ΔS_{iso} are shown in Fig. 84(b). A significant number of prototypes using permanent magnets have already been developed in the case of the magnetocaloric effect. Computational simulations can predict improvements in the properties. Siewert et al. [204] suggested that Pt-doping in Ni-Mn-based Heusler alloys improves the performance of these alloys, in particular their magnetocaloric properties. These methods are described in Section 9.

13. Computational design of Heusler alloys

Ab-initio or first-principles electronic structure calculations based on the density functional theory (DFT) are one critical tool today for studying and designing materials at atomic- and nano-scale. Based on the fundamental laws of physics with appropriate approximations, *ab-initio* calculations can access a great variety of materials properties and are playing an increasing role in materials

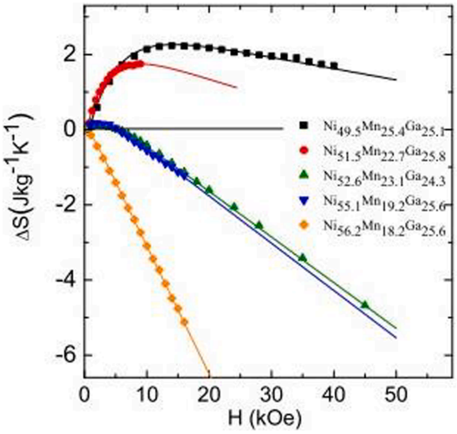

Fig. 83. Entropy change with an externally applied field for different compositions close to Ni_2MnGa. Notice both conventional and inverse magnetocaloric effects. (Adapted from Marcos et al. [326] Phys Rev. 2003).

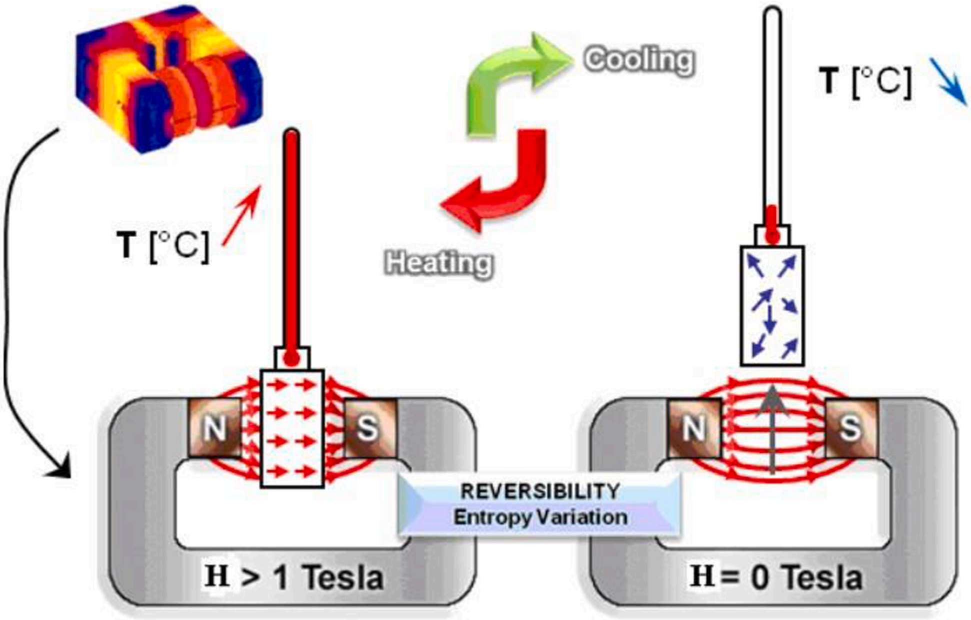

Fig. 84. Principle of operation of magnetic solid state refrigeration: left, specimen between N and S poles of magnet, leading to temperature rise; right, specimen outside of field leading to temperature drop. (b) changes in isothermal entropy and adiabatic temperature with activation of conventional magnetocaloric effect: a decrease in the entropy and an increase in temperature when the field is activated. (From Muller et al [327]).

research. Along with the rapid development of computational hardware and algorithms in the past decades, a so-called high-throughput computational materials design approach based on large-scale *ab-initio* calculations has emerged as one of the most efficient methods to search and design target materials. To date, great efforts have been made to search for the target materials using such an approach, and several selected application examples include the organic–inorganic hybrid perovskite materials for opto-electronics [277–279], perovskite-oxide-based material interfaces [280,281], topological insulators [282], alkali-ion batteries [283–285], and catalysts for hydrogen production [278]. In particular, the high-throughput computational materials design approach offers unique and powerful solutions to accelerate the design and development of the target Heusler alloys with desired properties for various types of technological applications [286–296,296]. This is simply because the Heusler alloys belong to a large family of binary, ternary, and Quaternary compounds that contain hundreds of thousands of materials. The traditional computational studies are limited to one or several compounds at a time and are not efficient for the high-throughput discovery of target Heusler alloys. Accordingly, here we focused on reviewing the high-throughput computational design of novel Heusler alloys, with an emphasis on the general computational workflow, evaluation of the materials stability, and extraction of proper materials descriptors for spintronic and thermoelectric applications.

13.1. Workflow of high-throughput computational design of Heusler compounds

The central idea of the high-throughput computational materials design approach is to carry out large-scale *ab-initio* calculations for many existing and/or hypothetical materials [297–300], and then rapidly identify the materials with the desired properties by screening the calculated quantum materials data. The existing materials structures can be obtained from the inorganic crystal structure database (ICSD) and the hypothetical materials structures can be made from the prototype structures such as the well-known perovskites and Heusler alloys [301]. For example, several open-access quantum materials databases including AFLOWLIB [297], Materials Project [299–302], and Open Quantum Materials Database (OQMD)[298] have been built from the ICSD for public research usage. As for the latter case, i.e., the large-scale *ab-initio* calculations of hypothetical materials, this approach is often used when the materials having the specific prototype structures are the research focus. For example, a high-throughput design of Heusler alloys is one typical example application of such a case.

After large-scale *ab-initio* calculations of hypothetical Heusler alloys, one critical step is to select stable compounds by evaluating their material stability. Several common approaches include formation energy calculations, convex hull calculations, and phonon calculations. Formation energy and convex hull calculations are commonly used to study the thermodynamic stability of materials in a high-throughput fashion. The formation energy (ΔE_f) is directly related to the solid-state formation enthalpy since the change in pressure and volume of the solid materials can be neglected. A negative ΔE_f means that the compound is unlikely to be decomposed into constituent elements. However, it is still possible that the compound is decomposed into other competing phases. Hence, formation energy calculations often serve as the first step in the process of high-throughput design because of the computational cost-effectiveness.

To evaluate the thermodynamic stability of materials against the decomposition into other phases, convex hull calculations are required. A convex hull is a set of lines of formation energies versus compositions for binary compounds (or a surface for ternary compounds). It connects all the lowest energy phases and thus all the competing phases should be considered in the convex hull calculations. Fig. 85 shows convex-hall diagrams for a binary Co-Ti compound and a ternary Mn-Pt-Pd compound. Convex hull distance (ΔE_H) is one effective material parameter to evaluate material stability. It is defined as $\Delta E_H = E_f - H_{hull}$, where E_f is the formation of energy and H_{hull} is the convex hull energy for the considered phase composition. A compound on the convex hull has a zero ΔE_H and is thus thermodynamically stable since its E_f is lower than any other phases or the linear combination of other phases. In contrast, a compound with a large ΔE_H is thermodynamically unstable and is possible to decompose into other competing phases; and the compounds with a relatively small ΔE_H in the order of dozens of meV are potentially stable [303,304]. This is essential because the DFT calculations are generally performed at 0 K and the contributions of entropy to the free energy are neglected. As a result, for some compounds with relatively high entropy, at ambient (or higher) temperature, the total free energy could be further reduced, forming thermodynamically stable states. Hence, the choice of ΔE_H plays a critical role in the prediction of novel Heusler compounds and greatly influences computational accuracy. It is worth mentioning that, in our recent work [303], a comprehensive investigation of the ΔE_H for around 1682 ternary Heusler compounds, we have found that the experimentally synthesized full Heusler and Half Heusler compounds generally have a $\Delta E_H < 100$ meV/atom and $\Delta E_H < 150$ meV/atom, respectively. Accordingly, these values can serve as thresholds to screen thermodynamically stable Heusler compounds from *ab-initio* calculations.

Phonon calculations are often used to assess the dynamic stability of crystalline solids such as Heusler alloys. The common procedure is to calculate the phonon dispersion curve and if all the phonons have real and positive frequencies, then the compounds are considered dynamically stable [277,294]. In addition to the phonon calculations, the calculations of elastic constants (C_{ij}) are often used to evaluate the mechanical stability against deformations and distortions under the strain. A crystal's elastic constants reflect the second-order change of the internal energy in response to a strain and can be calculated using the equation: $C_{ij} = \frac{1}{V_0}\left(\frac{\partial^2 E}{\partial \varepsilon_i \varepsilon_j}\right)$, in which E is the total internal energy, V_0 is the volume of the crystal under the equilibrium condition, and ε_i (ε_j) represents the applied strain. Cubic crystals such as Heusler alloys have three independent elastic constants C_{11}, C_{12}, and C_{44}, and their mechanical stability is determined by the well-known Born stability criteria: $C_{11} - C_{12} > 0$, $C_{11} + 2C_{12} > 0$, and $C_{44} > 0$ [294,305]. These elastic constants can be calculated from *ab-initio* calculations.

13.2. Applications: Examples of high-throughput computational design of Heusler compounds

Discussed below are a few specific examples of the high-throughput search for target Heusler alloys focusing on their magnetic and thermoelectric properties for different functional applications. The high-throughput computational search for target Heusler alloys with the desired magnetic properties such as ferromagnetism, antiferromagnetism, perpendicular magnetic anisotropy (PMA), and high tunnel magnetoresistance (TMR) has been conducted in recent years [306]. For instance, in 2017, Sanvito et al. [306] reported a high-throughput screening of Heusler-based ferromagnetic materials. In this work, they first built a materials database that collects 236,115 Heusler compounds via large-scale *ab-initio* calculations and found 20 magnetic materials by screening the database using a group of material descriptors including formation energy (ΔE_f), convex hull distance (ΔE_H), *d*-block elements, spin moment, and magnetic order. Similarly, Ballueff et al. [289] predicted 21 antiferromagnetic Heusler compounds from 80, 000 Heusler compounds via high-throughput screening of the open-access database AFLOWLIB and density functional theory (DFT)-based magnetic coupling calculations, and all these candidate compounds have a Néel temperature above room temperature. The critical materials descriptors employed in this work include: i) critical elements, ii) spin moment, iii) convex hull distance (ΔE_H), and iv) energy difference between ferromagnetic and antiferromagnetic states.

By taking Sanvito et al.'s [306] work as one example, here briefly reviewed is the procedure of high-throughput screening of target Heusler-based magnets (see Fig. 86). After the large-scale *ab-initio* calculations, the authors carried out a trial screening using two

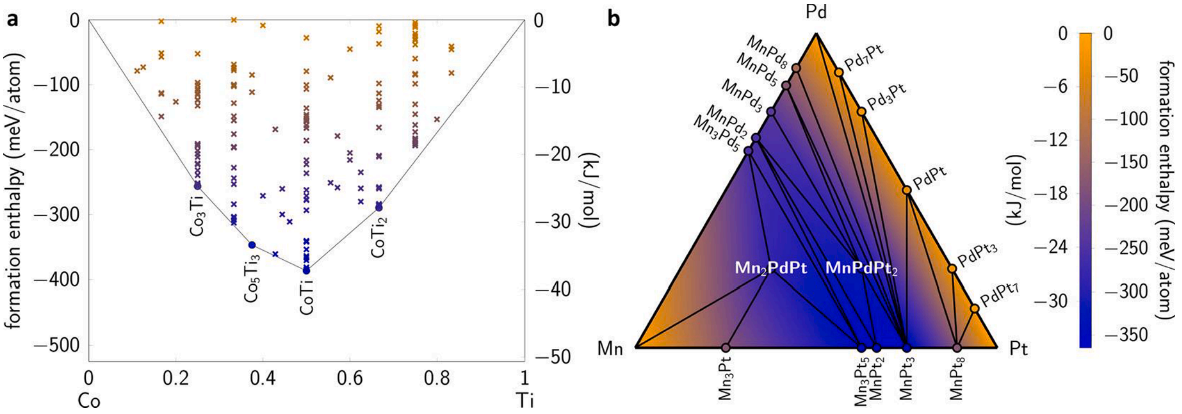

Fig. 85. Convex-hull diagrams. (a) binary compound Co-Ti. (b) ternary compound Mn-Pt-Pd. (From American Chemical Society [328]).

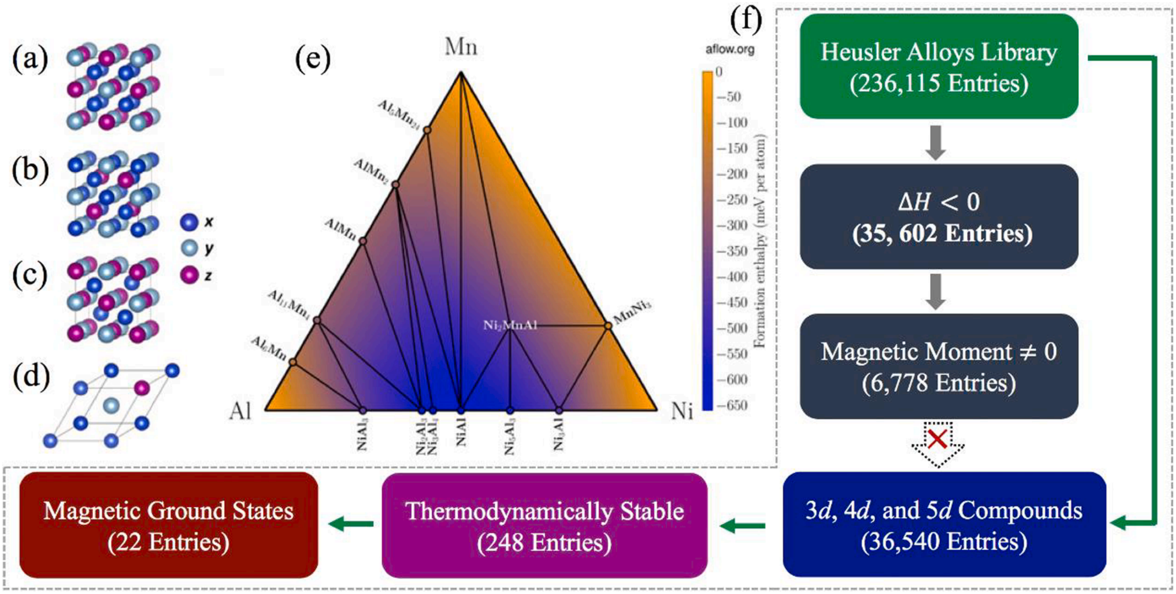

Fig. 86. High-throughput screening of Heusler-based magnets. Basic models of (a) normal Heusler. (b) Inverse Heusler, and (c) Half Heusler. (d) Primitive unit cell to create electronic structure database. (e) Convex hull diagram for Al-Mn-Ni. (f) High-throughput workflow for searching for Heusler-based magnets. Adapted and redesigned (From Yang [301] and Sanvito et al. [306]).

materials parameters including formation enthalpy and magnetic moment and realized that this screening strategy is extremely challenging because it requires the total energy calculations of approximately 15 million prototypes to determine the stability of each calculated Heusler compound. Instead, Sanvito et al. [306] narrowed down the materials search space to the intermetallic compounds that consist of 3*d*, 4*d*, and 5*d* elements. They conducted a convex hull analysis using the available energetic data of the binary and ternary compounds in the AFLOWLIB [297] and found 248 thermodynamically stable compounds from the 36, 540 compounds. This strategy significantly reduced the number of candidate compounds and improved the screening efficiency. The authors further carried out magnetic coupling calculations for the 248 compounds and identified 20 new ferromagnetic materials that belong to Co_2YZ, Mn_2YZ, and X_2MnZ classes, suggesting that Co and Mn elements are critical in producing the magnetic ground states. It is worth mentioning that they successfully synthesized a new ferromagnetic compound, Co_2MnTi, which displays a Curie temperature (T_C) as high as 938 K, surprisingly in excellent agreement with the predicted value of 940 K via a linear regression method over the existing data.

Large-scale *ab-initio* calculations can also be employed to study the fundamental structure–property relationship for Heusler alloys. For example, Faleev et al. [307] explored the stability of the tetragonal phase of X_2YZ Heusler compounds by comparing the relative stability between the cubic and tetragonal phases using first-principles calculations for a subset of 286 compounds. Based on these data, the authors soon reported an approach to search for tetragonal Heusler compounds with large PMA and TMR for high-density memory recording applications [308]. The key materials descriptors used for selecting candidate materials include volume magnetic anisotropy (K_v), the strength of the Brillouin zone (BZ) spin filtering effect (E_z), and total spin polarization (P_f). Faleev et al. [308] further carried out experimental verification for the candidates and identified 11 experimentally stable tetragonal Heusler compounds among which 9 have PMA. Interestingly, the compound Fe_2MnGa was reported to be tetragonal in the experiment while predicted to be cubic from DFT calculations, in which the calculated total energy of the tetragonal phase is about 0.03 eV higher than that of the cubic phase. This energy difference is less than the established threshold value of 100 meV/atom for ΔE_H mentioned above, implying that the tetragonal phase is likely to be thermodynamically stable due to the entropy effects.

Inverse Heusler compounds have also been studied for promising spintronic applications. For instance, Ma et al. [309] calculated 405 Inverse Heusler compounds using large-scale *ab-initio* calculations and identified about 51 half-metals and 50 near half-metals. One interesting finding from this work is that most experimentally synthesized Inverse Heusler compounds have a $\Delta E_H < 52$ meV/atom, which could serve as one useful reference to select thermodynamically stable compounds from the Inverse Heusler family. However, in this work, the material stability of the identified candidate spintronic materials was only evaluated from the negative formation energy rather than through the convex hull analysis, and thus the thermodynamic stability of these candidate materials should be further examined before considering their practical applications. Half Heusler compounds are another ideal materials platform for searching for spintronic materials [310]. Interestingly, it is found that most experimentally synthesized compounds have a$<100\Delta E_H$ meV/atom that is larger than that of the inverse Full Heusler compounds, 52 meV/atom [309]. This also implies a larger entropy in the Half Heusler compounds than that in the Full Heusler compounds. Similarly, one can expect that a large ΔE_H (100 – 150 meV/atom) can be used for selecting stable Quaternary Heusler compounds because of their large entropy [290,294,304].

Besides spintronic properties, Heusler compounds also offer promising thermoelectric properties, and many computational design efforts of thermoelectric materials based on the Heusler compounds have been made in recent years [286,287,293,295,311–314]. In 2014, Carrete et al. [286] first reported the high-throughput search for thermoelectric materials based on the Half Heusler compounds. In this work, most of the computational efforts were focused on the evaluation of material stability. The authors screened 79,057 compounds belonging to the Half Heusler structure and identified 75 stable compounds after using materials descriptors including negative formation enthalpies, band gaps, photon dispersion curves, and ternary phase diagram (ΔE_H). Among the 75 stable compounds, the authors proposed the three promising thermoelectric materials, PtLaSb, RhLaTe, and SbNaSr, which have the lowest thermal conductivity for future experimental verification. In contrast, SbNaSr was later found dynamically unstable via phonon dispersion calculations [315], and hence further computational or/and experimental efforts are required to clarify the inconsistency. A similar computational search of thermoelectric materials with low thermal conductivity was also carried out for Full Heusler compounds. For instance, He et al. [311] reported a new class of Full Heusler compounds that have ten valence electrons using the high-throughput *ab-initio* computational approach and identified 15 promising X_2YZ compounds as thermoelectric materials. As in the case of other high-throughput screening work, a large portion of the research efforts were focused on the determination of the thermodynamic stability of compounds.

The emerging machine learning approach has also been employed as one supplementary tool in the high-throughput *ab-initio* design of target materials when the traditional *ab-initio* calculations are not approachable to obtain the desired materials data, which could be because of either the extremely large-size computational task or the unavailability of *ab-initio* calculations. This has been enabled by the rapid development of computer algorithms. For instance, Carrete et al. [286] employed machine learning techniques to predict lattice thermal conductivity in their work on the high-throughput search for thermoelectric materials. In 2018, Kim et al. [290] reported 55 novels Quaternary Heusler compounds using a combinatorial approach involving machine learning techniques and high-throughput ab-initio calculations. The machine learning approach was employed to evaluate the thermodynamic stability of about 3.2 million possible structures by estimating the convex hull distance and identifying 303 candidate materials (with $\Delta E_H < 100$ meV/atom) for accurate ab-initio calculations. This work indicates that machine learning approach is rather effective to estimate the stability of materials and thus can significantly accelerate the discovery of novel materials.

14. Conclusions, perspectives, and recommendations

Heusler alloys have a fascinating story that involved three family members. The first, C. Heusler, added Mn to bronze to improve its properties. The ferromagnetism in Heusler alloys, discovered in 1898 by F. Heusler, has been shown to be the result of their ordered BCC structure with an FCC superlattice. The structure was determined because of advances in X-ray diffraction. This was done by O. Heusler, Fredrich Heusler's son, in 1934; a more detailed simultaneous study by Bradley reached the same conclusion. Eventually, the correct source of ferromagnetism, the ordered $L2_1$ structure which separated the Mn atoms at a critical distance, was reached through X-ray diffraction. The constituent elements not being ferromagnetic, this discovery led to numerous studies investigating its origin. The original Cu_2MnZ (where Z is Sn, Al, As, W, Sb, or B) definition has been expanded to include other classes. The contemporary designation is Full Heusler (with stoichiometry $X_2Y_1Z_1$), Half Heusler (with stoichiometry $X_1Y_1Z_1$), Inverse Heusler, Binary Heusler, Binary Heusler, and Quaternary Heusler. In addition to ferromagnetism, many other effects that render them important for functional applications are being revealed. Although the numbers depend on the measurement method, over 1,500 Heusler alloys exist today, covering a range of potential applications. However, the possible number, as possible through computer simulation, is in the millions. Thus, Heusler alloys are the functional equivalent to the structural characteristics of High Entropy Alloys. Some of the functional properties and distinct characteristics of Heusler alloys are reviewed below.

Half metallicity, discovered in some alloys, starting with the classic discovery by de Groot in 1983 (in the half-Heusler alloy NiMnSb), gives them electronic properties between metals and semiconductors. The discovery of half metallicity in Heusler alloys led to the giant magnetoresistance effect, and gave a great impulse to research and opened the door to a cornucopia of potential applications that also use the magnetic shape memory effect:

- Spintronic hard disk drive heads and magnetic random-access memory.
- Thermoelectric devices
- Sensors and actuators
- Superconductors and semiconductors
- Topological insulator materials.

Some of these applications are briefly reviewed her.

Spintronics (or spin transport electronic) applications. This is a rather new concept through which information is carried not by the electrons but by their spin. This Nobel-prize discovery (given in 2007 to Grünberg and Fert) led to the application in computer science, specifically in hard drive reading heads and magnetic random-access memory (MRAM). Most of the current generation read heads use spintronic technology. Although the principal materials used are oxide compounds (e.g., CrO_2 and Fe_3O_4), perovskites, and magnetic semiconductors (e.g., EuO, EuS, and (Ga, Mn) As, CrAs), Heusler alloys are being seriously considered. In particular, CoFeSi and $Co_2Cr_{0.6}Fe_{0.4}$ have been seriously investigated (Felser and Fecher [316]).

Magnetic shape memory effect: this is another unique property exhibited by some Heusler alloys, analogous to the better-known mechanical shape memory effect exhibited by, among others, the NiTiNol compound. Martensite can form and be uniform under the effect of an imposed external magnetic field. If the process is an adiabatic process, there is an increase in temperature when the external field is applied (direct/conventional magnetocaloric effect). If there is a temperature decrease, we have the inverse magnetocaloric effect. This adiabatic temperature change can be incorporated into a Carnot or Rankine cycle. Practical refrigeration applications require this reversibility to occur close to or at ambient temperature. For a brief time, GE produced a portable refrigerator using the magnetocaloric effect. One important advantage of this form of refrigeration is that no gases with negative environmental effects (such as freon) are used. Another advantage is that losses due to heat conversion are decreased.

Multicaloric effect. In addition to externally applied magnetic fields affecting the martensitic transformation (the magnetocaloric effect), pressure (barocaloric effect) and uniaxial stress (elastocaloric effect) can be applied to enhance the performance of Heusler alloys. The significant environmental and efficiency advantages of solid-state refrigeration warrant focused research on this effect. All-*d*-metal Heusler alloys, formed by only transition metals, exhibit a multicaloric effect and high mechanical properties as reported by Azanar et al. [234], Wei et al. [257], and Cong et al. [103]. This behavior makes these alloys promising candidates for applications in solid-state refrigeration.

Topological insulator (TI) materials This is a new state of quantum matter because the wave functions describing them have a non-trivial Hilbert space topology. Cd/Te/HgTe/CdTe quantum wells is an example of 2D TI whereas Bi1-xSbx is an early 3D TI. Some ternary Half Heusler alloys can be classified as TI materials: YPtBi and LuPtBi. They are candidate materials for spintronics. Felser's group identified 50 of such materials.

Some Heusler alloys have outstanding magneto-electronic properties in bulk, but the fabrication of thin films still presents challenges. Thus, there are currently no applications in industrially produced devices, but the intense investigations globally are advancing the capabilities of these materials. The use of high-throughput computational material design is accelerating the discovery of new alloys with tailored functional properties. In spite of the approximately 6,000 research papers published on Heusler alloys, there is a scarcity of studies on their mechanical properties. Nevertheless, these are important to the robustness of devices.

Most Heusler alloys are intermetallic and have an ordered structure. The loss of ordering also degrades the properties. They tend to have high hardness, yield stress, and low ductility. It is amazing that little quantitative experimental work has been done on the mechanical properties. First-principles and molecular dynamics calculations can predict the elastic properties realistically, but plasticity, strength, and toughness require experimental work, which involves making casts of sufficient size, and heat treating them in the appropriate conditions to retain the ordered structure, machining specimens, and testing them. This is an area ripe for systematic inquiry.

Declaration of Competing Interest

The authors declare that they have no known competing financial interests or personal relationships that could have appeared to influence the work reported in this paper.

Acknowledgement

We thank the UC San Diego Senate for granting us a Senate Research Grant Award which enable the writing of this review article.

References

[1] Groot RA, Mueller FM, van Engen PG, Buschow KHJ. New Class of Materials: Half-Metallic Ferromagnets. Phys Rev Lett 1983;50:2024–7. https://doi.org/10.1103/PhysRevLett.50.2024.

[2] Heusler Alloys Publications. Web Sci 2021. https://www.webofscience.com/wos/woscc/analyze-results/df46b0b5-4430-4bb0-acc5-5f6970011322-0637da2a.

[3] Meyers MA. Some observation on the Cu-Mn-Sn system. University of Denver 1971.

[4] Wollmann L, Nayak AK, Parkin SSP, Felser C. Heusler 4.0: Tunable Materials. Annu Rev Mater Res 2017;47:247–70. https://doi.org/10.1146/annurev-matsci-070616-123928.

[5] Balke B, Wurmehl S, Fecher GH, Felser C, Kübler J. Rational design of new materials for spintronics: Co_2FeZ (Z=Al, Ga, Si, Ge). Sci Technol Adv Mater 2008;9:14102. https://doi.org/10.1088/1468-6996/9/1/014102.

[6] Graf T, Parkin SSP, Felser C. Heusler Compounds—A Material Class With Exceptional Properties. IEEE Trans Magn 2011;47:367–73. https://doi.org/10.1109/TMAG.2010.2096229.

[7] Graf T, Felser C, Parkin SSP. Simple rules for the understanding of Heusler compounds. Prog Solid State Chem 2011;39:1–50. https://doi.org/10.1016/j.progsolidstchem.2011.02.001.

[8] Felser C, Wollmann L, Chadov S, Fecher GH, Parkin SSP. Basics and prospective of magnetic Heusler compounds. APL Mater 2015;3:41518. https://doi.org/10.1063/1.4917387.

[9] Felser C, Hirohata A, editors. Heusler Alloys: Properties. Growth: Applications. Springer International Publishing; 2016.

[10] Galanakis I. Theory of Heusler and Full-Heusler Compounds. In: Felser C, Hirohata A, editors. Heusler Alloy. Prop. Growth, Appl., Springer Series In Materials Science; 2016, p. 3–36. 10.1007/978-3-319-21449-8.

[11] Felser C, Wollmann L, Chadov S, Fecher GH. Basics and Prospectives of Magnetic Heusler Compounds. In: Felser C, Hirohata A, editors. Heusler Alloy. Prop. Growth, Appl., Springer Series In Materials Science; 2016, p. 37–48. 10.1007/978-3-319-21449-8.

[12] Fetzer R, Aeschlimann M, Cinchetti M. Spin-Resolved Photoemission Spectroscopy of the Heusler Compound Co_2MnSi. In: Felser C, Hirohata A, editors. Heusler Alloy. Prop. Growth, Appl., Springer Series In Materials Science; 2016, p. 51–86. 10.1007/978-3-319-21449-8.

[13] Wurmehl S, Wójcik M. Structural Order in Heusler Compounds. In: Felser C, Hirohata A, editors. Heusler Alloy. Prop. Growth, Appl., Springer Series In Materials Science; 2016, p. 87–109. 10.1007/978-3-319-21449-8.

[14] Bende D, Grin Y, Wagner FR. Chemical Bonding in MgAgAs-Type Compounds. In: Felser C, Hirohata A, editors. Heusler Alloy. Prop. Growth, Appl., Springer Series In Materials Science; 2016, p. 133–56. 10.1007/978-3-319-21449-8.

[15] Meyer J, Teichert N, Auge A, Wang C, Hutten A, Felser C. Heusler Compounds Go Nano. In: Felser C, Hirohata A, editors. Heusler Alloy. Prop. Growth, Appl., Springer Series In Materials Science; 2016, p. 111–32. 10.1007/978-3-319-21449-8.

[16] Hirohata A, Sagar J, Fleet L., Parkin SSP. Heusler Alloy Films for Spintronic Devices. In: Felser C, Hirohata A, editors. Heusler Alloy. Prop. Growth, Appl., Springer Series In Materials Science; 2016, p. 219–48. 10.1007/978-3-319-21449-8.

[17] Sakuraba Y, Takanashi K. Giant Magnetoresistive Devices with Half-Metallic Heusler Compounds. In: Felser C, Hirohata A, editors. Heusler Alloy. Prop. Growth, Appl., Springer Series In Materials Science; 2016, p. 389–400. 10.1007/978-3-319-21449-8.
[18] Krez J, Balke B. Thermoeletric Heusler Compounds. In: Felser C, Hirohata A, editors. Heusler Alloy. Prop. Growth, Appl., Springer Series In Materials Science; 2016, p. 249–67. 10.1007/978-3-319-21449-8.
[19] Song Y, Leighton C, James RD. Thermodynamics and Energy Conversion in Heusler Alloys. In: Felser C, Hirohata A, editors. Heusler Alloy. Prop. Growth, Appl., Springer Series In Materials Science; 2016, p. 269–91. 10.1007/978-3-319-21449-8.
[20] Takahashi YK, Hono K. Spin Polarization in Heusler Alloy Films. In: Felser C, Hirohata A, editors. Heusler Alloy. Prop. Growth, Appl., Springer Series In Materials Science; 2016, p. 295–318. 10.1007/978-3-319-21449-8.
[21] Felser C, Chadov S. Topological Insulators within the Family of Heusler Materials. In: Felser C, Hirohata A, editors. Heusler Alloy. Prop. Growth, Appl., Springer Series In Materials Science; 2016, p. 465–77. 10.1007/978-3-319-21449-8.
[22] Heusler C. Verein zur Beforderung des Gewerbleisses. VerhVerBeforddGewerbfl 1881.
[23] Heusler F. Über Manganbronze und über die Synthese magnetisierbarer Legierungen aus unmagnetischen Metallen. Zeitschrift Für Angew Chemie 1904;17: 260–4. doi: 10.1002/ange.19040170903.
[24] Hsu C-Y, Hsu K-C, Murr LE, Meyers MA. The Attenuation of Shock Waves in Nickel BT - Shock Waves and High-Strain-Rate Phenomena in Metals: Concepts and Applications. In: Meyers MA, Murr LE, editors., Boston, MA: Springer US; 1981, p. 433–52. 10.1007/978-1-4613-3219-0_27.
[25] Uber HF. Uber Magnetischen Manganlegierungen. Verhandlungen Der Dtsch Phys Gesellschaft 1903;5:219.
[26] Heusler F, Starck W, Haupt E. Magnetisch-chemische Studien. Verhandlungen Der Dtsch Phys Gesellschaft 1903;5:220–32.
[27] Hume-Rothery W. Electrons, atoms, metals and alloys. AIChE J 1956;2:18J–20J. https://doi.org/10.1002/aic.690020233.
[28] Uber HE. Uber Die Ferromagnetischen Eigenschaften Von Legierungen Unmagnetischer Metalle. Ges Naturw 1904;13:257–63.
[29] Honda K. Die Magnetisierung einiger Legierungen als Funktion ihrer Zusammensetzung und Temperatur. Ann Phys 1910;337:1003–26. https://doi.org/10.1002/andp.19103371005.
[30] Take E, Semm A. Magnetisch Heuslerschen Legierungen. Verhandlungen Der Dtsch Phys Gesellschaft 1964;32:971.
[31] Ross AD, Gray RC. On the Magnetism of the Copper-Manganese-Tin Alloys under varying Thermal Treatment. Proc R Soc Edinburgh 1912;31:85–99. https://doi.org/10.1017/S0370164600025025.
[32] Carapella AL, Hultgren R. The Ferromagnetic Nature of the Beta Phase in the. Copper-Manganese-Tin System Trans Am Inst Min Metall Eng 1942;147:232–42.
[33] Heusler F, Take E. The Nature of the Heusler Alloys. Trans Faraday Soc 1912;61:169–84. https://doi.org/10.1039/TF9120800169.
[34] Heusler F, Richarz F. Studien über magnetisierbare Manganlegierungen. Zeitschrift Für Anorg Chemie 1909;61:265–79. https://doi.org/10.1002/zaac.19090610121.
[35] Ross AD. On the magnetic properties and microstructure of the Heusler alloys. Trans Faraday Soc 1912;8:185–94. https://doi.org/10.1039/TF9120800185.
[36] Harang L. On the Crystal Structure of the Heusler Alloys. Zeitschrift Für Krist 1927;65:261.
[37] Persson E. "Röntgenanalyse der Heuslerschen Legierungen", das Mangan-Aluminun-Kupfer. Zeitschrift Für Anorg Und Allg Chemie 1928;171:126–42.
[38] Heusler O. Zur Kenntnis der Heusler'schen Legierungen. Über das Mangan-Aluminium-Kupfer. Zeitschrift Für Anorg Und Allg. Chemie 1928;171:126–42. https://doi.org/10.1002/zaac.19281710112.
[39] West DFR, Thomas DJ. The Constitution of Copper-Rich Alloys of the Copper-Manganese-Aluminum System. J Ind Met 1956;85:97–104.
[40] Potter HH. The X-ray structure and magnetic properties of single crystals of Heusler alloy. Proc Phys Soc 1928;41:135–42. https://doi.org/10.1088/0959-5309/41/1/314.
[41] Persson E. Über den Bau der Heuslerschen Legierungen. Zeitschrift Für Phys 1929;57:115–33. https://doi.org/10.1007/BF01339855.
[42] Valentiner S, Becker G. Untersuchungen an Heuslerschen Legierungen. Zeitschrift Für Phys 1933;83:371–403. https://doi.org/10.1007/BF01342096.
[43] Heusler O. Kristallstruktur und Ferromagnetismus der Mangan-Aluminium-Kupferlegierungen. Ann Phys 1934;411:155–201. https://doi.org/10.1002/andp.19344110205.
[44] Bradley AJ, Rodgers JW, Bragg WL. The crystal structure of the heusler alloys. Proc R Soc London Ser A, Contain Pap a Math Phys Character 1934;144:340–59. https://doi.org/10.1098/rspa.1934.0053.
[45] Valentiner S. Über den Ersatz des Aluminiums und des Zinns durch Indium in den Heuslerschen Legierungen. Naturwissenschaften 1947;34:123–4. https://doi.org/10.1007/BF00602642.
[46] Grinstead RR, Yost DM. Ferromagnetic Alloys in the System Copper-Manganese-Indium. Phys Rev 1949;75:984–5. https://doi.org/10.1103/PhysRev.75.984.
[47] Coles BR, Hume-Rothery W, Myers HP. The structure and properties of the alloy Cu_2MnIn. Proc R Soc London Ser A Math Phys Sci 1949;196:125–33. https://doi.org/10.1098/rspa.1949.0019.
[48] Hames FA, Eppelsheimer DS. Some New Ferromagnetic Manganese Alloys. Nature 1948;162:968. https://doi.org/10.1038/162968a0.
[49] Valentiner S. Zur Kenntnis des Systems Kupfer-Mangan-Zinn. Zeitschrift Fuer Met 1953;44:59–64.
[50] Taglang P, Asch G. Etude paramagnetique et thermique de l'alliage de Hesuler MnSnCu2. Comptes Rendus 1954;238:2500–3.
[51] Gladyshevskii EI, Kripyakevich PI, Teslyuk MY. Crystal Structures of Some Intermetallic Compounds. Sov Physics, Crystallogr 1961;6:207–8.
[52] Taglang P, Fournier M. Sur les transformations de l'alliage MnSnCu2. J Phys Radium 1961;22:295–7.
[53] Oxley DP, Tebble RS, Williams KC. Heusler Alloys. J Appl Phys 1963;34:1362–4. https://doi.org/10.1063/1.1729511.
[54] Johnston GB, Hall EO. Studies on the Heusler alloys—II. The structure of Cu3Mn2Al. J Phys Chem Solids 1968;29:201–7. https://doi.org/10.1016/0022-3697(68)90063-2.
[55] Johnston GB, Hall EO. Studies on the Heusler alloys—I. Cu2MnAl and associated structures. J Phys Chem Solids 1968;29:193–200. https://doi.org/10.1016/0022-3697(68)90062-0.
[56] Forster RH, Johnston GB, Wheeler DA. Studies on the heusler alloys—III. The antiferro-magnetic phase in the Cu-Mn-Sb system. J Phys Chem Solids 1968;29: 855–61. https://doi.org/10.1016/0022-3697(68)90147-9.
[57] Webster PJ. Magnetic and chemical order in Heusler alloys containing cobalt and manganese. J Phys Chem Solids 1971;32:1221–31. https://doi.org/10.1016/S0022-3697(71)80180-4.
[58] Webster PJ, Ziebeck KRA. Magnetic and chemical order in Heusler alloys containing cobalt and titanium. J Phys Chem Solids 1973;34:1647–54. https://doi.org/10.1016/S0022-3697(73)80130-1.
[59] Meyers MA, Ashworth E. A model for the effect of grain size on the yield stress of metals. Philos Mag A 1982;46:737–59. https://doi.org/10.1080/01418618208236928.
[60] Meyers MA, Ruud CO, Barrett CS. Observations on the Ferromagnetic Beta Phase of the Cu-Mn-Sn System. Crystallogr J Appl 1973;6:39–41. https://doi.org/10.1107/S0021889873008022.
[61] Ziebeck KRA, Webster PJ. A neutron diffraction and magnetization study of Heusler alloys containing Co and Zr, Hf, V or Nb. J Phys Chem Solids 1974;35:1–7. https://doi.org/10.1016/0022-3697(74)90002-X.
[62] Noda Y, Ishikawa Y. Spin Waves in Heusler Alloys Pd2MnSn and Ni2MnSn. J Phys Soc Japan 1976;40:690–8. https://doi.org/10.1143/JPSJ.40.690.
[63] Buschow KHJ, van Engen PG. Magnetic and magneto-optical properties of heusler alloys based on aluminium and gallium. J Magn Magn Mater 1981;25:90–6. https://doi.org/10.1016/0304-8853(81)90151-7.
[64] Galanakis I, Dederichs PH, Papanikolaou N. Origin and properties of the gap in the half-ferromagnetic Heusler alloys. Phys Rev B 2002;66:134428. https://doi.org/10.1103/PhysRevB.66.134428.
[65] Galanakis I, Dederichs PH, Papanikolaou N. Slater-Pauling behavior and origin of the half-metallicity of the full-Heusler alloys. Phys Rev B 2002;66:174429. https://doi.org/10.1103/PhysRevB.66.174429.
[66] Galanakis I. Appearance of half-metallicity in the quaternary Heusler alloys. J Phys Condens Matter 2004;16:3089–96. https://doi.org/10.1088/0953-8984/16/18/010.
[67] Galanakis I. Orbital magnetism in the half-metallic Heusler alloys. Phys Rev B 2005;71:12413. https://doi.org/10.1103/PhysRevB.71.012413.

[68] Şaşıoğlu E, Sandratskii LM, Bruno P, Galanakis I. Exchange interactions and temperature dependence of magnetization in half-metallic Heusler alloys. Phys Rev B 2005;72:184415. https://doi.org/10.1103/PhysRevB.72.184415.

[69] Galanakis I, Mavropoulos P, Dederichs PH. Electronic structure and Slater-Pauling behaviour in half-metallic Heusler alloys calculated from first principles. J Phys D Appl Phys 2006;39:765–75. https://doi.org/10.1088/0022-3727/39/5/s01.

[70] Galanakis I, Şaşıoğlu E. High TC half-metallic fully-compensated ferrimagnetic Heusler compounds. Appl Phys Lett 2011;99:52509. https://doi.org/10.1063/1.3619844.

[71] Skaftouros S, Özdoğan K, Şaşıoğlu E, Galanakis I. Generalized Slater-Pauling rule for the inverse Heusler compounds. Phys Rev B 2013;87:24420. https://doi.org/10.1103/PhysRevB.87.024420.

[72] Özdoğan K, Şaşıoğlu E, Galanakis I. Slater-Pauling behavior in LiMgPdSn-type multifunctional quaternary Heusler materials: Half-metallicity, spin-gapless and magnetic semiconductors. J Appl Phys 2013;113:193903. https://doi.org/10.1063/1.4805063.

[73] Wurmehl S, Fecher GH, Kandpal HC, Ksenofontov V, Felser C, Lin H-J. Investigation of Co_2FeSi: The Heusler compound with highest Curie temperature and magnetic moment. Appl Phys Lett 2006;88:32503. https://doi.org/10.1063/1.2166205.

[74] Wurmehl S, Fecher GH, Ksenofontov V, Casper F, Stumm U, Felser C, et al. Half-metallic ferromagnetism with high magnetic moment and high Curie temperature in Co_2FeSi. J Appl Phys 2006;99:08J103. https://doi.org/10.1063/1.2167330.

[75] Ksenofontov V, Melnyk G, Wojcik M, Wurmehl S, Kroth K, Reiman S, et al. Structure and properties of CoMnSb in the context of half-metallic ferromagnetism. Phys Rev B 2006;74:134426. https://doi.org/10.1103/PhysRevB.74.134426.

[76] Kandpal HC, Fecher GH, Felser C. Calculated electronic and magnetic properties of the half-metallic, transition metal based Heusler compounds. J Phys D Appl Phys 2007;40:1507–23. https://doi.org/10.1088/0022-3727/40/6/s01.

[77] Dai X, Liu G, Fecher GH, Felser C, Li Y, Liu H. New quarternary half metallic material CoFeMnSi. J Appl Phys 2009;105:07E901. https://doi.org/10.1063/1.3062812.

[78] Alijani V, Winterlik J, Fecher GH, Naghavi SS, Felser C. Quaternary half-metallic Heusler ferromagnets for spintronics applications. Phys Rev B 2011;83:184428. https://doi.org/10.1103/PhysRevB.83.184428.

[79] Alijani V, Ouardi S, Fecher GH, Winterlik J, Naghavi SS, Kozina X, et al. Electronic, structural, and magnetic properties of the half-metallic ferromagnetic quaternary Heusler compounds CoFeMnZ (Z=Al, Ga, Si. Ge Phys Rev B 2011;84:224416. https://doi.org/10.1103/PhysRevB.84.224416.

[80] Casper F, Graf T, Chadov S, Balke B, Felser C. Half-Heusler compounds: novel materials for energy and spintronic applications. Semicond Sci Technol 2012;27:63001. https://doi.org/10.1088/0268-1242/27/6/063001.

[81] Jourdan M, Minár J, Braun J, Kronenberg A, Chadov S, Balke B, et al. Direct observation of half-metallicity in the Heusler compound Co2MnSi. Nat Commun 2014;5:3974. https://doi.org/10.1038/ncomms4974.

[82] Damewood L, Busemeyer B, Shaughnessy M, Fong CY, Yang LH, Felser C. Stabilizing and increasing the magnetic moment of half-metals: The role of Li in half-Heusler LiMnZ(Z=N, P, Si). Phys Rev B 2015;91:64409. https://doi.org/10.1103/PhysRevB.91.064409.

[83] Webster PJ, Ziebeck KRA, Town SL, Peak MS. Magnetic order and phase transformation in Ni2MnGa. Philos Mag B 1984;49:295–310. https://doi.org/10.1080/13642817408246515.

[84] Ullakko K, Huang JK, Kantner C, O'Handley RC, Kokorin VV. Large magnetic-field-induced strains in Ni_2MnGa single crystals. Appl Phys Lett 1996;69:1966–8. https://doi.org/10.1063/1.117637.

[85] Martynov VV, Kokorin VV. The crystal structure of thermally- and stress-induced Martensites in Ni_2MnGa single crystals. J Phys III Fr 1992;2:739–49.

[86] Sutou Y, Imano Y, Koeda N, Omori T, Kainuma R, Ishida K, et al. Magnetic and martensitic transformations of NiMnX(X=In, Sn, Sb) ferromagnetic shape memory alloys. Appl Phys Lett 2004;85:4358–60. https://doi.org/10.1063/1.1808879.

[87] de Oliveira NA, von Ranke PJ. Theoretical aspects of the magnetocaloric effect. Phys Rep 2010;489:89–159. https://doi.org/10.1016/j.physrep.2009.12.006.

[88] Mozharivskyj Molecular Sciences and Chemical Engineering YBT-RM in C. Magnetocaloric Effect and Magnetocaloric Materials, Elsevier; 2016. /10.1016/B978-0-12-409547-2.11643-9.

[89] Zimm C, Jastrab A, Sternberg A, Pecharsky V, Gschneidner K, Osborne M, et al. Description and Performance of a Near-Room Temperature Magnetic Refrigerator BT - Advances in Cryogenic Engineering. In: Kittel P, editor., Boston, MA: Springer US; 1998, p. 1759–66. 10.1007/978-1-4757-9047-4_222.

[90] Fähler S, Rößler UK, Kastner O, Eckert J, Eggeler G, Emmerich H, et al. Caloric Effects in Ferroic Materials: New Concepts for Cooling. Adv Eng Mater 2012;14:10–9. https://doi.org/10.1002/adem.201100178.

[91] Brück E, Tegus O, Cam Thanh DT, Trung NT, Buschow KHJ. A review on Mn based materials for magnetic refrigeration: Structure and properties. Int J Refrig 2008;31:763–70. https://doi.org/10.1016/j.ijrefrig.2007.11.013.

[92] Krenke T, Duman E, Acet M, Wassermann EF, Moya X, Mañosa L, et al. Inverse magnetocaloric effect in ferromagnetic Ni–Mn–Sn alloys. Nat Mater 2005;4:450–4. https://doi.org/10.1038/nmat1395.

[93] Krenke T, Duman E, Acet M, Wassermann EF, Moya X, Mañosa L, et al. Magnetic superelasticity and inverse magnetocaloric effect in Ni-Mn-In. Phys Rev B 2007;75:104414. https://doi.org/10.1103/PhysRevB.75.104414.

[94] Khan M, Ali N, Stadler S. Inverse magnetocaloric effect in ferromagnetic $Ni_{50}Mn_{37+x}Sb_{13-x}$ Heusler alloys. J Appl Phys 2007;101:53919. https://doi.org/10.1063/1.2710779.

[95] Khan M, Dubenko I, Stadler S, Ali N. Exchange bias in bulk Mn rich Ni–Mn–Sn Heusler alloys. J Appl Phys 2007;102:113914. https://doi.org/10.1063/1.2818016.

[96] Du J, Zheng Q, Ren WJ, Feng WJ, Liu XG, Zhang ZD. Magnetocaloric effect and magnetic-field-induced shape recovery effect at room temperature in ferromagnetic Heusler alloy Ni–Mn–Sb. J Phys D Appl Phys 2007;40:5523–6. https://doi.org/10.1088/0022-3727/40/18/001.

[97] Bourgault D, Tillier J, Courtois P, Maillard D, Chaud X. Large inverse magnetocaloric effect in $Ni_{45}Co_5Mn_{37.5}In_{12.5}$ single crystal above 300 K. Appl Phys Lett 2010;96:132501. doi: 10.1063/1.3372633.

[98] Liu J, Gottschall T, Skokov KP, Moore JD, Gutfleisch O. Giant magnetocaloric effect driven by structural transitions. Nat Mater 2012;11:620–6. https://doi.org/10.1038/nmat3334.

[99] Gottschall T, Skokov KP, Frincu B, Gutfleisch O. Large reversible magnetocaloric effect in Ni-Mn-In-Co. Appl Phys Lett 2015;106:21901. https://doi.org/10.1063/1.4905371.

[100] Mañosa L, González-Alonso D, Planes A, Bonnot E, Barrio M, Tamarit J-L, et al. Giant solid-state barocaloric effect in the Ni–Mn–In magnetic shape-memory alloy. Nat Mater 2010;9:478–81. https://doi.org/10.1038/nmat2731.

[101] Wei Z, Shen Y, Zhang Z, Guo J, Li B, Liu E, et al. Low-pressure-induced giant barocaloric effect in an all-d-metal Heusler $Ni_{35.5}Co_{14.5}Mn_{35}Ti_{15}$ magnetic shape memory alloy. APL Mater 2020;8:51101. doi: 10.1063/5.0005021.

[102] Yang Z, Cong DY, Huang L, Nie ZH, Sun XM, Zhang QH, et al. Large elastocaloric effect in a Ni–Co–Mn–Sn magnetic shape memory alloy. Mater Des 2016;92:932–6. https://doi.org/10.1016/j.matdes.2015.12.118.

[103] Cong D, Xiong W, Planes A, Ren Y, Mañosa L, Cao P, et al. Colossal Elastocaloric Effect in Ferroelastic Ni-Mn-Ti Alloys. Phys Rev Lett 2019;122:255703. https://doi.org/10.1103/PhysRevLett.122.255703.

[104] Qi X-L, Zhang S-C. The quantum spin Hall effect and topological insulators. Phys Today 2009;63:33–8. https://doi.org/10.1063/1.3293411.

[105] Qi X-L, Zhang S-C. Topological insulators and superconductors. Rev Mod Phys 2011;83:1057–110. https://doi.org/10.1103/RevModPhys.83.1057.

[106] Andrei BB, L. HT, Shou-Cheng Z. Quantum Spin Hall Effect and Topological Phase Transition in HgTe Quantum Wells. Science (80-) 2006;314:1757–61. doi: 10.1126/science.1133734.

[107] Markus K, Steffen W, Christoph B, Andreas R, Hartmut B, W. ML, et al. Quantum Spin Hall Insulator State in HgTe Quantum Wells. Science (80-) 2007;318:766–70. 10.1126/science.1148047.

[108] Hsieh D, Qian D, Wray L, Xia Y, Hor YS, Cava RJ, et al. A topological Dirac insulator in a quantum spin Hall phase. Nature 2008;452:970–4. https://doi.org/10.1038/nature06843.

[109] Müchler L, Zhang H, Chadov S, Yan B, Casper F, Kübler J, et al. Topological Insulators from a Chemist's Perspective. Angew Chemie Int Ed 2012;51:7221–5. https://doi.org/10.1002/anie.201202480.

[110] Chadov S, Qi X, Kübler J, Fecher GH, Felser C, Zhang SC. Tunable multifunctional topological insulators in ternary Heusler compounds. Nat Mater 2010;9:541–5. https://doi.org/10.1038/nmat2770.

[111] Zhang H-J, Chadov S, Müchler L, Yan B, Qi X-L, Kübler J, et al. Topological Insulators in Ternary Compounds with a Honeycomb Lattice. Phys Rev Lett 2011;106:156402. https://doi.org/10.1103/PhysRevLett.106.156402.

[112] Müchler L, Casper F, Yan B, Chadov S, Felser C. Topological insulators and thermoelectric materials. Phys Status Solidi – Rapid Res Lett 2013;7:91–100. https://doi.org/10.1002/pssr.201206411.

[113] Liu ZK, Yang LX, Wu S-C, Shekhar C, Jiang J, Yang HF, et al. Observation of unusual topological surface states in half-Heusler compounds LnPtBi (Ln=Lu, Y). Nat Commun 2016;7:12924. https://doi.org/10.1038/ncomms12924.

[114] Manna K, Sun Y, Muechler L, Kübler J, Felser C. Heusler. Weyl and Berry Nat Rev Mater 2018;3:244–56. https://doi.org/10.1038/s41578-018-0036-5.

[115] Kumar N, Guin SN, Manna K, Shekhar C, Felser C. Topological Quantum Materials from the Viewpoint of Chemistry. Chem Rev 2021;121:2780–815. https://doi.org/10.1021/acs.chemrev.0c00732.

[116] Yan B, Zhang S-C. Topological materials Reports Prog Phys 2012;75:96501. https://doi.org/10.1088/0034-4885/75/9/096501.

[117] Moore JE. The birth of topological insulators. Nature 2010;464:194–8. https://doi.org/10.1038/nature08916.

[118] Rogl G, Grytsiv A, Gürth M, Tavassoli A, Ebner C, Wünschek A, et al. Mechanical properties of half-Heusler alloys. Acta Mater 2016;107:178–95. https://doi.org/10.1016/j.actamat.2016.01.031.

[119] Everhart W, Newkirk J. Mechanical properties of Heusler alloys. Heliyon 2019;5. https://doi.org/10.1016/j.heliyon.2019.e01578.

[120] Huang X-M, Wang L-D, Liu H-X, Yan H-L, Jia N, Yang B, et al. Correlation between microstructure and martensitic transformation, mechanical properties and elastocaloric effect in Ni–Mn-based alloys. Intermetallics 2019;113:106579. https://doi.org/10.1016/j.intermet.2019.106579.

[121] Gràcia-Condal A, Gottschall T, Pfeuffer L, Gutfleisch O, Planes A, Mañosa L. Multicaloric effects in metamagnetic Heusler Ni-Mn-In under uniaxial stress and magnetic field. Appl Phys Rev 2020;7:41406. https://doi.org/10.1063/5.0020755.

[122] Yan H-L, Wang L-D, Liu H-X, Huang X-M, Jia N, Li Z-B, et al. Giant elastocaloric effect and exceptional mechanical properties in an all-d-metal Ni–Mn–Ti alloy: Experimental and ab-initio studies. Mater Des 2019;184:108180. https://doi.org/10.1016/j.matdes.2019.108180.

[123] Ritchie L, Xiao G, Ji Y, Chen TY, Chien CL, Zhang M, et al. Magnetic, structural, and transport properties of the Heusler alloys Co_2MnSi and NiMnSb. Phys Rev B 2003;68:104430. https://doi.org/10.1103/PhysRevB.68.104430.

[124] Nishino Y, Kato M, Asano S, Soda K, Hayasaki M, Mizutani U. Semiconductorlike Behavior of Electrical Resistivity in Heusler-type Fe_2VAl Compound. Phys Rev Lett 1997;79:1909–12. https://doi.org/10.1103/PhysRevLett.79.1909.

[125] Morcrette M, Larcher D, Tarascon JM, Edström K, Vaughey JT, Thackeray MM. Influence of electrode microstructure on the reactivity of Cu2Sb with lithium. Electrochim Acta 2007;52:5339–45. https://doi.org/10.1016/j.electacta.2007.01.083.

[126] Webster PJ, Ziebeck KRA. , in Alloys and Compounds of d-Elements with Main Group Elements. Part 2., e. In: Wijn HPJ, editor. Magn. Prop. Met. · Alloy. Compd. d-Elements with Main Gr. Elem. Part 2, Berlin: Springer-Verlag Berlin Heidelberg; n.d., p. 75–184. 10.1007/10353201_12.

[127] Graf T, Casper F, Winterlik J, Balke B, Fecher GH, Felser C. Crystal Structure of New Heusler Compounds. Zeitschrift Für Anorg Und Allg Chemie 2009;635:976–81. https://doi.org/10.1002/zaac.200900036.

[128] Gao GY, Yao K-L. Antiferromagnetic half-metals, gapless half-metals, and spin gapless semiconductors: The D03-type Heusler alloys. Appl Phys Lett 2013;103:232409. https://doi.org/10.1063/1.4840318.

[129] Chadov S, D'Souza SW, Wollmann L, Kiss J, Fecher GH, Felser C. Chemical disorder as an engineering tool for spin polarization in Mn_3Ga-based Heusler systems. Phys Rev B 2015;91:94203. https://doi.org/10.1103/PhysRevB.91.094203.

[130] Li J, Meng F, Liu G, Chen X, Hongzhi L, Liu E, et al. Electronic structure and magnetism of binary Fe-based half-Heusler alloys Fe_2Z (Z=In, Sn, Sb and As). J Magn Magn Mater 2013;331:82–7. 10.1016/j.jmmm.2012.11.038.

[131] Song J-T, Zhang J-M. The structural, electronic, magnetic and elastic properties of the binary Heusler alloys Mn_2Z (Z = As, Sb, Bi): a first-principles study. Mater Res Express 2017;4:116501. https://doi.org/10.1088/2053-1591/aa93cc.

[132] Slater JC. The Ferromagnetism of Nickel. II Temperature Effects Phys Rev 1936;49:931–7. https://doi.org/10.1103/PhysRev.49.931.

[133] Pauling L. The Nature of the Interatomic Forces in Metals. Phys Rev 1938;54:899–904. https://doi.org/10.1103/PhysRev.54.899.

[134] Néel ML. Propriétés magnétiques des ferrites; ferrimagnétisme et antiferromagnétisme. Ann Phys 1948;12:137–98.

[135] Hirohata A, Huminiuc T, Sinclair J, Wu H, Samiepour M, Vallejo-Fernandez G, et al. Development of antiferromagnetic Heusler alloys for the replacement of iridium as a critically raw material. J Phys D Appl Phys 2017;50:443001. https://doi.org/10.1088/1361-6463/aa88f4.

[136] Galanakis I, H. Dederichs P. Half-Metallicity and Slater-Pauling Behavior in the Ferromagnetic Heusler Alloys BT - Half-metallic Alloys: Fundamentals and Applications. In: Galanakis I, Dederichs PH, editors., Berlin, Heidelberg: Springer Berlin Heidelberg; 2005, p. 1–39. 10.1007/11506256_1.

[137] Kieven D, Klenk R, Naghavi S, Felser C, Gruhn T. I-II-V half-Heusler compounds for optoelectronics: Ab initio calculations. Phys Rev B 2010;81:75208. https://doi.org/10.1103/PhysRevB.81.075208.

[138] Roy A, Bennett JW, Rabe KM, Vanderbilt D. Half-Heusler Semiconductors as Piezoelectrics. Phys Rev Lett 2012;109:37602. https://doi.org/10.1103/PhysRevLett.109.037602.

[139] Ishida S, Fujii S, Kashiwagi S, Asano S. Search for Half-Metallic Compounds in Co_2MnZ (Z=IIIb, IVb, Vb Element). J Phys Soc Japan 1995;64:2152–7. https://doi.org/10.1143/JPSJ.64.2152.

[140] Fujii S, Sugimura S, Ishida AS. Hyperfine fields and electronic structures of the Heusler alloys Co_2MnX (X=Al, Ga, Si, Ge, Sn). J Phys Condens Matter 1990;2:8583–9. https://doi.org/10.1088/0953-8984/2/43/004.

[141] Fujii S, Ishida S, Asano S. A Half-Metallic Band Structure and Fe_2MnZ (Z=Al, Si, P). J Phys Soc Japan 1995;64:185–91. https://doi.org/10.1143/JPSJ.64.185.

[142] Kübler J, William AR, Sommers CB. Formation and coupling of magnetic moments in Heusler alloys. Phys Rev B 1983;28:1745–55. https://doi.org/10.1103/PhysRevB.28.1745.

[143] Li J, Jin Y. Half-metallicity of the inverse Heusler alloy $Mn_2CoAl(001)$ surface: A first-principles study. Appl Surf Sci 2013;283:876–80. /10.1016/j.apsusc.2013.07.036.

[144] Ahmadian F, Salary A. Half-metallicity in the Inverse Heusler compounds Sc_2MnZ (Z = C, Si, Ge, and Sn). Intermetallics 2014;46:243–9. 10.1016/j.intermet.2013.11.021.

[145] Wang XT, Lin TT, Rozale H, Dai XF, Liu GD. Robust half-metallic properties in inverse Heusler alloys composed of 4d transition metal elements: Zr2RhZ (Z=Al, Ga, In). J Magn Magn Mater 2016;402:190–5. https://doi.org/10.1016/j.jmmm.2015.11.062.

[146] Hirohata A, Kikuchi M, Tezuka N, Inomata K, Claydon JS, Xu YB, et al. Heusler alloy/semiconductor hybrid structures. Curr Opin Solid State Mater Sci 2006;10:93–107. https://doi.org/10.1016/j.cossms.2006.11.006.

[147] Takamura Y, Nakane R, Sugahara S. Quantitative analysis of atomic disorders in full-Heusler Co_2FeSi alloy thin films using x-ray diffraction with Co Kα and Cu Kα sources. J Appl Phys 2010;107:09B111. https://doi.org/10.1063/1.3350914.

[148] Shishidou T, Freeman AJ, Asahi R. Effect of GGA on the half-metallicity of the itinerant ferromagnet CoS_2. Phys Rev B 2001;64:180401. https://doi.org/10.1103/PhysRevB.64.180401.

[149] Kato H, Okuda T, Okimoto Y, Tomioka Y, Oikawa K, Kamiyama T, et al. Structural and electronic properties of the ordered double perovskites A2MReO6 (A = Sr, Ca; M =Mg, Sc, Cr, Mn, Fe Co, Ni, Zn). Phys Rev B 2004;69:184412. https://doi.org/10.1103/PhysRevB.69.184412.

[150] Joshi VK. Spintronics: A contemporary review of emerging electronics devices. Eng Sci Technol an Int J 2016;19:1503–13. https://doi.org/10.1016/j.jestch.2016.05.002.

[151] A. WS, D. AD, A. BR, M. DJ, S. von M, L. RM, et al. Spintronics: A Spin-Based Electronics Vision for the Future. Science (80-) 2001;294:1488–95. 10.1126/science.1065389.

[152] Yakout SM. Spintronics: Future Technology for New Data Storage and Communication Devices. J Supercond Nov Magn 2020;33:2557–80. https://doi.org/10.1007/s10948-020-05545-8.

[153] Wolf SA, Awschalom DD, Buhrman RA, Daughton JM, von Molnár S, Roukes ML, et al. Spintronics: A Spin-Based Electronics Vision for the Future. Science (80-) 2001;294:1488 LP – 1495. 10.1126/science.1065389.

[154] Grünberg P, Schreiber R, Pang Y, Brodsky MB, Sowers H. Layered Magnetic Structures: Evidence for Antiferromagnetic Coupling of Fe Layers across Cr Interlayers. Phys Rev Lett 1986;57:2442–5. https://doi.org/10.1103/PhysRevLett.57.2442.

[155] Baibich MN, Broto JM, Fert A, Van Dau FN, Petroff F, Etienne P, et al. Giant Magnetoresistance of (001)Fe/(001)Cr Magnetic Superlattices. Phys Rev Lett 1988;61:2472–5. https://doi.org/10.1103/PhysRevLett.61.2472.

[156] Thompson SM. The discovery, development and future of GMR: The Nobel Prize 2007. J Phys D Appl Phys 2008;41:93001. https://doi.org/10.1088/0022-3727/41/9/093001.

[157] Hirohata A, Yamada K, Nakatani Y, Prejbeanu I-L, Diény B, Pirro P, et al. Review on spintronics: Principles and device applications. J Magn Magn Mater 2020;509:166711. doi: 10.1016/j.jmmm.2020.166711.

[158] Nakatani TM, Furubayashi T, Kasai S, Sukegawa H, Takahashi YK, Mitani S, et al. Bulk and interfacial scatterings in current-perpendicular-to-plane giant magnetoresistance with $Co_2Fe(Al_{0.5}Si_{0.5})$ Heusler alloy layers and Ag spacer. Appl Phys Lett 2010;96:212501. 10.1063/1.3432070.

[159] Chen J, Liu J, Sakuraba Y, Sukegawa H, Li S, Hono K. Realization of high quality epitaxial current- perpendicular-to-plane giant magnetoresistive pseudo spin-valves on Si(001) wafer using NiAl buffer layer. APL Mater 2016;4:56104. https://doi.org/10.1063/1.4950827.

[160] Chen J, Furubayashi T, Takahashi YK, Sasaki TT, Hono K. Crystal orientation dependence of band matching in all-B2-trilayer current-perpendicular-to-plane giant magnetoresistance pseudo spin-valves using $Co_2Fe(Ge_{0.5}Ga_{0.5})$ Heusler alloy and NiAl spacer. J Appl Phys 2015;117:17C119. 10.1063/1.4915481.

[161] Chen J, Li S, Furubayashi T, Takahashi YK, Hono K. Crystal orientation dependence of current-perpendicular-to-plane giant magnetoresistance of pseudo spin-valves with epitaxial $Co_2Fe(Ge_{0.5}Ga_{0.5})$ Heusler alloy layers. J Appl Phys 2014;115:233905. 10.1063/1.4882736.

[162] Chen J, Sakuraba Y, Yakushiji K, Kurashima Y, Watanabe N, Liu J, et al. Fully epitaxial giant magnetoresistive devices with half-metallic Heusler alloy fabricated on poly-crystalline electrode using three-dimensional integration technology. Acta Mater 2020;200:1038–45. https://doi.org/10.1016/j.actamat.2020.04.002.

[163] Moyer JA, Mangalam RVK, Martin LW. 6 - Epitaxial growth of magnetic-oxide thin films. In: Koster G, Huijben M, Rijnders GBT-EG of CMO, editors. Woodhead Publ. Ser. Electron. Opt. Mater., Woodhead Publishing; 2015, p. 129–72. 10.1016/B978-1-78242-245-7.00006-3.

[164] Julliere M. Tunneling between ferromagnetic films. Phys Lett A 1975;54:225–6. https://doi.org/10.1016/0375-9601(75)90174-7.

[165] Maekawa S, Gafvert U. Electron tunneling between ferromagnetic films. IEEE Trans Magn 1982;18:707–8. https://doi.org/10.1109/TMAG.1982.1061834.

[166] Moodera JS, Kinder LR, Wong TM, Meservey R. Large Magnetoresistance at Room Temperature in Ferromagnetic Thin Film Tunnel Junctions. Phys Rev Lett 1995;74:3273–6. https://doi.org/10.1103/PhysRevLett.74.3273.

[167] Miyazaki T, Tezuka N. Giant magnetic tunneling effect in $Fe/Al_2O_3/Fe$ junction. J Magn Magn Mater 1995;139:L231–4. 10.1016/0304-8853(95)90001-2.

[168] Sakuraba Y, Hattori M, Oogane M, Ando Y, Kato H, Sakuma A, et al. Giant tunneling magnetoresistance in $Co_2MnSi/Al–O/Co_2MnSi$ magnetic tunnel junctions. Appl Phys Lett 2006;88:192508. https://doi.org/10.1063/1.2202724.

[169] Fert A, Van Dau FN. Spintronics, from giant magnetoresistance to magnetic skyrmions and topological insulators. Comptes Rendus Phys 2019;20:817–31. https://doi.org/10.1016/j.crhy.2019.05.020.

[170] Yuasa S, Nagahama T, Fukushima A, Suzuki Y, Ando K. Giant room-temperature magnetoresistance in single-crystal Fe/MgO/Fe magnetic tunnel junctions. Nat Mater 2004;3:868–71. https://doi.org/10.1038/nmat1257.

[171] Parkin SSP, Kaiser C, Panchula A, Rice PM, Hughes B, Samant M, et al. Giant tunnelling magnetoresistance at room temperature with MgO (100) tunnel barriers. Nat Mater 2004;3:862–7. https://doi.org/10.1038/nmat1256.

[172] Ikeda S, Hayakawa J, Ashizawa Y, Lee YM, Miura K, Hasegawa H, et al. Tunnel magnetoresistance of 604% at 300K by suppression of Ta diffusion in CoFeB/MgO/CoFeB pseudo-spin-valves annealed at high temperature. Appl Phys Lett 2008;93:82508. https://doi.org/10.1063/1.2976435.

[173] Gallagher W, Parkin S. Development of the magnetic tunnel junction MRAM at IBM: From first junctions to a 16-Mb MRAM demonstrator chip. IBM J Res Dev 2006;50:5–23. https://doi.org/10.1147/rd.501.0005.

[174] LeClair P, Ha JK, Swagten HJM, Kohlhepp JT, van de Vin CH, de Jonge WJM. Large magnetoresistance using hybrid spin filter devices. Appl Phys Lett 2002;80:625–7. https://doi.org/10.1063/1.1436284.

[175] Bowen M, Bibes M, Barthélémy A, Contour J-P, Anane A, Lemaître Y, et al. Nearly total spin polarization in $La_{2/3}Sr_{1/3}MnO_3$ from tunneling experiments. Appl Phys Lett 2003;82:233–5. 10.1063/1.1534619.

[176] Ishikawa T, Marukame T, Kijima H, Matsuda K-I, Uemura T, Arita M, et al. Spin-dependent tunneling characteristics of fully epitaxial magnetic tunneling junctions with a full-Heusler alloy Co_2MnSi thin film and a MgO tunnel barrier. Appl Phys Lett 2006;89:192505. https://doi.org/10.1063/1.2378397.

[177] Felser C, Fecher GH, Balke B. Spintronics: A Challenge for Materials Science and Solid-State Chemistry. Angew Chemie Int Ed 2007;46:668–99. https://doi.org/10.1002/anie.200601815.

[178] Hülsen B, Scheffler M, Kratzer P. Thermodynamics of the Heusler alloy $Co_{2-x}Mn_{1+x}Si$: A combined density functional theory and cluster expansion study. Phys Rev B 2009;79:94407. https://doi.org/10.1103/PhysRevB.79.094407.

[179] Wang W, Liu E, Kodzuka M, Sukegawa H, Wojcik M, Jedryka E, et al. Coherent tunneling and giant tunneling magnetoresistance in $Co_2FeAl/MgO/CoFe$ magnetic tunneling junctions. Phys Rev B 2010;81:140402. https://doi.org/10.1103/PhysRevB.81.140402.

[180] Inomata K, Ikeda N, Tezuka N, Goto R, Sugimoto S, Wojcik M, et al. Highly spin-polarized materials and devices for spintronics*. Sci Technol Adv Mater 2008;9:14101. https://doi.org/10.1088/1468-6996/9/1/014101.

[181] Wang W, Sukegawa H, Shan R, Mitani S, Inomata K. Giant tunneling magnetoresistance up to 330% at room temperature in sputter deposited $Co_2FeAl/MgO/CoFe$ magnetic tunnel junctions. Appl Phys Lett 2009;95:182502. https://doi.org/10.1063/1.3258069.

[182] Liu H, Honda Y, Taira T, Matsuda K, Arita M, Uemura T, et al. Giant tunneling magnetoresistance in epitaxial $Co_2MnSi/MgO/Co_2MnSi$ magnetic tunnel junctions by half-metallicity of Co_2MnSi and coherent tunneling. Appl Phys Lett 2012;101:132418. https://doi.org/10.1063/1.4755773.

[183] Kabanov YP, Shull RD, Zheng C, Pong PWT, Gopman DB. Asymmetric magnetization reversal of the Heusler alloy Co_2FeSi as free layer in an CoFeB/MgO/Co2FeSi magnetic tunnel junction. Appl Surf Sci 2021;536. https://doi.org/10.1016/j.apsusc.2020.147672.

[184] Trudel S, Gaier O, Hamrle J, Hillebrands B. Magnetic anisotropy, exchange and damping in cobalt-based full-Heusler compounds: an experimental review. J Phys D Appl Phys 2010;43:193001. https://doi.org/10.1088/0022-3727/43/19/193001.

[185] Sterwerf C, Paul S, Khodadadi B, Meinert M, Schmalhorst J-M, Buchmeier M, et al. Low Gilbert damping in Co_2FeSi and Fe_2CoSi films. J Appl Phys 2016;120:83904. https://doi.org/10.1063/1.4960705.

[186] Gaier O, Hamrle J, Trudel S, Hillebrands B, Schneider H, Jakob G. Exchange stiffness in the Co_2FeSi Heusler compound. J Phys D Appl Phys 2009;42:232001. https://doi.org/10.1088/0022-3727/42/23/232001.

[187] Hirohata A, Lloyd DC. Heusler alloys for metal spintronics. MRS Bull 2022. https://doi.org/10.1557/s43577-022-00350-1.

[188] Wei ZY, Liu EK, Chen JH, Li Y, Liu GD, Luo HZ, et al. Realization of multifunctional shape-memory ferromagnets in all-d-metal Heusler phases. Appl Phys Lett 2015;107:22406. https://doi.org/10.1063/1.4927058.

[189] Roy S, Blackburn E, Valvidares SM, Fitzsimmons MR, Vogel SC, Khan M, et al. Delocalization and hybridization enhance the magnetocaloric effect in Cu-doped Ni_2MnGa. Phys Rev B 2009;79:235127. https://doi.org/10.1103/PhysRevB.79.235127.

[190] Muldawer L. X-ray Study of Ternary Ordering of the Noble Metals in AgAuZn2 and $CuAuZn_2$. J Appl Phys 1966;37:2062–6. https://doi.org/10.1063/1.1708670.

[191] Murakami Y, Watanabe Y, Kachi S. An X-ray Study of the Heusler-type Ordering in $AuAgZn_2$ Alloy. Trans Japan Inst Met 1980;21:708–13. https://doi.org/10.2320/matertrans1960.21.708.

[192] Wei ZY, Liu EK, Li Y, Han XL, Du ZW, Luo HZ, et al. Magnetostructural martensitic transformations with large volume changes and magneto-strains in all-d-metal Heusler alloys. Appl Phys Lett 2016;109:71904. https://doi.org/10.1063/1.4961382.

[193] Han Y, Wu M, Kuang M, Yang T, Chen X, Wang X. All-d-metal equiatomic quaternary Heusler hypothetical alloys ZnCdTMn (T = Fe, Ru, Os, Rh, Ir, Ni, Pd, Pt): A first-principle investigation of electronic structures, magnetism, and possible martensitic transformations. Results Phys 2018;11:1134–41. https://doi.org/10.1016/j.rinp.2018.11.024.

[194] Zeng Q, Shen J, Zhang H, Chen J, Ding B, Xi X, et al. Electronic behaviors during martensitic transformations in all-*d*-metal Heusler alloys. J Phys Condens Matter 2019;31:425401. https://doi.org/10.1088/1361-648x/ab2bd8.

[195] Taubel A, Beckmann B, Pfeuffer L, Fortunato N, Scheibel F, Ener S, et al. Tailoring magnetocaloric effect in all-d-metal Ni-Co-Mn-Ti Heusler alloys: a combined experimental and theoretical study. Acta Mater 2020;201:425–34. https://doi.org/10.1016/j.actamat.2020.10.013.

[196] Li Y, Qin L, Huang S, Li L. Enhanced magnetocaloric performances and tunable martensitic transformation in $Ni_{35}Co_{15}Mn_{35-x}Fe_xTi_{15}$ all-d-metal Heusler alloys by chemical and physical pressures. Sci China Mater 2022;65:486–93. https://doi.org/10.1007/s40843-021-1747-3.

[197] Korenko MK, Cohen M. Some martensitic embryo experiments using high magnetic fields. Scr Metall 1974;8:751–4. https://doi.org/10.1016/0036-9748(74)90287-7.

[198] James RD, Wuttig M. Magnetostriction of martensite Philos Mag A 1998;77:1273–99. https://doi.org/10.1080/01418619808214252.

[199] Vasil'ev AN, Kokorin V V., I YS, Chernenko VA. The Magnetoelastic Properties of a Ni_2MnGa Single Crystal. Sov Phys JETP 1990;71:1437–41.

[200] Chernenko VA, Cesari E, Kokorin VV, Vitenko IN. The development of new ferromagnetic shape memory alloys in Ni-Mn-Ga system. Scr Metall Mater 1995;33:1239–44. https://doi.org/10.1016/0956-716X(95)00370-B.

[201] Entel P, Buchelnikov VD, Khovailo VV, Zayak AT, Adeagbo WA, Gruner ME, et al. Modelling the phase diagram of magnetic shape memory Heusler alloys. J Phys D Appl Phys 2006;39:865–89. https://doi.org/10.1088/0022-3727/39/5/s13.

[202] Murray SJ, Marioni M, Allen SM, O'Handley RC, Lograsso TA. 6% magnetic-field-induced strain by twin-boundary motion in ferromagnetic Ni–Mn–Ga. Appl Phys Lett 2000;77:886–8. https://doi.org/10.1063/1.1306635.

[203] Sozinov A, Likhachev AA, Lanska N, Ullakko K. Giant magnetic-field-induced strain in NiMnGa seven-layered martensitic phase. Appl Phys Lett 2002;80:1746–8. https://doi.org/10.1063/1.1458075.

[204] Siewert M, Gruner ME, Dannenberg A, Chakrabarti A, Herper HC, Wuttig M, et al. Designing shape-memory Heusler alloys from first-principles. Appl Phys Lett 2011;99:191904. https://doi.org/10.1063/1.3655905.

[205] Planes A, Mañosa L, Acet M. Magnetocaloric effect and its relation to shape-memory properties in ferromagnetic Heusler alloys. J Phys Condens Matter 2009;21:233201. https://doi.org/10.1088/0953-8984/21/23/233201.

[206] Bruno NM, Karaman I, Ross JH, Chumlyakov YI. High-field magneto-thermo-mechanical testing system for characterizing multiferroic bulk alloys. Rev Sci Instrum 2015;86:113902. https://doi.org/10.1063/1.4934571.

[207] Gottschall T, Gràcia-Condal A, Fries M, Taubel A, Pfeuffer L, Mañosa L, et al. A multicaloric cooling cycle that exploits thermal hysteresis. Nat Mater 2018;17:929–34. https://doi.org/10.1038/s41563-018-0166-6.

[208] Stern-Taulats E, Castán T, Mañosa L, Planes A, Mathur ND, Moya X. Multicaloric materials and effects. MRS Bull 2018;43:295–9. https://doi.org/10.1557/mrs.2018.72.

[209] Thomson II W. On the thermoelastic, thermomagnetic, and pyroelectric properties of matter. London, Edinburgh, Dublin Philos Mag J Sci 1878;5:4–27. https://doi.org/10.1080/14786447808639378.

[210] Warburg E. Magnetische Untersuchungen. Ann Phys 1881;249:141–64. https://doi.org/10.1002/andp.18812490510.

[211] Weiss P, Piccard A. Le phénomène magnétocalorique. J Phys Théorique Appliquée 1917;7:103–9. https://doi.org/10.1051/jphystap:019170070010300.

[212] Giauque WF, MacDougall DP. Attainment of Temperatures Below 1° Absolute by Demagnetization of $Gd_2(SO_4)_3{\cdot}8H2O$. Phys Rev 1933;43:768. https://doi.org/10.1103/PhysRev.43.768.

[213] Brown GV. Magnetic heat pumping near room temperature. J Appl Phys 1976;47:3673–80. https://doi.org/10.1063/1.323176.

[214] Pecharsky VK, Gschneidner KAJ. Giant Magnetocaloric Effect in $Gd_5(Si_2Ge_2)$. Phys Rev Lett 1997;78:4494–7. https://doi.org/10.1103/PhysRevLett.78.4494.

[215] Franco V, Blázquez JS, Ipus JJ, Law JY, Moreno-Ramírez LM, Conde A. Magnetocaloric effect: From materials research to refrigeration devices. Prog Mater Sci 2018;93:112–232. https://doi.org/10.1016/j.pmatsci.2017.10.005.

[216] Tishin AM. The magnetocaloric effect and its applications. Philadelphia: Institute Of Physics Pub; 2003.

[217] GschneidnerJr KA, Pecharsky VK, Tsokol AO. Recent developments in magnetocaloric materials. Reports Prog Phys 2005;68:1479–539. https://doi.org/10.1088/0034-4885/68/6/r04.

[218] Pecharsky VK, Gschneidner KA. Tunable magnetic regenerator alloys with a giant magnetocaloric effect for magnetic refrigeration from ~20 to ~290 K. Appl Phys Lett 1997;70:3299–301. https://doi.org/10.1063/1.119206.

[219] Guo ZB, Du YW, Zhu JS, Huang H, Ding WP, Feng D. Large Magnetic Entropy Change in Perovskite-Type Manganese Oxides. Phys Rev Lett 1997;78:1142–5. https://doi.org/10.1103/PhysRevLett.78.1142.

[220] Morellon L, Magen C, Algarabel PA, Ibarra MR, Ritter C. Magnetocaloric effect in $Tb_5(Si_xGe_{1-x})_4$. Appl Phys Lett 2001;79:1318–20. https://doi.org/10.1063/1.1399007.

[221] Wada H, Tanabe Y. Giant magnetocaloric effect of $MnAs_{1-x}Sb_x$. Appl Phys Lett 2001;79:3302–4. https://doi.org/10.1063/1.1419048.

[222] Tegus O, Brück E, Buschow KHJ, de Boer FR. Transition-metal-based magnetic refrigerants for room-temperature applications. Nature 2002;415:150–2. https://doi.org/10.1038/415150a.

[223] Annaorazov MP, Asatryan KA, Myalikgulyev G, Nikitin SA, Tishin AM, Tyurin AL. Alloys of the FeRh system as a new class of working material for magnetic refrigerators. Cryogenics (Guildf) 1992;32:867–72. https://doi.org/10.1016/0011-2275(92)90352-B.

[224] Sandeman KG, Takei S. Magnetocaloric Materials and Applications BT - Handbook of Magnetism and Magnetic Materials. In: Coey M, Parkin S, editors., Cham: Springer International Publishing; 2020, p. 1–38. 10.1007/978-3-030-63101-7_13-1.

[225] Koyama K, Okada H, Watanabe K, Kanomata T, Kainuma R, Ito W, et al. Observation of large magnetoresistance of magnetic Heusler alloy $Ni_{50}Mn_{36}Sn_{14}$ in high magnetic fields. Appl Phys Lett 2006;89:182510. https://doi.org/10.1063/1.2374868.

[226] Pasquale M, Sasso CP, Lewis LH, Giudici L, Lograsso T, Schlagel D. Magnetostructural transition and magnetocaloric effect in $Ni_{55}Mn_{20}Ga_{25}$ single crystals. Phys Rev B 2005;72:94435. https://doi.org/10.1103/PhysRevB.72.094435.

[227] Liu J, Moore JD, Skokov KP, Krautz M, Löwe K, Barcza A, et al. Exploring La(Fe, Si)13-based magnetic refrigerants towards application. Scr Mater 2012;67:584–9. https://doi.org/10.1016/j.scriptamat.2012.05.039.

[228] Mañosa L, Planes A. Materials with Giant Mechanocaloric Effects: Cooling by Strength. Adv Mater 2017;29:1603607. https://doi.org/10.1002/adma.201603607.

[229] Bonnot E, Romero R, Mañosa L, Vives E, Planes A. Elastocaloric Effect Associated with the Martensitic Transition in Shape-Memory Alloys. Phys Rev Lett 2008;100:125901. https://doi.org/10.1103/PhysRevLett.100.125901.

[230] Cazorla C. Novel mechanocaloric materials for solid-state cooling applications. Appl Phys Rev 2019;6:41316. https://doi.org/10.1063/1.5113620.

[231] Mañosa L, Planes A. Mechanocaloric effects in shape memory alloys. Philos Trans R Soc A Math Phys Eng Sci 2016;374:20150310. https://doi.org/10.1098/rsta.2015.0310.

[232] Mañosa L, Moya X, Planes A, Gutfleisch O, Lyubina J, Barrio M, et al. Effects of hydrostatic pressure on the magnetism and martensitic transition of Ni–Mn–In magnetic superelastic alloys. Appl Phys Lett 2008;92:12515. https://doi.org/10.1063/1.2830999.

[233] Stern-Taulats E, Planes A, Lloveras P, Barrio M, Tamarit J-L, Pramanick S, et al. Tailoring barocaloric and magnetocaloric properties in low-hysteresis magnetic shape memory alloys. Acta Mater 2015;96:324–32. https://doi.org/10.1016/j.actamat.2015.06.026.

[234] Aznar A, Gràcia-Condal A, Planes A, Lloveras P, Barrio M, Tamarit J-L, et al. Giant barocaloric effect in all- d-metal Heusler shape memory alloys. Phys Rev Mater 2019;3:44406. https://doi.org/10.1103/PhysRevMaterials.3.044406.

[235] Stern-Taulats E, Lloveras P, Barrio M, Defay E, Egilmez M, Planes A, et al. Inverse barocaloric effects in ferroelectric $BaTiO_3$ ceramics. APL Mater 2016;4:91102. https://doi.org/10.1063/1.4961598.

[236] Liu Y, Wei J, Janolin P-E, Infante IC, Lou X, Dkhil B. Giant room-temperature barocaloric effect and pressure-mediated electrocaloric effect in $BaTiO_3$ single crystal. Appl Phys Lett 2014;104:162904. https://doi.org/10.1063/1.4873162.
[237] Lloveras P, Stern-Taulats E, Barrio M, Tamarit J-L, Crossley S, Li W, et al. Giant barocaloric effects at low pressure in ferrielectric ammonium sulphate. Nat Commun 2015;6:8801. https://doi.org/10.1038/ncomms9801.
[238] Bermúdez-García JM, Sánchez-Andújar M, Castro-García S, López-Beceiro J, Artiaga R, Señarís-Rodríguez MA. Giant barocaloric effect in the ferroic organic-inorganic hybrid [TPrA, Mn(dca)$_3$] perovskite under easily accessible pressures. Nat Commun 2017;8:15715. https://doi.org/10.1038/ncomms15715.
[239] Flerov IN, Kartashev A V, Gorev M V, Bogdanov E V, Mel'nikova S V, Molokeev MS, et al. Thermal, structural, optical, dielectric and barocaloric properties at ferroelastic phase transition in trigonal $(NH_4)_2SnF_6$: A new look at the old compound. J Fluor Chem 2016;183:1–9. 10.1016/j.jfluchem.2015.12.010.
[240] Gorev M V, Bogdanov E V, Flerov IN. Conventional and inverse barocaloric effects around triple points in ferroelastics $(NH_4)_3NbOF_6$ and $(NH_4)_3TiOF_5$. Scr Mater 2017;139:53–7. 10.1016/j.scriptamat.2017.06.022.
[241] Usuda EO, Bom NM, Carvalho AMG. Large barocaloric effects at low pressures in natural rubber. Eur Polym J 2017;92:287–93. https://doi.org/10.1016/j.eurpolymj.2017.05.017.
[242] Bom NM, Imamura W, Usuda EO, Paixão LS, Carvalho AMG. Giant Barocaloric Effects in Natural Rubber: A Relevant Step toward Solid-State Cooling. ACS Macro Lett 2018;7:31–6. https://doi.org/10.1021/acsmacrolett.7b00744.
[243] Carvalho AMG, Imamura W, Usuda EO, Bom NM. Giant room-temperature barocaloric effects in PDMS rubber at low pressures. Eur Polym J 2018;99:212–21. https://doi.org/10.1016/j.eurpolymj.2017.12.007.
[244] Miliante CM, Christmann AM, Usuda EO, Imamura W, Paixão LS, Carvalho AMG, et al. Unveiling the Origin of the Giant Barocaloric Effect in Natural Rubber. Macromolecules 2020;53:2606–15. https://doi.org/10.1021/acs.macromol.0c00051.
[245] Odaira T, Xu S, Xu X, Omori T, Kainuma R. Elastocaloric switching effect induced by reentrant martensitic transformation. Appl Phys Rev 2020;7:31406. https://doi.org/10.1063/5.0007753.
[246] Gschneidner KA, Mudryk Y, Pecharsky VK. On the nature of the magnetocaloric effect of the first-order magnetostructural transition. Scr Mater 2012;67:572–7. https://doi.org/10.1016/j.scriptamat.2011.12.042.
[247] Tušek J, Engelbrecht K, Millán-Solsona R, Mañosa L, Vives E, Mikkelsen LP, et al. The Elastocaloric Effect: A Way to Cool Efficiently. Adv Energy Mater 2015;5:1500361. https://doi.org/10.1002/aenm.201500361.
[248] Tušek J, Engelbrecht K, Eriksen D, Dall'Olio S, Tušek J, Pryds N. A regenerative elastocaloric heat pump. Nat Energy 2016;1:16134. 10.1038/nenergy.2016.134.
[249] Xu S, Huang H-Y, Xie J, Takekawa S, Xu X, Omori T, et al. Giant elastocaloric effect covering wide temperature range in columnar-grained $Cu_{71.5}Al_{17.5}Mn_{11}$ shape memory alloy. APL Mater 2016;4:106106. 10.1063/1.4964621.
[250] Cui J, Wu Y, Muehlbauer J, Hwang Y, Radermacher R, Fackler S, et al. Demonstration of high efficiency elastocaloric cooling with large ΔT using NiTi wires. Appl Phys Lett 2012;101:73904. https://doi.org/10.1063/1.4746257.
[251] Álvarez-Alonso P, Aguilar-Ortiz CO, Villa E, Nespoli A, Flores-Zúñiga H, Chernenko VA. Conventional and inverse elastocaloric effect in Ni-Fe-Ga and Ni-Mn-Sn ribbons. Scr Mater 2017;128:36–40. https://doi.org/10.1016/j.scriptamat.2016.09.033.
[252] Liang X, Xiao F, Jin M, Jin X, Fukuda T, Kakeshita T. Elastocaloric effect induced by the rubber-like behavior of nanocrystalline wires of a Ti-50.8Ni (at.%) alloy. Scr Mater 2017;134:42–6. https://doi.org/10.1016/j.scriptamat.2017.02.026.
[253] Huang YJ, Hu QD, Bruno NM, Chen J-H, Karaman I, Ross JH, et al. Giant elastocaloric effect in directionally solidified Ni–Mn–In magnetic shape memory alloy. Scr Mater 2015;105:42–5. https://doi.org/10.1016/j.scriptamat.2015.04.024.
[254] Ossmer H, Lambrecht F, Gültig M, Chluba C, Quandt E, Kohl M. Evolution of temperature profiles in TiNi films for elastocaloric cooling. Acta Mater 2014;81:9–20. https://doi.org/10.1016/j.actamat.2014.08.006.
[255] Pataky GJ, Ertekin E, Sehitoglu H. Elastocaloric cooling potential of NiTi, Ni_2FeGa, and CoNiAl. Acta Mater 2015;96:420–7. 10.1016/j.actamat.2015.06.011.
[256] Yang Z, Cong DY, Sun XM, Nie ZH, Wang YD. Enhanced cyclability of elastocaloric effect in boron-microalloyed Ni-Mn-In magnetic shape memory alloys. Acta Mater 2017;127:33–42. https://doi.org/10.1016/j.actamat.2017.01.025.
[257] Wei ZY, Sun W, Shen Q, Shen Y, Zhang YF, Liu EK, et al. Elastocaloric effect of all-d-metal Heusler NiMnTi(Co) magnetic shape memory alloys by digital image correlation and infrared thermography. Appl Phys Lett 2019;114:101903. https://doi.org/10.1063/1.5077076.
[258] Shen Y, Wei Z, Sun W, Zhang Y, Liu E, Liu J. Large elastocaloric effect in directionally solidified all-d-metal Heusler metamagnetic shape memory alloys. Acta Mater 2020;188:677–85. https://doi.org/10.1016/j.actamat.2020.02.045.
[259] Czernuszewicz A, Kaleta J, Lewandowski D. Multicaloric effect: Toward a breakthrough in cooling technology. Energy Convers Manag 2018;178:335–42. https://doi.org/10.1016/j.enconman.2018.10.025.
[260] de Oliveira NA. Entropy change upon magnetic field and pressure variations. Appl Phys Lett 2007;90:52501. https://doi.org/10.1063/1.2434154.
[261] Lin H, Wray LA, Xia Y, Xu S, Jia S, Cava RJ, et al. Half-Heusler ternary compounds as new multifunctional experimental platforms for topological quantum phenomena. Nat Mater 2010;9:546–9. https://doi.org/10.1038/nmat2771.
[262] Hasan MZ, Kane CL. Colloquium: Topological insulators. Rev Mod Phys 2010;82:3045–67. https://doi.org/10.1103/RevModPhys.82.3045.
[263] König M, Wiedmann S, Brüne C, Roth A, Buhmann H, Molenkamp LW, et al. Quantum Spin Hall Insulator State in HgTe Quantum Wells. Science (80-) 2007;318:766 LP – 770. 10.1126/science.1148047.
[264] Dai X, Hughes TL, Qi X-L, Fang Z, Zhang S-C. Helical edge and surface states in HgTe quantum wells and bulk insulators. Phys Rev B 2008;77:125319. https://doi.org/10.1103/PhysRevB.77.125319.
[265] Zhang H, Liu C-X, Qi X-L, Dai X, Fang Z, Zhang S-C. Topological insulators in Bi_2Se_3, Bi_2Te_3 and Sb_2Te_3 with a single Dirac cone on the surface. Nat Phys 2009;5:438–42. https://doi.org/10.1038/nphys1270.
[266] Xia Y, Qian D, Hsieh D, Wray L, Pal A, Lin H, et al. Observation of a large-gap topological-insulator class with a single Dirac cone on the surface. Nat Phys 2009;5:398–402. https://doi.org/10.1038/nphys1274.
[267] Chen YL, Analytis JG, Chu J-H, Liu ZK, Mo S-K, Qi XL, et al. Experimental Realization of a Three-Dimensional Topological Insulator, Bi2Te3. Science (80-) 2009;325:178–81. https://doi.org/10.1126/science.1173034.
[268] Yan B, de Visser A. Half-Heusler topological insulators. MRS Bull 2014;39:859–66. https://doi.org/10.1557/mrs.2014.198.
[269] He R, Gahlawat S, Guo C, Chen S, Dahal T, Zhang H, et al. Studies on mechanical properties of thermoelectric materials by nanoindentation. Phys Status Solidi 2015;212:2191–5. https://doi.org/10.1002/pssa.201532045.
[270] Yousuf S, Gupta DC. Thermoelectric and mechanical properties of gapless Zr_2MnAl compound. Indian J Phys 2017;91:33–41. https://doi.org/10.1007/s12648-016-0900-3.
[271] Musabirov II, Safarov IM, Nagimov MI, Sharipov IZ, Koledov VV, Mashirov AV, et al. Fine-grained structure and properties of a Ni2MnIn alloy after a settling plastic deformation. Phys Solid State 2016;58:1605–10. https://doi.org/10.1134/S1063783416080217.
[272] Wen Z, Zhao Y, Hou H, Wang B, Han P. The mechanical and thermodynamic properties of Heusler compounds Ni_2XAl (X=Sc, Ti, V) under pressure and temperature: A first-principles study. Mater Des 2017;114:398–403. 10.1016/j.matdes.2016.11.005.
[273] Yang Z, Cong D, Yuan Y, Wu Y, Nie Z, Li R, et al. Ultrahigh cyclability of a large elastocaloric effect in multiferroic phase-transforming materials. Mater Res Lett 2019;7:137–44. https://doi.org/10.1080/21663831.2019.1566182.
[274] Tang X, Feng Y, Wang H, Wang P. Enhanced elastocaloric effect and cycle stability in B and Cu co-doping Ni-Mn-In polycrystals. Appl Phys Lett 2019;114:33901. https://doi.org/10.1063/1.5080762.
[275] Jiao ZB, Luan JH, Liu CT. Strategies for improving ductility of ordered intermetallics. Prog Nat Sci Mater Int 2016;26:1–12. https://doi.org/10.1016/j.pnsc.2016.01.014.
[276] Mañosa L, Planes A, Acet M. Advanced materials for solid-state refrigeration. J Mater Chem A 2013;1:4925–36. https://doi.org/10.1039/C3TA01289A.
[277] Li Y, Yang K. High-throughput computational design of organic–inorganic hybrid halide semiconductors beyond perovskites for optoelectronics. Energy Environ Sci 2019;12:2233–43. https://doi.org/10.1039/C9EE01371G.

[278] Li Y, Maldonado-Lopez D, Ríos Vargas V, Zhang J, Yang K. Stability diagrams, defect tolerance, and absorption coefficients of hybrid halide semiconductors: High-throughput first-principles characterization. J Chem Phys 2020;152:84106. https://doi.org/10.1063/1.5127929.
[279] Li Y, Yang K. High-throughput computational design of halide perovskites and beyond for optoelectronics. Wires Comput Mol Sci 2021;11:e1500. 10.1002/wcms.1500.
[280] Yang K, Nazir S, Behtash M, Cheng J. High-Throughput Design of Two-Dimensional Electron Gas Systems Based on Polar/Nonpolar Perovskite Oxide Heterostructures. Sci Rep 2016;6:34667. https://doi.org/10.1038/srep34667.
[281] Cheng J, Yang K. Design of two-dimensional electron gas systems via polarization discontinuity from large-scale first-principles calculations. J Mater Chem C 2018;6:6680–90. https://doi.org/10.1039/C8TC01893F.
[282] Yang K, Setyawan W, Wang S, Buongiorno Nardelli M, Curtarolo S. A search model for topological insulators with high-throughput robustness descriptors. Nat Mater 2012;11:614–9. https://doi.org/10.1038/nmat3332.
[283] Hautier G, Jain A, Chen H, Moore C, Ong SP, Ceder G. Novel mixed polyanions lithium-ion battery cathode materials predicted by high-throughput ab initio computations. J Mater Chem 2011;21:17147–53. https://doi.org/10.1039/C1JM12216A.
[284] Hautier G, Jain A, Ong SP, Kang B, Moore C, Doe R, et al. Phosphates as Lithium-Ion Battery Cathodes: An Evaluation Based on High-Throughput ab Initio Calculations. Chem Mater 2011;23:3495–508. https://doi.org/10.1021/cm200949v.
[285] Ong SP, Chevrier VL, Hautier G, Jain A, Moore C, Kim S, et al. Voltage, stability and diffusion barrier differences between sodium-ion and lithium-ion intercalation materials. Energy Environ Sci 2011;4:3680–8. https://doi.org/10.1039/C1EE01782A.
[286] Carrete J, Li W, Mingo N, Wang S, Curtarolo S. Finding Unprecedentedly Low-Thermal-Conductivity Half-Heusler Semiconductors via High-Throughput Materials Modeling. Phys Rev X 2014;4:11019. https://doi.org/10.1103/PhysRevX.4.011019.
[287] Bhattacharya S, Madsen GKH. A novel p-type half-Heusler from high-throughput transport and defect calculations. J Mater Chem C 2016;4:11261–8. https://doi.org/10.1039/C6TC04259G.
[288] Oliynyk AO, Antono E, Sparks TD, Ghadbeigi L, Gaultois MW, Meredig B, et al. High-Throughput Machine-Learning-Driven Synthesis of Full-Heusler Compounds. Chem Mater 2016;28:7324–31. https://doi.org/10.1021/acs.chemmater.6b02724.
[289] Balluff J, Diekmann K, Reiss G, Meinert M. High-throughput screening for antiferromagnetic Heusler compounds using density functional theory. Phys Rev Mater 2017;1:34404. https://doi.org/10.1103/PhysRevMaterials.1.034404.
[290] Kim K, Ward L, He J, Krishna A, Agrawal A, Wolverton C. Machine-learning-accelerated high-throughput materials screening: Discovery of novel quaternary Heusler compounds. Phys Rev Mater 2018;2:123801. https://doi.org/10.1103/PhysRevMaterials.2.123801.
[291] Sanvito S, Žic M, Nelson J, Archer T, Oses C, Curtarolo S. Machine Learning and High-Throughput Approaches to Magnetism BT - Handbook of Materials Modeling: Applications: Current and Emerging Materials. In: Andreoni W, Yip S, editors., Cham: Springer International Publishing; 2018, p. 1–23. 10.1007/978-3-319-50257-1_108-1.
[292] Ahmad R, Gul A, Mehmood N. Artificial neural networks and vector regression models for prediction of lattice constants of half-Heusler compounds. Mater Res Express 2019;6:46517. https://doi.org/10.1088/2053-1591/aafa9f.
[293] Barreteau C, Crivello J-C, Joubert J-M, Alleno E. Looking for new thermoelectric materials among TMX intermetallics using high-throughput calculations. Comput Mater Sci 2019;156:96–103. https://doi.org/10.1016/j.commatsci.2018.09.030.
[294] Gao Q, Opahle I, Zhang H. High-throughput screening for spin-gapless semiconductors in quaternary Heusler compounds. Phys Rev Mater 2019;3:24410. https://doi.org/10.1103/PhysRevMaterials.3.024410.
[295] Guo S, Jia T, Zhang Y. Electrical Property Dominated Promising Half-Heusler Thermoelectrics through High-Throughput Material Computations. J Phys Chem C 2019;123:18824–33. https://doi.org/10.1021/acs.jpcc.9b04580.
[296] Han Y, Chen Z, Kuang M, Liu Z, Wang X, Wang X. 171 Scandium-based full Heusler compounds: A comprehensive study of competition between XA and L21 atomic ordering. Results Phys 2019;12:435–46. https://doi.org/10.1016/j.rinp.2018.11.079.
[297] Curtarolo S, Setyawan W, Wang S, Xue J, Yang K, Taylor RH, et al. AFLOWLIB.ORG: A distributed materials properties repository from high-throughput ab initio calculations. Comput Mater Sci 2012;58:227–35. https://doi.org/10.1016/j.commatsci.2012.02.002.
[298] Saal JE, Kirklin S, Aykol M, Meredig B, Wolverton C. Materials Design and Discovery with High-Throughput Density Functional Theory: The Open Quantum Materials Database (OQMD). JOM 2013;65:1501–9. https://doi.org/10.1007/s11837-013-0755-4.
[299] Jain A, Ong SP, Hautier G, Chen W, Richards WD, Dacek S, et al. Commentary: The Materials Project: A materials genome approach to accelerating materials innovation. APL Mater 2013;1:11002. https://doi.org/10.1063/1.4812323.
[300] Landis DD, Hummelshøj JS, Nestorov S, Greeley J, Dułak M, Bligaard T, et al. The Computational Materials Repository. Comput Sci Eng 2012;14:51–7. https://doi.org/10.1109/MCSE.2012.16.
[301] Yang K. High-throughput design of functional materials using materials genome approach. Chinese Phys B 2018;27:128103. https://doi.org/10.1088/1674-1056/27/12/128103.
[302] Jain A, Hautier G, Moore CJ, Ping Ong S, Fischer CC, Mueller T, et al. A high-throughput infrastructure for density functional theory calculations. Comput Mater Sci 2011;50:2295–310. https://doi.org/10.1016/j.commatsci.2011.02.023.
[303] Jiang S, Nazir S, Yang K. High-Throughput Design of Interfacial Perpendicular Magnetic Anisotropy at Heusler/MgO Heterostructures. ACS Appl Mater Interfaces 2022;14:9734–43. https://doi.org/10.1021/acsami.1c20945.
[304] Jiang S, Yang K. Review of high-throughput computational design of Heusler alloys. J Alloys Compd 2021;867:158854. 10.1016/j.jallcom.2021.158854.
[305] Mouhat F, Coudert F-X. Necessary and sufficient elastic stability conditions in various crystal systems. Phys Rev B 2014;90:224104. https://doi.org/10.1103/PhysRevB.90.224104.
[306] Sanvito S, Oses C, Xue J, Tiwari A, Zic M, Archer T, et al. Accelerated discovery of new magnets in the Heusler alloy family. Sci Adv 2017;3:e1602241. https://doi.org/10.1126/sciadv.1602241.
[307] Faleev SV, Ferrante Y, Jeong J, Samant MG, Jones B, Parkin SSP. Origin of the Tetragonal Ground State of Heusler Compounds. Phys Rev Appl 2017;7:34022. https://doi.org/10.1103/PhysRevApplied.7.034022.
[308] Faleev SV, Ferrante Y, Jeong J, Samant MG, Jones B, Parkin SSP. Heusler compounds with perpendicular magnetic anisotropy and large tunneling magnetoresistance. Phys Rev Mater 2017;1:24402. https://doi.org/10.1103/PhysRevMaterials.1.024402.
[309] Ma J, He J, Mazumdar D, Munira K, Keshavarz S, Lovorn T, et al. Computational investigation of inverse Heusler compounds for spintronics applications. Phys Rev B 2018;98:94410. https://doi.org/10.1103/PhysRevB.98.094410.
[310] Ma J, Hegde VI, Munira K, Xie Y, Keshavarz S, Mildebrath DT, et al. Computational investigation of half-Heusler compounds for spintronics applications. Phys Rev B 2017;95:24411. https://doi.org/10.1103/PhysRevB.95.024411.
[311] He J, Amsler M, Xia Y, Naghavi SS, Hegde VI, Hao S, et al. Ultralow Thermal Conductivity in Full Heusler Semiconductors. Phys Rev Lett 2016;117:46602. https://doi.org/10.1103/PhysRevLett.117.046602.
[312] Vikram SB, Barman CK, Alam A. Accelerated Discovery of New 8-Electron Half-Heusler Compounds as Promising Energy and Topological Quantum Materials. J Phys Chem C 2019;123:7074–80. https://doi.org/10.1021/acs.jpcc.9b01737.
[313] Vikram SB, Barman CK, Alam A. Reply to "Comment on 'Accelerated Discovery of New 8-Electron Half-Heusler Compounds as Promising Energy and Topological Quantum Materials'". J Phys Chem C 2020;124:2245–6. https://doi.org/10.1021/acs.jpcc.9b12014.
[314] Xiao H, Dan Y, Suo B, Chen X. Comment on "Accelerated Discovery of New 8-Electron Half-Heusler Compounds as Promising Energy and Topological Quantum Materials". J Phys Chem C 2020;124:2247–9. https://doi.org/10.1021/acs.jpcc.9b10295.
[315] Shukla GK, Jena AK, Shahi N, Dubey KK, Rajput I, Baral S, et al. Atomic disorder and Berry phase driven anomalous Hall effect in a Co_2FeAl Heusler compound. Phys Rev B 2022;105:35124. https://doi.org/10.1103/PhysRevB.105.035124.
[316] Felser C, Fecher GH. Spintronics: From Materials to Devices. Netherlands: Springer; 2013.
[317] Yan H-L, Huang X-M, Esling C. Recent Progress in Crystallographic Characterization, Magnetoresponsive and Elastocaloric Effects of Ni-Mn-In-Based Heusler Alloys—A Review. Front Mater 2022;9.

[318] Krez J, Balke B. Thermoeletric Heusler Compounds BT - Heusler Alloys: Properties, Growth, Applications. In: Felser C, Hirohata A, editors., Cham: Springer International Publishing; 2016, p. 249–67. 10.1007/978-3-319-21449-8_10.

[319] Zhang X, Butler W. Theory of Giant Magnetoresistance and Tunneling Magnetoresistance BT - Handbook of Spintronics. In: Xu Y, Awschalom DD, Nitta J, editors., Dordrecht: Springer Netherlands; 2016, p. 3–69. 10.1007/978-94-007-6892-5_2.

[320] Hirohata A, Sukegawa H, Yanagihara H, Žutić I, Seki T, Mizukami S, et al. Roadmap for Emerging Materials for Spintronic Device Applications. IEEE Trans Magn 2015;51:1–11. https://doi.org/10.1109/TMAG.2015.2457393.

[321] Chappert C, Fert A, Van Dau FN. The emergence of spin electronics in data storage. Nat Mater 2007;6:813–23. https://doi.org/10.1038/nmat2024.

[322] de Paula VG, Reis MS. All-d-Metal Full Heusler Alloys: A Novel Class of Functional Materials. Chem Mater 2021;33:5483–95. https://doi.org/10.1021/acs.chemmater.1c01012.

[323] Ma YQ, Jiang CB, Feng G, Xu HB. Thermal stability of the $Ni_{54}Mn_{25}Ga_{21}$ Heusler alloy with high temperature transformation. Scr Mater 2003;48:365–9. 10.1016/S1359-6462(02)00450-5.

[324] Kainuma R, Imano Y, Ito W, Sutou Y, Morito H, Okamoto S, et al. Magnetic-field-induced shape recovery by reverse phase transformation. Nature 2006;439: 957–60. https://doi.org/10.1038/nature04493.

[325] Acet M, Mañosa L, Planes A. Chapter Four - Magnetic-Field-Induced Effects in Martensitic Heusler-Based Magnetic Shape Memory Alloys. In: Buschow KHJBT-H of MM, editor. vol. 19, Elsevier; 2011, p. 231–89. 10.1016/B978-0-444-53780-5.00004-1.

[326] Marcos J, Mañosa L, Planes A, Casanova F, Batlle X, Labarta A. Multiscale origin of the magnetocaloric effect in Ni-Mn-Ga shape-memory alloys. Phys Rev B 2003;68:94401. https://doi.org/10.1103/PhysRevB.68.094401.

[327] Muller C, Vasile C, Risser M, Heitzler J-C, Keith B. New air-conditioning and refrigeration magnetocaloric gas free system 2022.

[328] Oses C, Gossett E, Hicks D, Rose F, Mehl MJ, Perim E, et al. AFLOW-CHULL: Cloud-Oriented Platform for Autonomous Phase Stability Analysis. J Chem Inf Model 2018;58:2477–90. https://doi.org/10.1021/acs.jcim.8b00393.

[329] Mañosa L, Stern-Taulats E, Planes A, Lloveras P, Barrio M, Tamarit J-L, et al. Barocaloric effect in metamagnetic shape memory alloys. Phys Status Solidi 2014; 251:2114–9. https://doi.org/10.1002/pssb.201350371.

[330] He XJ, Xu K, Wei SX, Zhang YL, Li Z, Jing C. Barocaloric effect associated with magneto-structural transformation studied by an effectively indirect method for the $Ni_{58.3}Mn_{17.1}Ga_{24.6}$ Heusler alloy. J Mater Sci 2017;52:2915–23. https://doi.org/10.1007/s10853-016-0585-1.

[331] He X, Wei S, Kang Y, Zhang Y, Cao Y, Xu K, et al. Enhanced barocaloric effect produced by hydrostatic pressure-induced martensitic transformation for $Ni_{44.6}Co_{5.5}Mn_{35.5}In_{14.4}$ Heusler alloy. Scr Mater 2018;145:58–61. 10.1016/j.scriptamat.2017.10.015.

[332] He X, Kang Y, Wei S, Zhang Y, Cao Y, Xu K, et al. A large barocaloric effect and its reversible behavior with an enhanced relative volume change for $Ni_{42.3}Co_{7.9}Mn_{38.8}Sn_{11}$ Heusler alloy. J Alloys Compd 2018;741:821–5. 10.1016/j.jallcom.2018.01.244.